Patient-Specific Polyvinyl Alcohol Phantoms for Applications in Minimally Invasive Surgery

UCL

Department of Medical Physics and Biomedical Engineering

A dissertation submitted in partial fulfilment
of the requirements for the degree of
Doctor of Philosophy

Eleanor C Mackle

June 5, 2022

Supervised by:
Prof. Adrien Desjardins
Prof. Ioannis Papakonstantinou
Dr Malcolm Finlay

I, Eleanor C Mackle, confirm that the work presented in this thesis is my own. Where information has been derived from other sources, I confirm that this has been indicated in the thesis.

Abstract

In biomedical engineering, phantoms are physical models of known geometric and material composition that are used to replicate biological tissues. Phantoms are vital tools in the testing and development of novel minimally invasive devices, as they can simulate the conditions in which devices will be used. Clinically, phantoms are also highly useful as training tools for minimally invasive procedures, such as those performed in regional anaesthesia, and for patient-specific surgical planning.

Despite their widespread utility, there are many limitations with current phantoms and their fabrication methods. Commercial phantoms are often prohibitively expensive and may not be compatible with certain imaging modalities, such as ultrasound. Much of the phantom literature is complicated or hard to follow, making it difficult for researchers to produce their own models and it is highly challenging to create anatomically realistic phantoms that replicate real patient pathologies.

Therefore, the aim of this work is to address some of the challenges with current phantoms. Novel fabrication methods and frameworks are presented to enable the creation of phantoms that are suitable for use in both the development of novel devices and as clinical training tools, for applications in minimally invasive surgery. This includes regional anaesthesia, brain tumour resection, and percutaneous coronary interventions. In such procedures, imaging is of key importance, and the phantoms developed are demonstrated to be compatible across a range of modalities, including ultrasound, computed tomography, MRI, and photoacoustic imaging.

Impact statement

The methods developed in this thesis have the potential to lead to benefits, both within academia and also clinically. Within the academic environment, the work overcomes some of the challenges experienced with current phantom fabrication techniques and contributes to the literature with multiple publications. Methods are presented that can easily be replicated in a lab setting, to create patient-specific phantoms that are compatible with a range of medical imaging modalities. The specific phantoms described here are a proof of concept for the techniques, but could be expanded to include a variety of other geometries, structures, or pathologies.

In order to address the difficulties found in replicating existing phantoms in the literature, and to make it easy to share the work described here in a transparent way, the files used during the phantom fabrication process are made availbe via an open source platform (found <u>here</u>), which also provides a place for future work to be shared. This will enable others within the community to directly download both patient-specific (anonymised) data, and 3D printing files, so that they phantoms presented here can be replicated.

Clinically, the work here could be beneficial as it provides an alternative to commercially available training phantoms. Having cost-effective, patient-specific, realistic phantoms is of utmost important for minimally invasive surgical training. Their need has become even more apparent during the COVID crisis, where restrictions have made it increasingly difficult for junior clinicians to acquire necessary experience in patients, through observing or performing procedures in clinical practice. Training on the phantoms described here could reduce strain within the operating room, increase patient safety, and improve clinical outcomes.

Acknowledgments

Expressing my gratitude, in a concise way, to everyone who deserves it seems more of an impossible task than writing the thesis itself. Below are the people, without whom, none of the work here would have been possible.

Firstly, I would like to thank my supervisor, Prof. Adrien Desjardins, for what I think is now seven years of invaluable guidance. I am so grateful for the opportunity to pursue this PhD in your lab, and I could not have asked for a better supervisor. I have appreciated your positivity and enthusiasm, and your ongoing support has made me feel empowered to pursue exciting research directions. I loved that working with you always felt like a collaboration, and it has been a pleasure and a privilege.

Secondly I would like to thank my clinical and secondary superviors, Dr. Malcolm Finlay and Prof. Ioannis Papakonstantinou, for their guidance throughout this process. I also am eternally indebted to Dr Efthymios Maneas, for his help and insights. No question ever felt too silly to ask, and I can only imagine the levels of patience it must have taken to answer them all. This made all the difference to my confidence in my work; thank you.

One of my favourite things about undertaking a project in a multidisciplinary area was the opportunity to collaborate with a whole host of amazing people. I owe my thanks to everyone who has shared their expertise with me, and helped all my ideas come together. This includes Dr. Jonathan Shapey, with whom I collaborated for the brain phantom project, and was great fun to work with. Dr. Wenfeng Xia and Mengjie Shi helped me with the photoacoustic work, and were kind enough to let me use their imaging system. Prof. David Atkinson shared his MRI expertise with me, and provided so many valuable insights. Dr Simeon West also shared his clinical experience, and welcomed me into his clinic to observe relevant procedures. The whole Interventional Devices Group have been a joy to work with, on both a professional and personal level, and made me feel part of a team from my very first day.

I feel privileged to have been part of the i4Health Centre for Doctoral Training and the Wellcome / EPSRC Centre for Interventional and Surgical Sciences (WEISS). These centres have afforded me many incredible opportunities, and I would like to thank all the staff that work in both.

Table of Contents

List of Tables

List of Figures

Introduction

Table of Contents

1.1 Motivation

In biomedical engineering, phantoms are physical models of known geometric and material composition that are used to replicate biological tissues [2]. Such phantoms are vital tools in the testing and development of novel minimally invasive devices, as they can simulate the conditions in which devices will be used. This reduces the reliance on animals or cadavers, which have intrinsic limitations, including high cost and ethical concerns [3].

Clinically, phantoms can be used as training tools [4] and for patient-specific surgical planning [5]. Traditional clinical training uses the 'master-apprentice' model, where students learn from observing procedures and then trying them out on real patients, under observation. This model has many limitations, including the risk to patient safety, time constraints, and lack of uniformity in training. Phantoms can be used to effectively address this problem, by providing a simulation environment for trainees, meaning there is no need to use real patients in the early stages of training. They also allow for repetitions, and experience of a wide range of situa-

tions and pathologies. In addition, phantoms are useful for patient-specific surgical planning, as physical models of patient anatomy can be used to assess and test out different surgical techniques [6]. In clinical practice, the use of phantoms for simulation training has been shown to improve success rate in real surgeries, so can lead to reduced surgery times and better patient outcomes [7]. In some applications, phantoms have been shown to be more efficient than traditional clinical training models [8], and they help to shorten the learning curve for novices [9].

Despite their widespread utility, much of the phantom literature is complicated or difficult to follow, making it difficult for researchers to produce their own models. In addition, the majority of fabrication techniques used have associated limitations. For example, methods that are relatively simple and cheap to reproduce have limited anatomical accuracy. Other methods used include those which require expensive or hard to source materials, meaning it is impractical to create such phantoms in a research setting. Even phantoms that are commercially produced, which tend to be more anatomically accurate but are prohibitively expensive, are usually tailored to one specific imaging modality or application. This means that they are not suitable for applications where multiple imaging modalities are required, which is often the case in minimally invasive surgery.

Therefore, the aim of this work is to transform how medical imaging phantoms are created, by addressing three key challenges identified with current techniques:

1. **Anatomical realism**: phantoms that are not anatomically realistic have limited use, however, using current techniques it is challenging to create such models. Commercial models are available, which are often more anatomically realistic, but these models are prohibitively expensive, cannot be tailored to the intended application, and may not be compatible with desired imaging modalities.

2. **Compatibility across multiple imaging modalities**: in the development of novel minimally invasive devices, and also in surgical simulation for clinical

training, it is important that phantom models used are compatible across all the imaging modalities used in a real clinical setting. This can be challenging, as materials used for one imaging modality may not be suitable for another, and this can limit the utility of a phantom model.

3. **Sharing of information**: significant proportions of phantom fabrication techniques are not well documented in the literature. This makes it challenging to reproduce phantoms described, and is an inefficient way of developing new techniques.

In this work, techniques are developed to create phantom models that address these challenges. Firstly, the techniques enable patient-specific data to be used to create the models, so that they are anatomically realistic. They are also compatible across multiple imaging systems, so are suitable for simulating minimally invasive surgery. Through the use of 3D printing, files used to create these phantoms can easily be uploaded and shared, making it simple to download the files and recreate a phantom remotely. The methods also aim to be cost-effective and not highly complex, as these are limitations with current phantoms; however, both cost and complexity are subjective and what is feasible in this respect depends on the individual phantom and specific application. In general, the materials and equipment used are easily sourced and affordable in most laboratory settings.

1.2 Publications

The works that have been published as part of this thesis are summarised as follows:

1.2.1 First author publications

1. **Mackle, E.C.,** Maneas, E., Little, C., Carr, E., Xia, W., Nikitichev, D., Rakhit, R.D., Finlay, M.C. and Desjardins, A.E., 2019, February. Wall-less vascular poly (vinyl) alcohol gel ultrasound imaging phantoms using 3D

printed vessels. In *Design and quality for biomedical technologies XII* (Vol. 10870, p. 108700P). International Society for Optics and Photonics

2. **Mackle, E.C.,** Shapey, J., Maneas, E., Saeed, S.R., Bradford, R., Ourselin, S., Vercauteren, T. and Desjardins, A.E., 2020. Patient-specific polyvinyl alcohol phantom fabrication with ultrasound and x-ray contrast for brain tumor surgery planning. *JoVE (Journal of Visualized Experiments)*, (161), p.e61344

3. **Mackle, E.C.,** Maneas, E., Xia, W., West, S. and Desjardins, A.E., 2020. LED-based photoacoustic imaging for guiding peripheral minimally invasive procedures. *LED-Based Photoacoustic Imaging*, pp.321-334

4. **Mackle, E.C.,** Coote, J.M., Carr, E., Little, C.D., van Soest, G. and Desjardins, A.E., 2021. Fibre optic intravascular measurements of blood flow: A review. *Sensors and Actuators A: Physical*, p.113162

5. ***In preparation:*** Self-healing, ultrasound phantoms for peripheral nerve blocks (*International Journal of Computer Assisted Radiology and Surgery*)

6. ***In preparation:*** Patient-specific abdominal aortic aneurysm multi-modality imaging phantoms for EVAR simulation training (*International Journal of Computer Assisted Radiology and Surgery; Co-first author with Callum Little*)

1.2.2 Other publications

7. Carr, E., **Mackle, E.C.,** Finlay, M.C., Mosse, C.A., Coote, J.M., Papakonstantinou, I. and Desjardins, A.E., 2019, June. Optical interferometric temperature sensors for intravascular blood flow measurements. In *European Conference on Biomedical Optics* (p. 11075-1). Optical Society of America

8. Alles, E.J., **Mackle, E.C.,** Noimark, S., Zhang, E.Z., Beard, P.C. and Desjardins, A.E., 2021. Freehand and video-rate all-optical ultrasound imaging.

Ultrasonics, 116, p.106514

9. Shapey, J., Dowrick, T., Delaunay, R., **Mackle, E.C.,** Thompson, S., Janatka, M., Guichard, R., Georgoulas, A., Pérez-Suárez, D., Bradford, R. and Saeed, S.R., 2021. Integrated multi-modality image-guided navigation for neurosurgery: open-source software platform using state-of-the-art clinical hardware. *International Journal of Computer Assisted Radiology and Surgery*, pp.1-10

1.3 Contributions

The main contributions of this thesis and corresponding publications can be summarised as follows:

- **Chapter 3:** development of a novel technique for creating wall-less vascular ultrasound phantom

    – **Publications** 1, 4, 6, 7, 8

- **Chapter 4:** development of novel self-healing nerve phantoms, for applications in minimally invasive surgery, such as regional anaesthesia

    – **Publications** 5

    – **In collaboration with** Dr Simeon West

- **Chapter 5:** review of LED-based photoacoustic imaging for guiding minimally invasive procedures and extension of PVA phantom fabrication techniques to include photoacoustic imaging

    – **Publications** 3

    – **In collaboration with** Dr Wenfeng Xia and Mengjie Shi

- **Chapter 6:** development of a novel, multi-modality, patient-specific brain phantom for applications in minimally invasive surgery, such as vestibular schwannoma tumour resection

    – **Publications** 2, 9

    – **In collaboration with** Dr Jonathan Shapey

1.4 Thesis Organisatation

This thesis is divided into six chapters. In this chapter, a brief introduction to phantoms has been provided, in order to describe the context and motivations of this work. **Chapter 2** continues with a more detailed discussion of phantoms, and a literature review of work that is relevant to the overall themes of the thesis. In each subsequent chapter, an introduction section outlines the background, aims, and motivations of the chapter, and includes a concise literature review of work relevant to that section. There is also a discussion of limitations, applications, and future directions of the work at the end of each chapter.

Chapter 3 describes the development of a novel fabrication method for the creation of wall-less, vascular, ultrasound phantoms, using polyvinyl alcohol (PVA). This is initially adapted from work published as a conference paper, and then expanded to include the creation of patient-specific wall-less vascular phantoms. Vascular phantoms are important tools for the development of novel devices such as invasive blood flow sensors, and so as part of the research for this chapter, a review was written on fibre optic intravascular measurements of blood flow.

Chapter 4 expands on the methods previously developed, and in this chapter a novel, self-healing, ultrasound nerve phantom is described. This has applications as a clinical training phantom for minimally invasive procedures such as those used in regional anaesthesia. The work presented is adapted from that which has been submitted for publication.

Chapter 5 investigates the use of previously developed PVA phantoms for applications in photoacoustic imaging, and the feasibility of using the novel techniques to create phantoms for this imaging modality is confirmed. This chapter is part of work-in-progress, and the future directions of interest are discussed. As part of this chapter, research was undertaken on the use of LED-based photoacoustic imaging for guiding minimally invasive procedures, and subsequently, book chapter was published. The background material in **Chapter 5** is adapted from this published work.

Finally, in **Chapter 6**, a novel technique is developed for the fabrication of a multi-modality, patient-specific brain phantom, which includes a vestibular schwannoma tumour. This is adapted from work that has been published as a methods paper, and the phantom was further used in a publication describing the validation of a novel intraoperative navigation system.

Background

Table of Contents

The chapters of this thesis are all broadly focused on the same theme: to develop patient-specific phantoms for applications in minimally invasive surgery. The specific methods and applications vary between chapters and therefore, each subsequent chapter begins with a section detailing the relevant clinical and technical background information. That being said, all of the work in this project is linked and there is a significant amount of background material that is relevant to all the chapters. In this chapter, the aim is to present an overall introduction to the field, and the background work that is relevant across the whole thesis. This includes the concept of tissue mimicking phantoms and the materials commonly used for their fabrication, 3D printing techniques, and medical imaging modalities.

2.1   Phantoms

Phantoms are models of biological tissues, which simulate certain properties of the tissue and can be used to provide a clinically realistic imaging environment [2]. Phantoms are, therefore, vital tools in many aspects of biomedical engineering, especially within minimally invasive surgery, where they can be used for surgical planning, clinical training and development or validation of novel devices.

Minimally invasive surgery has become increasingly widespread over the past two to three decades and is now common among most, if not all, surgical disciplines. The technique allows a minimal number of incisions to be made in the patient, which shortens post-operative recovery times, reduces pain for the patients, and increases cost-effectiveness [10]. However, there are also limitations involved with the adoption of minimally invasive surgery; namely that the learning curve is steeper and more prologued for these surgeries, compared with traditional open surgeries [10, 11]. Phantoms can, therefore, be an indispensable tool in the translation of minimally invasive devices, as they can be used for clinical training.

There are certain properties that all phantoms need to have, in order to be suitable for applications in minimally invasive surgery. Firstly, they need to have complex, realistic structures so that they represent the relevant anatomy. Where possible, these phantoms should be created from real patient data - or in other words, be patient-specific phantoms - so that they are anatomically realistic and represent real structures and pathologies. Secondly, phantoms should have realistic imaging properties, so that they are compatible with the imaging modalities in the minimally invasive surgery in question. Finally, the phantoms, where possible, should be non-toxic and portable so that they can be taken into the hospital setting for clinical training and testing of novel devices.

There are many commercial training phantoms available on the market, but these are often prohibitively expensive (in the range of £1000-£10,000 each [12]) and have a limited life span (this varies depending on the materials and frequency

of use). These commercial phantoms are also tailored to a specific imaging modality and are rarely compatible with more than one. In minimally invasive surgery, it is common for multiple imaging modalities to be used and therefore the training phantoms should be compatible with all such modalities, so that training can be conducted in a realistic simulated environment. For both clinical training and novel device development, phantoms need to be used repeatedly, over long periods of time. This means that they either need to be durable enough to withstand this prolonged use, or should be cheap and easy to reproduce. As mentioned, commercial phantoms are very expensive and the methods used are patented so cannot be reproduced in a research laboratory.

As an alternative to commercial products, phantoms can be fabricated within the lab. This allows researchers to create phantoms that are tailored to the intended application, and in some instances this can also be more cost effective. The first stage involved in creating a phantom in a lab based setting is to choose an appropriate tissue mimicking material (TMM). The TMM is then often cast into anatomically realistic shapes by 3D printing appropriate moulds, as this technique is rapid and fairly low cost. The imaging modalities that the phantom will be used with, and their respective properties, must be considered when choosing the phantom TMM and fabrication process.

2.2 Tissue mimicking materials

TMMs are materials that - either naturally by chance, or by engineering their design - have properties comparable to those of human tissue. The specific property to be mimicked depends on the application, but includes mechanical, acoustic, and optical properties of tissue. There is an innumerable quantity of materials available for this purpose, and the choice of material for phantom fabrication is a key factor in determining the phantom's success and suitability. Certain materials are more suitable for one particular imaging modality and it is challenging to find

materials that encompass the desired range of properties. The most appropriate TMM also depends on the anatomical structure the phantom will replicate; for example, whether it is bone or soft tissue.

In this thesis, the focus was on soft tissue phantoms, so polyvinyl alcohol cryogel (PVA-c) was chosen as the TMM, due to its many favourable properties. Here, a summary of TMMs commonly used for soft tissue phantoms is presented, and the rationale for choosing PVA-c is described. It is not within the scope of this thesis to present every possible TMM, and many detailed reviews on the subject can be found within the literature [13, 14, 15].

2.2.1 Water based materials

Water based TMMs are very common, especially for ultrasound phantoms, because their high water content means they have acoustic properties similar to those of human tissue. Agar [1], agarose [16] and gelatin [2] are examples of water based TMMs that are frequently used. These materials have the advantage that they are relatively cheap and are easy to source and use. However, they are not mechanically robust, they degrade easily, and are susceptible to microbial invasion, which is undesirable, and can even be dangerous in a clinical setting. Water based phantoms can also suffer from dehydration and this affects their temporal stability [17].

2.2.2 Oil based materials

Oil based materials, on the other hand, do not dehydrate and are less susceptible to microbial invasion, so they have a higher temporal stability. Gel wax is on such oil-based material that has been demonstrated for use in phantom fabrication [18]. This material is sometimes friable, which can limit its use as a clinical training tool, and it also has a lower speed of sound (around 1445 m/s [18]) than human tissue (1540 m/s).

2.2.3   Other materials

Silicone is a common TMM material, due to its high stability and longevity [19]. It is also easy to add dyes to silicone to give phantoms a more realistic colour. However, silicone based phantoms have limited use for ultrasound imaging because the material has high acoustic attenuation and low speed of sound [15]. Therefore, silicone phantoms are more suited to computed tomography (CT) imaging [20].

Polyvinyl chloride-plastisol (PVCP) is sometimes used for phantom fabrication [21], but it can have a low speed of sound, high attenuation, and needs to be stored away from other plastics, due to its reactivity [17].

Organic materials such as animal tissue are used to mimic human tissue, as they do not require any preparation time and have acoustic and mechanical properties close to that of human tissue. These materials have very low longevity and the parameters of the material cannot be tuned to suit different requirements [15].

2.2.4   Polyvinyl alcohol cryogel

PVA-c is also a water based material, and is a synthetic polymer. It is prepared as a solution and then must undergo freeze-thaw cycles to solidify the material. During the freeze-thaw process, hydroxyl groups are physically cross-linked by hydrogen bonding, and an amorphous matrix of crystallites is formed [15, 22]. These freeze-thaw cycles mean that, although it is a simple fabrication process, it typically takes 24-48 hours to create a PVA-c phantom. Using PVA-c for phantom fabrication has many advantages. Firstly, PVA-c phantoms are more rigid and mechanically robust than those created using other water based materials, but are still relatively cheap to fabricate. With the addition of preservatives, the material can be kept for months at a time, although, as with other water-based materials, care must be taken with PVA-c phantoms to avoid dehydration; they can be kept indefinitely in as air-tight container. Finally, it is a non-toxic material, as demonstrated by its wide industrial use, including in craft glue and food packaging.

In the literature, PVA-c is well characterised and is already established as a high quality soft tissue mimic [23, 24]. As it is a water-based material that is mostly composed of water, the natural acoustic properties of PVA-c are close to those of human tissue. In addition, the mechanical strength can be tuned by varying the freeze-thaw cycles. This is because with increasing numbers of freeze-thaw cycles, the number, size, and stability of the crystallites increases [22].

2.3 3D printing

3D printing is often used in conjunction with TMMs for phantom fabrication, as recent advances mean that the technique is low cost, rapid and customisable. Different printers and printing methods are now commercially available, and so the method chosen depends on the specific application. With 3D printing, phantoms can be created in one of two ways: either directly or indirectly. The first involves the phantoms being 3D printed (directly) out of a plastic material. 3D printing is used indirectly when a cast mould is printed, and other materials are used to create the phantom; in the case the 3D printed structures do not form part of the final product. In both cases, the printing resolution achievable is a key factor in the choice of printing method. When phantoms are directly printed, the choice of material is also highly important.

The resolution that can be achieved with 3D printing depends on the method and printer used. Moreover, the resolution that any given printer is capable of achieving is not necessarily realised across all prints, especially when there is a high level of complexity. Although there are many modes of 3D printing, the most common modalities in the phantom literature include fused deposition modelling (FDM) and stereolithography (SLA) methods. Both FDM and SLA printing are examples of additive manufacturing because the prints are built up in a sequence of layer, although the way this is achieved is different between the two processes.

2.3.1 Fused deposition modelling printing

The most accessible 3D printing technique is FDM, as printers using this technique can be purchased for less than £1000, and in general the associated materials used with these printers are affordable and easy to source. The technique involves melting thermoplastics inside the print heads, and the molten thermoplastic is then extruded, layer by layer, onto the print build plate [25]. This layer building approach does restrict the geometries that can be produced using the technique, as large overhangs or gaps within the print cannot be realised without appropriate support materials.

The materials compatible with FDM printers are thermoplastics; materials used as standard include acrylonitrile butadiene styrene (ABS), poly(lactic acid) (PLA), and high impact polystyrene (HIPS). PVA is also commonly used as a support material in FDM printing, due to its water solubility, but can be used as a printing material in its own right, with certain limitations. These are all rigid plastics once printed, with fixed mechanical and acoustic properties, and so this limits the utility of phantoms created using these materials. It is also possible to create prints with more mechanically malleable materials, using flexible thermoplastics such as thermoplastic polyurethane (TPU), but these materials are more challenging to work with and still do not have acoustic properties comparable to those of human tissue.

The resolution achievable using FDM printing is primarily dictated by the size of the print heads used to deposit the material. The diameter of the nozzles used to extrude varies between 0.2 – 0.4 mm, which in theory would be the minimum resolution achievable. However, in practice, it is very challenging to achieve this and the actual resolution depends on variables including the print settings and material quality [25].

2.3.2   Stereolithography printing

Prints made with SLA use an ultraviolet laser to gradually build up the layers from a vat of liquid resin. The material used is photoactive, and so the laser cures the material, turning it from liquid to solid [26]. This was the first commercially available form of 3D printing, but in general the technique is more expensive than FDM, so used less frequently in a research setting [25]. In some instances, the time taken to produce a print is lengthier with SLA printers, because extra steps may be required, to wash off the uncured resin, and to further cure the material for increased mechanical strength. However, as prints are built up from a vat of liquid resin, there are less restrictions on the feasible geometries and there is also a lower rate of print failures [26].

SLA printers cost thousands of pounds, and the resin used in conjunction with the printer is more expensive than the materials required for an FDM print. As a comparison between FDM and SLA printing, Coles-Black *et al.* described the fabrication of an abdominal aortic aneurysm model, and the materials to create the same phantom were found to cost $10-20 using an FDM printer, and $50-100 using an SLA printer [26].

The advantage of SLA is that the use of a laser to create prints means that the results are very precise and higher resolution can be achieved than with FDM, so SLA printers are preferred when fine details are required on a print. The typical nominal resolution of SLA printers is 30 - 140 µm, and is dependent on the minimum spot size of the laser [27].

2.3.3   3D printed phantoms

There are many examples in the literature where 3D printing has been used successfully to create phantom models. When phantoms are produced by direct 3D printing, they have the advantage that the technique is rapid, easily repeatable and the material will not degrade. These phantoms are useful for CT, x-ray imaging

and positron emission tomography (PET) imaging, both to investigate image quality and for patient-specific dosimetric verification [20, 28, 29]. They may also be suitable as clinical training models, especially if replication of soft tissues is not required [30].

Due to the nature of the plastic based 3D printing materials, phantoms made through direct 3D printing are generally rigid, which is not realistic for soft tissues. However, advancements in 3D printing materials have meant that it is possible to create more rubbery, flexible models [31]. When phantoms are 3D printed directly, it is difficult to alter any of the properties of the material, and only one property, such as speed of sound or mechanical strength, can be prioritised and simulated [32]. This means that the choice of printing material dictates the compatibility with imaging modalities, and in general phantoms that are directly printed are not compatible with ultrasound imaging.

When direct 3D printing is not suitable for the intended application – for example, when the phantom must include soft tissues – an alternative method must be employed. In this case, 3D printing can be used to create a negative mould of the structure of interest, and a suitable TMM can then be poured into the mould. Although this does increase the complexity and time required for the fabrication process, it means that the phantoms have a wider utility, and their properties can be selected more effectively. This technique has been used to create phantoms of many structures, including the breast [33], brain [34], pulmonary artery [35] and liver [19]. There are still limitations associated with these phantoms, including that they are often tailored to one specific modality and are therefore not compatible with the multi-modality imaging environment used in many minimally invasive surgeries.

2.4   Imaging

It is also important to understand the imaging modalities that are commonly used in minimally invasive surgery, in order to understand the requirements of phantoms for

their intended application. For the applications in this thesis, the primary imaging modality used was ultrasound, so all phantoms needed to be firstly compatible with ultrasound. In addition, other modalities used for multimodality imaging, were CT, MRI and photoacoustic imaging (PAI). Here, the relevant properties for each modality are described and explained, to give context for the phantom fabrication process.

2.4.1 Ultrasound

In ultrasound imaging, high frequency acoustic pulses are transmitted into tissue using a transducer. The transmitted pulses propagate through the tissue and when they encounter an acoustic impendence mismatch, the sound is scattered, with some of this scattered energy being received back at the transducer. The amplitude and timing of the received signal is then used to create an image of the tissue. This means that when creating a phantom, the properties of a material that will determine how appropriate it is for ultrasound imaging are the speed of sound, acoustic attenuation coefficient, and acoustic backscatter coefficient. Ultrasound imaging is most commonly used for imaging soft tissues and therefore, it is the properties of soft tissue that should be considered in ultrasound phantoms.

In order to be as realistic as possible, phantoms should be created with acoustic properties similar to those of human tissue. The speed of sound [36] in soft tissue is 1540 m/s. The acoustic attenuation and backscatter coefficients in tissue are dependent on frequency, although there is a range of typical values for these coefficients in the literature [2, 37, 38]; the attenuation coefficient is in the range of 0.5-3.3 dB cm^{-1} MHz^{-1}, and the acoustic backscatter coefficient is in the range of 10-5 - 10-1 cm^{-1} [2].

The natural properties of PVA-c make it a suitable soft tissue mimic and this is especially true for ultrasound imaging. As PVA-c is mostly comprised of water, the speed of sound and acoustic impedance in the material are similar to those of human

tissue (1520 - 1560 m/s [15]) and it also has a low acoustic attenuation (0.07 - 0.28 dB/cm MHz [15]). As investigated in this thesis, with the right additives, PVA-c can be 'self-healing' with ultrasound imaging, so that it can be used repeatedly without damage to the phantom being visible on ultrasound images. There are many examples in the literature where PVA-c is used as an ultrasound compatible TMM [39], and it has also been used as an ultrasound elastography phantom material [40, 41, 42].

When imaging human tissue, a water-based gel is applied to the area of interest, to couple the transducer to the tissue and reduce the effects of impedance mismatch from air. A small force is also applied to the transducer to ensure coupling with the skin surface. This means that, if it is to be used to simulate minimally invasive surgery, the phantom should also have the potential to be used in this way; it needs to have a surface that coupling gel can be applied to, and be able to withstand light pressure from the transducer. Many softer materials such as agar are not especially suited to this, whereas PVA-c is appropriate, because the mechanical strength can be altered by varying the freeze-thaw cycles, or by adding additional acoustic scatterers into the mixture during fabrication.

2.4.2 Photoacoustic imaging

Photoacoustic imaging (PAI) is an emerging modality that provides information complementary to conventional B-mode ultrasound imaging. With PAI, pulsed excitation light is delivered to tissue, where it is absorbed by specific tissue constituents and the corresponding temperature rise generates ultrasound waves via the photoacoustic effect. Received ultrasound signals are processed to generate an image [43]. Whereas B-mode ultrasound imaging yields information about variations in the mechanical properties of tissue, image contrast in PAI stems from optical absorption by endogenous or exogenous chromophores. In the visible and near-infrared (NIR) wavelength ranges, haemoglobin in blood is a prominent optical

absorber, which means that vasculature can be visualised with high contrast [43] and blood oxygen saturation can be estimated [44]. Lipids can also be prominent optical absorbers in the NIR, so nerves can also be directly visualised [45, 46, 47]. Studies performed to date indicate that PAI has strong potential for clinical translation in a broad range of applications, including in guiding minimally invasive surgeries and interventions [48].

PVA-c is suitable for PAI because its optical properties can be controlled by varying the freeze-thaw cycles, or by adding additional contrast agents into the material. Kharine *et al.* were able to control the optical characteristics of PVA-c to mimic those of human breast tissue, by optimising the freeze-thaw cycles [49]. Other studies have used gel wax and PVCP as PAI phantoms; both of these are optically transparent, unlike human tissue, and so optical scatterers are added for optical contrast [50, 18].

2.4.3   Computed tomography

CT imaging uses x-rays to measure the attenuation of different tissues, and this is used to create tomographic images of the organs of interest [51]. Different materials used within a phantom will naturally have different densities and so different attenuation coefficients. The CT contrast within one material can also be changed by adding a contrast agent. The majority of CT phantoms in the literature are used for image quality assessment, rather than for clinical training, and are often 3D printed in hard plastics, so may not adequately simulate soft tissues, or be compatible with ultrasound imaging [52, 53]. It has also been challenging to fabricate CT phantoms that are compatible with multimodality imaging [51].

2.4.4   Magnetic resonance imaging

The principles of MRI imaging are beyond the scope of this project and will not be covered here. Briefly, for MRI imaging it is the T1 (spin lattice, or longitudinal)

and T2 (spin spin, or transverse) relaxation times that are relevant and should be similar to human tissue, in order for the phantom to be useful. In general, this can be complicated to replicate in a phantom, but as PVA-c is predominantly made of water, it naturally has MRI properties similar to that of human tissues. PVA-c was shown as early as the 1980s to be a suitable MRI phantom material [54]. Unlike the optical and acoustic properties of PVA-c, the MRI parameters do not undergo significant changes with increasing freeze-thaw cycles, and once the solution is solidified from a gel to a solid, the MRI parameters in the material remain approximately constant [54]. This means that the freeze-thaw cycles can be adjusted to address other imaging requirements, without drastically affecting the MRI properties. As with CT phantoms, the MRI parameters can be tuned for PVA-c by adding contrast agents added into the aqueous solution. PVA-c has previously been used as a TMM for MRI imaging, and so is an appropriate material to choose for multimodality imaging [55, 56]. One final, important consideration for MRI phantoms, is that they must be free of any metal, as the inclusion of any ferromagnetic materials could cause distortions to the image, and pose a safety risk.

2.5 Conclusion

In the literature there are many 'home-made' phantoms used as alternatives to commercial phantoms. These phantoms aim to overcome some of the limitations described, such as limited patient-specific geometries, restricted compatibility with imaging modalities, and high cost. However, the published methods often use expensive, hard to source, or toxic materials, and the fabrication processes can be complex and difficult to follow. Methods that are less complex, on the other hand, may not have the required level of anatomical detail and cannot accommodate for variations between individual patients.

Therefore, there is a high unmet need for a novel phantom that addresses these

limitations. The following work aims to address this, and create of patient-specific phantoms that have realistic imaging properties, and are suitable for the multi-modality imaging techniques used in minimally invasive surgery.

Multi-Modality, Patient-Specific, Polyvinyl alcohol Wall-Less Vascular Phantoms

Table of Contents

This chapter describes a novel fabrication technique for creating patient-specific vascular phantoms, which are compatible with multi-modality imaging. The preliminary work for this was presented by the author of this thesis at SPIE Photonics West, and published as a conference paper [57]. The subsequent developments were combined with work in 4 Chapter 4 and have been submitted to the International Journal of Computer Assisted Radiology and Surgery (IJCARS).

3.1   Introduction

There are many applications of minimally invasive surgery where vasculature is important - either as the target of an intervention, or because it must be avoided during a procedure. Therefore, there are a number of applications where phantoms of the human vasculature would be useful tools. However, current methods available to create such phantoms have limitations. In this chapter, a novel technique for the fabrication of patient-specific phantoms is presented. These phantoms were developed for applications in minimally invasive coronary surgery, and so are phantoms of the coronary vasculature. The background and literature described here is, therefore, focused on this specific application, but the techniques presented for phantom fabrication could be applied to other types of vasculature, in various clinical scenarios.

3.1.1   Clinical background: coronary artery disease

Cardiovascular diseases, including coronary artery disease, are the leading cause of death worldwide [58]. In 2016, coronary artery disease in particular had a global prevalence of 154 million, which represented 2.2 % of the overall global burden of disease [59]. In addition to the high burden of the disease, there is also a high economic cost, which comes from hospitalisations, medication, and loss of productivity; in France, the estimated average 2-year cost per patient with coronary artery disease is €1746 [60]. It is therefore of vital importance to treat and effectively manage patients who have coronary artery disease.

The underlying pathology that causes coronary artery disease is atherosclerosis. This is where lipid accumulates and plaque forms in the walls of the coronary vessels, often accompanied by low-grade inflammation [59]. The plaques can block the vessels and restrict blood flow around the heart, leading to cardiovascular events such as myocardial infarction, (more commonly known as a heart attack). Treatments for the disease aim to provide relief of symptoms, but also to prevent future cardiovascular events.

In order to give an accurate diagnosis and provide the patient with appropriate treatment, it is often necessary to assess the extent and location of atherosclerosis in the coronary vessels. Blood flow is directly linked to pathology in the coronary arteries, so the most effective way to assess the extent of the disease is to look at the flow through the vessels. To date, there is no suitable method to directly quantify the flow through the coronary vessels. In clinical practice, coronary angiography and intravascular ultrasound (IVUS) can be used to qualitatively assess the extent of coronary artery disease, and guide stent implantation, which help to restore blood flow by opening up the diseased vessels.

3.1.2 Technical background: vascular phantoms

For improvements in the diagnosis and treatment of coronary heart disease, phantoms are vital tools to enable efficient development of new medical devices. However, it is challenging to create anatomically realistic phantoms that simulate the coronary vascular, due to its complex and branching structure. One of the main limitations of vascular phantoms that have been developed to date is their lack of compatibility with ultrasound or optical imaging. As IVUS is regularly used in coronary interventions, phantoms need to have ultrasound compatibility in order to be used to simulate these minimally invasive surgeries.

The basic requirements for a vascular phantom are in line with the general requirements of a phantom, which were presented in **Section 2.1**. In this instance,

the use of patient-specific data should allow the complex, branching structure of the coronary vasculature to be replicated. As coronary angiography and IVUS are used clinically, for minimally invasive surgeries to treat coronary artery disease, vascular phantoms for these applications must be compatible with both ultrasound and X-ray imaging. It is also important that vascular phantoms have hollow vessel structures, which can be connected up to a flow setup, to allow fluid to be passed through the vessels and simulate blood flow around the coronary vasculature.

In the literature, two main techniques have been developed for creating vascular phantoms. They are either what is referred to as a 'walled' phantom, or they are created to be 'wall-less' phantoms. Regardless of the technique used, there are basic structural features that vascular phantoms need to have, and development of novel phantoms should be based around this basic features. A basic phantom and its required structures are outlined in **Fig. 3.1**. This includes the following:

1. A hollow vessel structure, the most basic being a straight vessel, as shown in the diagram

2. The vessel should be surrounded by an appropriate tissue mimicking material (TMM), which simulates the tissue surrounding the coronary vessels and gives a more realistic imaging environment

3. A box to encapsulate the phantom, which also makes it easier to attach the phantom to a flow setup

4. Blood mimicking fluid should be used to simulate blood flow through the vessels

3.1.3 Walled phantoms

In walled phantoms the vessel structure is created using a solid material, such as plastic tubing. This solid vessel structure is then embedded into a TMM. Various
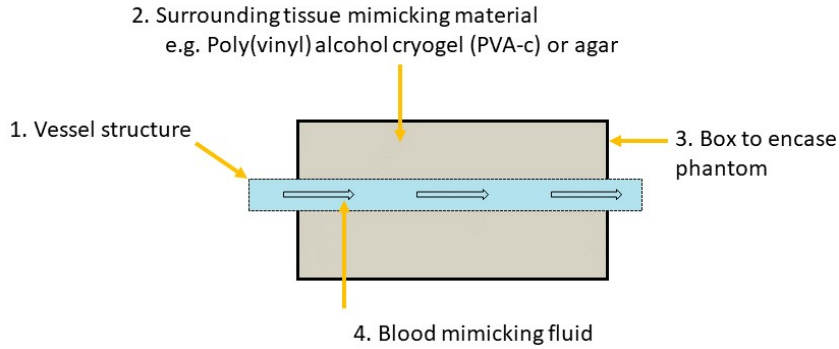
Figure 3.1: Diagram to show the necessary features for a vascular phantom

tubing materials have been used to create walled vascular phantoms, and these materials were reviewed by Law *et al.* [61]. 3D printing has been implemented to create walled vascular structures, including phantoms of an abdominal aortic aneurysm and neurovasculature [62, 26]. However, 3D printed structures made of hard plastics are not compatible with ultrasound imaging. Negative moulding of TMMs, such as PVA-c, has be used to create walled vessels that are more realistic than those created using plastic tubing [23, 63, 64, 65, 66, 67, 68, 69].

3.1.4 Wall-less phantoms

In wall-less phantoms, the material used to create the vessel structures is removed after the surrounding TMM has set, leaving a hollow space within the TMM, through which fluid can be passed. A wall-less technique is often preferred, especially when the phantom is to be imaged with ultrasound, as the lack of material at the vessel wall reduces impedance mismatch between the surrounding tissue and the vessel [70].

The simplest method used to create a wall-less phantom involves placing solid rods - with a diameter the size of the required vessel diameter - into a box, and the pouring the TMM over the rods. Once the TMM has solidified, the rods can be pulled out; a visual explanation of this can be seen in **Fig. 3.2**. This method was used as early as 1995 for the creation of phantoms with straight vessels [71, 72, 1].

It is also possible to create simple bifurcations and stenoses using this method, however, with this technique it is challenging to create more complex structures [73, 74, 75].
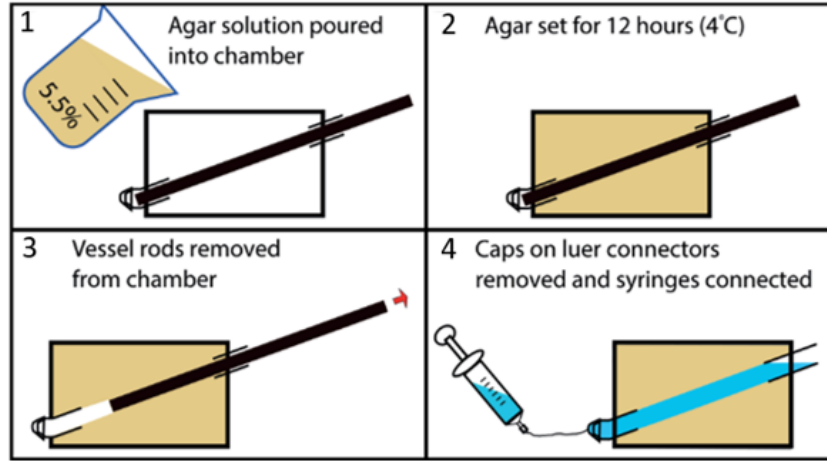
Figure 3.2: A simple method for creating wall-less phantom, by removing plastic rods from set tissue mimicking material; adapted from [1]

Another method for creating wall-less phantoms uses a lost casting technique to make solid vessels in a metal alloy that has a low melting point. This metal structure can be surrounded with a TMM and once that has set, the metal can be melted away, leaving a wall-less structure. There has been success in creating bifurcating and stenosed vessels using low melting point metals, and the technique has even been used to create anatomical replications of a human carotid bifurcating artery and a renal artery [76, 77, 78, 63]. However, using metals increases the cost and complexity of the fabrication process.

Finally, in a recent study by Ho *et al.*, 3D printing was used to create vessel structures made of polylactic acid (PLA) [79]. The structures were embedded in the phantom and removed after the TMM had set, by submerging the phantom in chloroform to dissolve the PLA. This technique produced wall-less phantoms with tortuous anatomical structures, but the use of chloroform should be avoided, as it is a dangerous chemical and known carcinogen.

3.2 Methods

As part of this thesis, a novel technique for fabricating wall-less vascular phantoms was developed. The process uses 3D printing in a water soluble material, which enables patient-specific phantoms, to be created. The technique and development process is described in detail here. The early stages of this work were published as a conference paper at SPIE Photonics West 2019, entitled 'Wall-less vascular polyvinyl alcohol gel ultrasound imaging phantoms using 3D printed vessels' [57]. The technique was then further developed to include patient-specific data, and add compatibility across a range of imaging modalities, which meant that these phantoms are highly relevant for surgical planning and clinical training in minimally invasive surgical procedures.

3.2.1 Overview

In the novel fabrication method, vessel structures were 3D printed in in water soluble PVA, and embedded into the TMM. As mentioned previously, PVA-c was chosen as the TMM, but these are two different forms of the same material. Printed PVA is a solid plastic that dissolves when submerged in water, whereas PVA-c is an aqueous solution of the material, that can be solidified through freeze-thaw cycles. Once the 3D printed structures had been embedded into the TMM, they were subsequently dissolved, leaving hollow, wall-less vessel structures. The various stages of the fabrication process are summarised in **Fig. 3.3**:
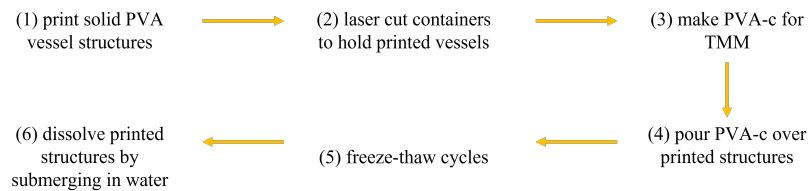
Figure 3.3: The six key stages of the process developed here, to create wall-less vascular phantoms

3.2.2 Printing resolution tests

The minimum dimensions achievable for 3D printed vessel structures were investigated by printing small vessel segments of various lengths. CAD models of straight vessels, 30 mm in length, were created in Autodesk Fusion 360 and then printed in incrementally smaller sizes, until the prints failed. Both hollow and solid prints were tested, using the Ultimaker 3. It was thought that hollow vessels would be preferred over solid printed structures for phantom fabrication, as it could enable the printed structures to be dissolved more easily. Hollow vessels would also be more difficult to print effectively, and so both hollow and solid structures were tested to see what was achievable.

In the first stage of this work, the vessel structures were created manually, rather than being extracted from patient-specific data, and this was simpler and provided a proof of concept. Computer aided design (CAD) software was used to design these structures, (Autodesk Fusion 360, Autodesk Inc., San Rafael, California, United States) and they were saved as .stl files, which are compatible with 3D printing software. In this project, the software used for this was Cura, (Ultimaker, Utrecht, Netherlands). Once the STL files were imported into the software, suitable print settings were selected, including 20% infill and the 'fast' option, to reduce the time required for printing. These structures were then printed on a commercially available printer, the Ultimaker 3, (Ultimaker, Utrecht, Netherlands), using PVA at the printing material (RS Components, Corby, United Kingdom).

3.2.3 Vessel fabrication

Three different designs were printed: a straight vessel, a stenosed (narrowed) vessel, and a bifurcated (branched) vessel. The 3D printed structures can be seen in **Fig. 3.4**. Vessels were all printed standing upright on the baseplate, with no support material used. The straight vessel was 120 mm in length, with a 10 mm outer diameter. The stenosed vessel was also 120 mm in length, with a 10 mm outer

diameter and a 50% stenosis in the middle section that was 30 mm long and 5 mm in diameter at the narrowest point. The straight section of the bifurcated vessel was 70 mm long with a 10 mm outer diameter; each branch was 60 mm long. The two branches of the bifurcation had a 10 mm and 8 mm outer diameter, respectively, and the angle between them was 90°.
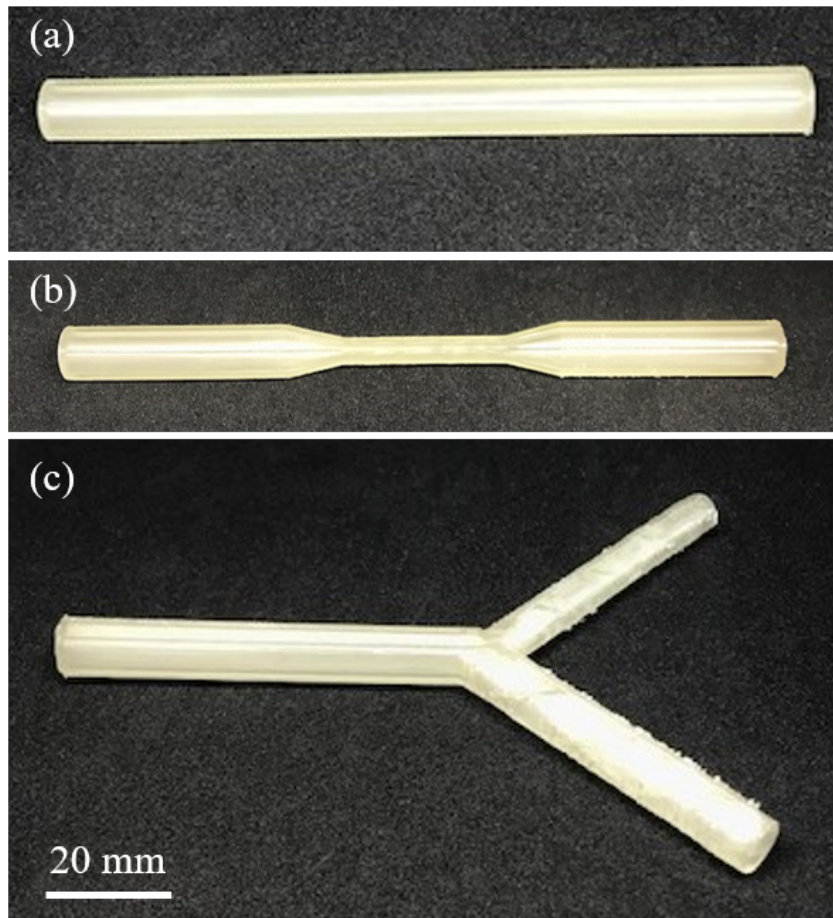
Figure 3.4: 3D printed vessel structures used to create first iteration of phantoms (a) straight vessel (b) vessel with 50% stenosis (c) bifurcation

3.2.4 Patient-specific vessel fabrication

Once the technique had been developed using manually designed vessels, it was expanded to include patient-specific phantoms, which was achieved by 3D printing patient-specific vessels, segmented from patient scans. Two examples shown here

include a carotid artery and a branched coronary vessel. These two structures are relevant in minimally invasive interventions, and are often imaged using either external or internal ultrasound, as well as CT or MRI imaging.

For the carotid artery, a patient-specific model was obtained from an online repository (http://grabcad.com; GrabCAD, Cambridge, Massachusetts, United States). The STL was then imported into the 3D printing software, as before, and printed in PVA. The CAD model of the vessel and the printed structure can be seen in **Fig. 3.5**. The carotid artery was chosen, as it is an important vessel in coronary interventions and is also located superficially in the neck, so is imaged clinically using external ultrasound, unlike a significant amount of the coronary vasculature, which is located too deep under the surface for external ultrasound imaging.
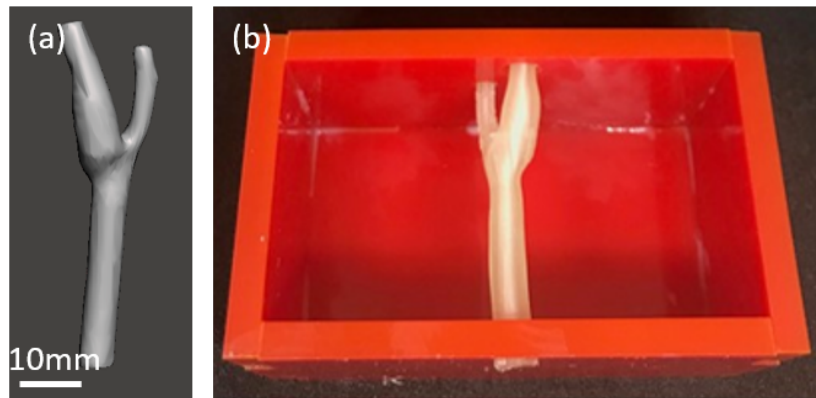
Figure 3.5: Carotid vessel used to create patient-specific phantom (a) CAD model of vessel downloaded from GrabCAD (b) the same vessel 3D printed in PVA-c

The coronary vessel phantom was created from an anonymised patient CT scan. The scans were obtained, and vessels segmented prior to this project. Clinically, intravascular imaging does not occur over the whole coronary tree - instead, it is performed over specific areas of interest and therefore, a small section of the coronary tree was chosen. This enabled the method to be tested, and for realistic clinical imaging to be conducted. The segmented coronary tree, and chosen section for printing can be seen in **Fig. 3.6**. The segmentation was loaded, into Meshmixer (Autodesk Inc., San Rafael, California, United States;

http://www.meshmixer.com/), which enabled the model to be manipulated, and a section to be extracted and 3D printed. The vessel section chosen was small (approximately 2.5 mm diameter) and branched, as small branching structures have been especially challenging to fabricate using current phantom fabrication methods.
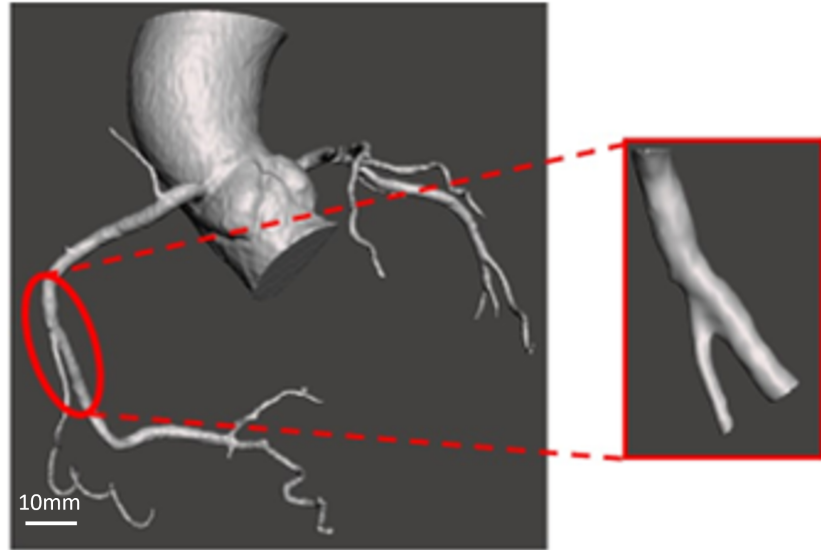
Figure 3.6: Segmented coronary tree that was used to create second patient-specific phantom. Zoom section included portion used in the phantom

3.2.5 Printing with PVA

The manually designed and patient-specific structures were 3D printed in PVA. This PVA filament used for 3D printing can absorb water from the surrounding environment, which affects the quality of printed models; therefore, care was taken to ensure the PVA used was dry prior to use. When not in use, spools of PVA were kept in a sealed contained along with a desiccant. It was also found that the PVA printed well at 200°C, but above this temperature there was a tendency for the PVA to burn, so that the print quality was reduced and the printed vessels had exteriors that were less smooth. During printing, the baseplate was heated to 60°C, to provide good adhesion to the plate.

Preliminary studies showed that in some instances, the aqueous solution used

to create PVA-c partially dissolved the printed structures before it has solidified. Therefore, printed structures were coated in parylene (approx. 3 µm) to waterproof them and stop them from dissolving before intended. It was also found that hollow 3D printed PVA vessel structures dissolved much more quickly than solid ones, however, at small scales it was challenging to print hollow structures.

3.2.6   Phantom preparation

The printed structures were combined with a TMM to create the final phantom. Containers were made to shape and encapsulate the phantoms by laser cutting and combining sheets of acrylic. Holes in each end face of the container allowed printed vessel structures to be slotted in. These containers allowed the phantoms to be free standing and portable. For the straight and stenosed phantom, the box dimensions were 50 mm × 50 mm × 100 mm; for the bifurcation phantom, the box dimensions were 100 mm × 50 mm × 112 mm.

The TMM used was PVA-c, for reasons discussed in **2**, and this was fabricated using a method adapted from Kharine *et al.* [49]. A 10% w/w aqueous solution was created by mixing the solid PVA powder with water, in a temperature controlled water bath (HBR4 control, IKA), using an electronic stirrer (Eurostar Digital 20, IKA). Each batch of PVA-c was 1500 ml, as this amount of solution was found to be optimal for the apparatus; if smaller batches were made, there was not enough solution in the conical flask for adequate and homogeneous stirring.

To make up these 1500 ml batches, a 2 L conical flask was used, with 1350 ml of deionized water added. The deionised water was parboiled before being added to the conical flask, so that it was hot, but was not allowed to boil completely, to avoid significant amounts of the water being lost to evaporation. The flask of water was suspended in the water bath, set at 90°C, and the electronic stirrer was added and set to 1800 rpm. PVA powder (Sigma Aldrich 99%+ hydrolysed, average molecular weight 85,000-140,000) was added gradually over 30 min. The solution was then

left to stir for 90 min to allow for the PVA powder to completely dissolve.

Subsequently, the conical flask was removed from the water bath and the solution was left to cool at room temperature for approximately 10 min. Once cool enough to handle, 0.5% w/w glass microspheres (53 - 106 μm) were stirred into the PVA-c solution for additional ultrasound contrast. In the later work using patient-specific vessels, sonication was used at this stage, to ensure homogeneous mixing of the glass spheres with the PVA-c; each batch was sonicated for 5 mins. In early work, problems were encountered with the longevity and storage of the phantoms, as they had to be stored in the fridge and did not last more than around a month, before becoming mouldy. Different preservatives were researched, and so for the patient-specific phantoms, potassium sorbate was also sonicated into the aqueous mixture of PVA-c as preservative. This material has been used previously in phantoms as an antimicrobial agent, and is safe to use, as it is a food preservative. Literature values often use 0.3% potassium sorbate, but in these phantoms 0.5% w/w was found to be a suitable amount to preserve the phantom for months, without affecting any of the other properties of the phantom. The phantoms could then be kept at room temperature, in a sealed bag to prevent them drying, and could be stored for months at a time.

When the PVA-c mixture was ready, with all the relevant contrast agents and preservatives added, it was poured into the phantom containers, over the 3D printed vessel structures that were positioned inside. In the preliminary studies with manually created vessel structures, the phantoms were left to cool for an hour at room temperature before the freeze-thaw cycles were started. A single freeze-thaw cycle involved freezing at -20°C for 24 h and thawing in the fridge at 5°C for 24 h. Each phantom underwent one freeze-thaw cycle. After the thawing was complete, the phantoms were submerged in deionized water for 48 h to dissolve out the printed structures.

In the subsequent work, where patient-specific vessels were used, the phantoms

underwent two freeze-thaw cycles, rather than the one used in earlier. This was because it was subsequently found that after two cycles phantoms were more mechanically robust. It was then easier to manipulate them for ultrasound imaging in the same way that human tissue would be, and so they were more realistic.

3.2.7 Concentration tests

Initially, the vascular phantoms described here were only compatible with ultrasound imaging. Later in the work, the benefits of adding compatibility with include computed tomography (CT) and MRI were realised, as it would increase the utility of the phantoms if they were compatible across a clinically relevant range of imaging modalities. Limited literature is available on the use of CT and MRI contrast agents in PVA-c and so, in order to validate the concentrations that should be used for appropriate tissue mimicking contrast, various concentrations of CT and MRI contrast agents were investigated in conjunction with PVA-c.

Barium sulphate ($BaSO_4$) was chosen as the CT contrast agent; this is used clinically, so is safe to use and relatively easy to source. $BaSO_4$ is insoluble in water and therefore, once the freeze-thaw cycles are performed, it is unlikely that the contrast agent would bleed out into other structures. For the MRI contrast agent, copper sulphate ($CuSO_4$) was chosen. Unfortunately, this is a toxic material, and is soluble in water, but it was not possible to obtain a suitable alternative. Gadolinium is used clinically for MRI imaging, and is also toxic in its native state. As a contrast agent, it is used with a chelating agent, which is thought to overcome its toxicity, so it is safe to administer. However, there is also research to suggest that it is not as safe as originally thought [80], and in the context of this research, copper sulphate was easier to obtain and work with.

A test phantom was constructed to verify that varying the concentration of one contrast agent would not affect the performance of the other, and experiment with the appropriate levels to use for a tissue mimicking phantom. The test included 12

separate samples in a 3×4 configuration, where each sample contained 10% w/w PVA-c with 0.5% w/w glass microspheres for constant ultrasound contrast and 0.5% w/w potassium sorbate as a preservative. All samples underwent two freeze-thaw cycles. The concentration of $CuSO_4$ and $BaSO_4$ in each sample was varied so that each row of the test phantom contained varying concentrations of $CuSO_4$, and each column contained varying concentrations of $BaSO_4$. The concentration range of interest was between 0 - 10% for $BaSO_4$ and 0 - 1% for $CuSO_4$, based on the literature [56].

3.2.8 Imaging

Ultrasound images of the phantoms were acquired using a clinical scanner (MDP Ultrasonix, Richmond, Canada) and a linear array probe (14-5 MHz). Phantoms were submerged in water for imaging, to allow for coupling between the probe and the TMM and to remove air from the wall-less vessels.

IVUS imaging was also performed on the patient-specific phantoms. This was performed at the Royal Free Hospital, using a 40 MHz OptiCross Coronary Imaging Catheter (Boston Scientific, United States), with the phantoms submerged in water.

CT images were acquired using an O-arm 3D mobile X-ray imaging system (Medtronic Inc, Minneapolis, USA). T1 MRI images were acquired with a 3T system (MAGNETOM Prisma scanner, Siemens, Munich, Germany). The protocol used for the MRI acquisition with this scanner can be found in **Appendix A**.

3.2.9 Image Analysis

The image analysis was performed in MATLAB. Data from the CT and MRI imaging were imported, stored, and displayed as an image. Regions of interest (ROIs) were created by drawing ellipses and displaying these as an overlay on the image; in this way, it was ensured that the ROI included a significant proportion of the sample and not the background. Data were then extracted from the ROI and used

to calculate the mean value, which could be recorded, or plotted against the concentration of the sample. At this stage, the mean image intensity was extracted for each sample, to demonstrate how the resulting image intensity of the phantoms created here could be varied by varying the concentration of additives. In future chapters, such as in **Section 6.2.10**, the intrinsic values such as T1 relaxation time were extracted, rather than the image intensity.

3.3 Results

The results from the printing resolution and concentration tests are presented first, and these were used to inform decisions later in the phantom fabrication process. The results are also presented separately for the first iteration of phantoms, and the further developments that included patient-specific vessels.

3.3.1 Printing resolution tests

The results from the printing resolution tests showed that it was possible to print solid vessels down to a diameter of 1 mm. However, vessels with a diameter less than 5 mm did not print smoothly and excess material that was not part of the original design was left around the edges of the structure. Vessels that had a diameter less than 1 mm could not be printed; this was consistent with the size of the print core that is used to print the PVA material, which has a 0.8 mm nozzle. The results of these printing resolution tests for solid vessels can be seen in **Fig. 3.7**.

Hollow vessel structures could be printed, with an outer diameter as small as 3 mm. The hollow structures were, in general, smoother than the solid ones, which may have resulted from differences in the way the print was built up. A thinner vessel wall would dissolve more easily than a thicker one, so the minimum achievable wall thickness was investigated, and it was found that a vessel wall of 1 mm could be printed using the 0.8 mm Ultimaker 3 printing nozzles. The results from the tests with hollow structures can be seen in **Fig. 3.8**. The diameters quoted in the
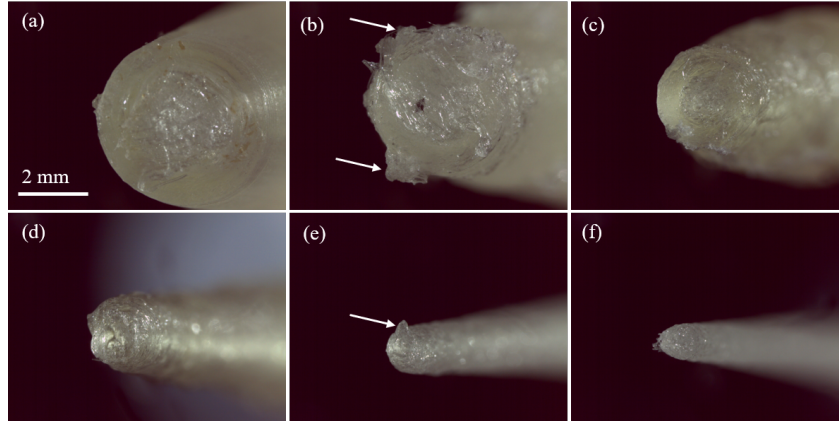
Figure 3.7: Resolution achieved of solid vessels printed with Ultimaker 3, with decreasing diameters (a) 5 mm (b) 4 mm (c) 3 mm (d) 2 mm (e) 1.5 mm (f) 1 mm. Scale bar applies to each image and arrows indicate excess printed material that was not part of the original design

figure are the values used to create the CAD models, but these were not actually achieved in the final print, due to limitations in the printing process. Below 3 mm, the vascular structures could be printed, but they were not hollow, as all the printed material joined together and produced a solid vessel. This can be seen in **Fig. 3.8(d)**, where the CAD model specified that the structure should have a 2 mm outer diameter and 1 mm inner diameter, but the printed structure was not hollow, and all the material had merged together.

3.3.2 Concentration tests

A schematic to show how the concentration test phantom was fabricated is shown in **Fig. 3.9**. This test phantom was imaged with both CT and MRI; the CT results are presented in **Fig. 3.9(a)** and the MRI results are presented in **Fig. 3.9(b)**. With increasing $BaSO_4$, there was an increasing CT signal and likewise, with increasing concentration of $CuSO_4$, there was an increasing MRI signal. The mean and standard deviation of image intensities for CT and MRI for each of the 12 samples are provided in **Table 3.1**. This shows that varying the CT contrast did not affect the MRI contrast, and vice versa, meaning that phantoms can be
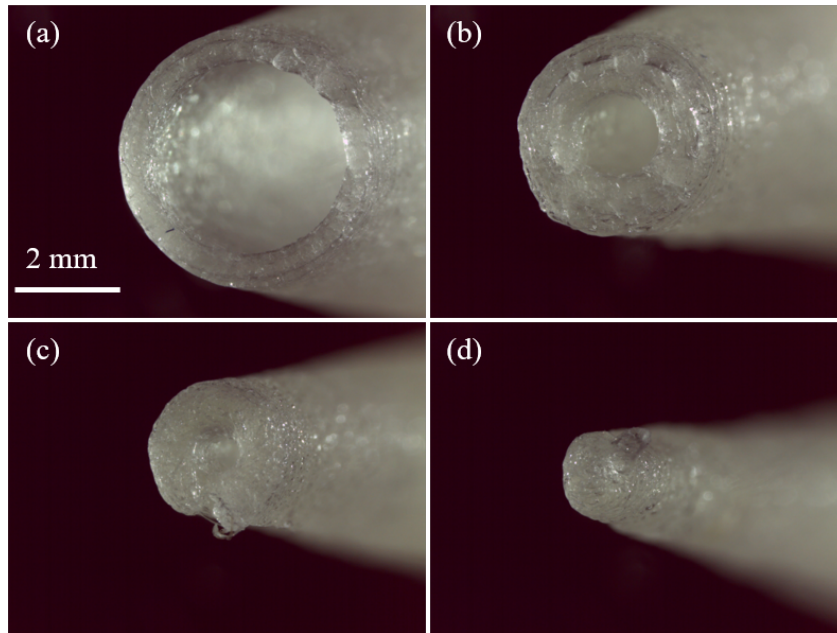
Figure 3.8: Resolution achieved for hollow vessels also printed with Ultimaker 3, with decreasing diameters and varying wall thicknesses (a) 5 mm outer diameter, 4 mm inner diameter, (b) 4 mm outer diameter, 2 mm inner diameter (c) 3 mm outer diameter, 1.5 mm inner diameter (d) 2 mm outer diameter, 1 mm inner diameter. Scale bar applies to all images

fabricated where the CT and MRI contrast are considered separately. From this test phantom, the concentrations to be used in phantom fabrication were chosen.
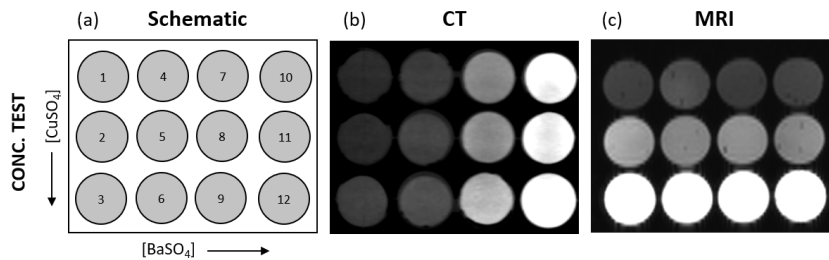
Figure 3.9: Images acquired with concentration test phantom (a) schematic to illustrate the phantom (b) CT imaging, where concentration decreases down each column (c) MRI imaging, where concentration increases across each row

Table 3.1: Average CT and MRI image intensities for the concentration test phantom samples

Sample no.	[CuSO$_4$]	[BaSO$_4$]	CT mean ± std	MRI mean ± std
1	0.01%	0.5%	0.2898 ± 0.0076	0.8517 ± 0.0524
2	0.1%	0.5%	0.3018 ± 0.0092	0.3323 ± 0.0285
3	1%	0.5%	0.3158 ± 0.0333	0.1083 ± 0.0161
4	0.01%	1%	0.3310 ± 0.0076	0.7516 ± 0.0396
5	0.1%	1%	0..385 ± 0.0083	0.2646 ± 0.0152
6	1%	1%	0.3611 ± 0.0111	0.1530 ± 0.0248
7	0.01%	5%	0.4818 ± 0.0117	0.7657 ± 0.0497
8	0.1%	5%	0.4988 ± 0.0170	0.2869 ± 0.0155
9	1%	5%	0.5907 ± 0.0385	0.1053 ± 0.0095
10	0.01%	10%	0.7631 ± 0.0681	0.8354 ± 0.0519
11	0.1%	10%	0.7213 ± 0.0498	0.2639 ± 0.0237
12	1%	10%	0.8487 ± 0.0417	0.1186 ± 0.0094

3.3.3   Manually designed phantoms

Using the novel fabrication technique described, wall-less ultrasound vascular phantoms were successfully fabricated. The straight vessel phantom is shown in **Fig. 3.10**, the stenosis phantom is shown in **Fig. 3.11** and the bifurcation phantom is shown in **Fig. 3.12**. The photo in **Fig. 3.10(a)** shows the finished phantom after one freeze-thaw cycle and the white opaque appearance of the solid PVA-c is apparent, whereas the photos in **Fig. 3.11(a)** and **Fig. 3.12(a)** show the phantom before the freeze-thaw process, so the aqueous gel can be seen. The yellow tape in all photos is a material that was used to hold the acrylic boxes together in place of glue, for ease of fabrication and re-use.

With ultrasound imaging, as shown in **Fig. 3.10(b)**, **Fig. 3.11(b)**, and **Fig. 3.12(b)**, the wall-less vessels were clearly visualised, with smooth walls. The hyperechoic regions around the vessel wall may be a result of some material being left behind after the printed structures were dissolved away if the vessels were not thoroughly flushed through with water. The size of the vessels as seen in the ultrasound images are consistent with the CAD designs, within 0.5 mm. There were some inhomogeneities in the background TMM, likely arising from inhomogeneous

mixing of the glass spheres, which were added for ultrasound contrast. This was mitigated in future iterations by sonicating the aqueous solution after the glass spheres had been added.
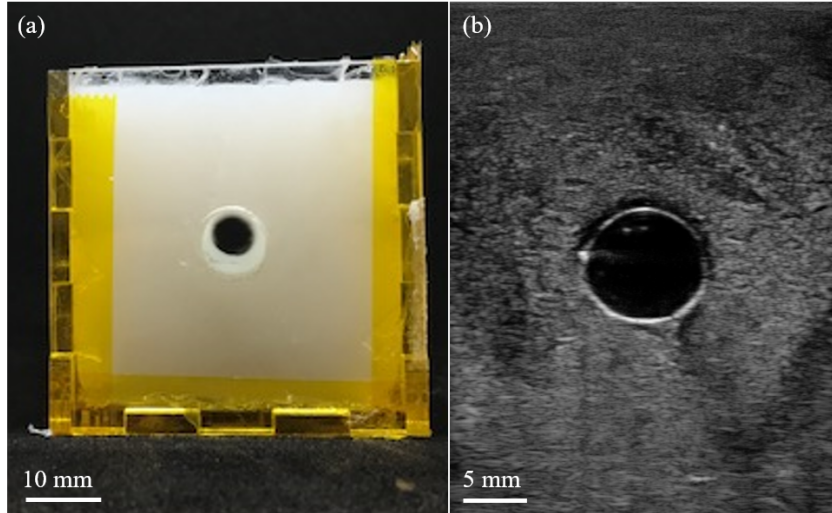
Figure 3.10: (a) Photo (end view) of straight vessel phantom after one freeze-thaw cycle. Yellow tape was used to hold the acrylic box together, for ease of fabrication and re-use (b) cross-sectional ultrasound image of the vessel
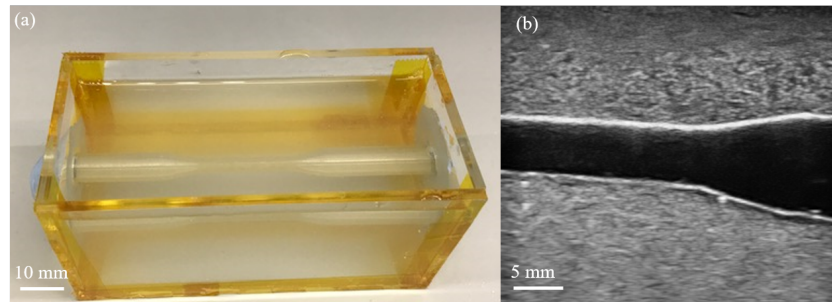
Figure 3.11: (a) Photo of stenosed vessel structure submerged in PVA-c, before one freeze-thaw cycle (b) longitudinal ultrasound image of the vessel

3.3.4 Patient-specific phantoms

External ultrasound imaging showed that the carotid artery phantom had be successfully fabricated. The TMM had a homogeneous speckled appearance, consistent with human tissue. The vessels structures could be clearly visualised and differen-
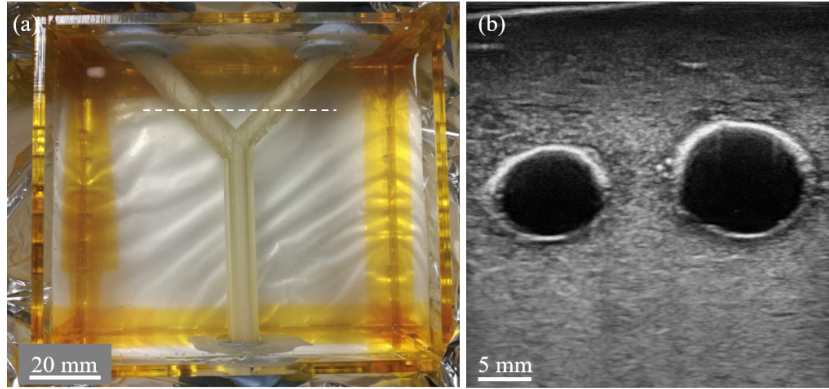
Figure 3.12: (a) Top view of the bifurcation phantom with aqueous PVA-c added, before one freeze-thaw cycle, with dashed line to indicate ultrasound imaging plane (b) cross sectional ultrasound image of the two vessels

tiated from the surrounding TMM. When measured on the ultrasound machine, the vessels had the same diameter as the printed structures, within 1mm, although these measurements were not formally recorded. A selection of ultrasound images from the carotid artery phantom can be seen in **Fig. 3.13**, including cross sections of the single vessel, the bifurcation point, and a plane where both vessel branches can be seen. It was also possible to visualise the vessel in a longitudinal plane, showing one branch and the slight narrowing at the bifurcation. The carotid artery phantom also had a realistic appearance with CT and MRI imaging, as seen in **Fig. 3.14**, where **(a)** is a schematic to highlight what the images are showing, **(b)** shows the CT image, and **(c)** shows the MRI image.

The coronary vessel phantom was imaged using both external and internal imaging techniques. External imaging modalities demonstrated that the phantom had been successfully fabricated, and internal imaging was used to test the phantom in a realistic clinical environment. The external imaging results can be seen in **Fig. 3.15**. The box created was slightly too large for the printed vessel structure, and so the holes needed to be plugged with Blu Tack, resulting in some distortion around the edges of the phantom. As with the previous phantom, with ultrasound the TMM had a homogeneous speckled appearance, and the two vessels could be
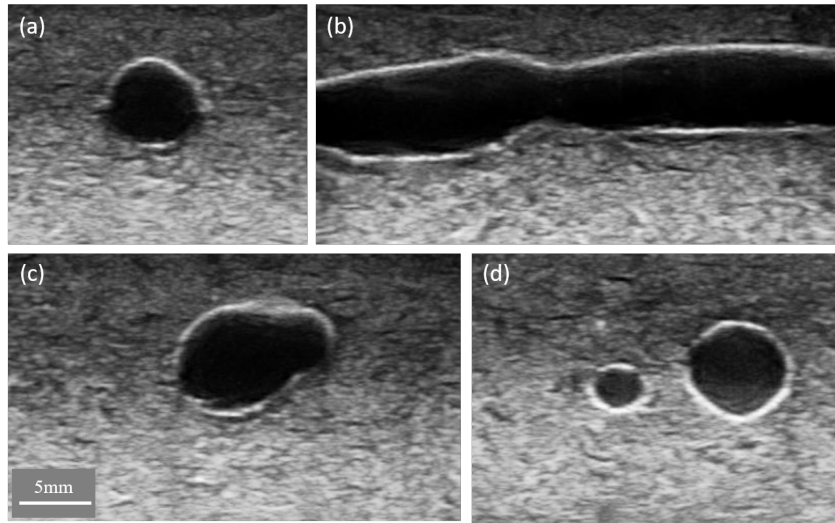
Figure 3.13: External ultrasound images of carotid artery phantom, showing wall-less vessels and homogenous background tissue mimic, (a) cross section of single vessel (b) longitudinal view of one branch (c) cross section at the bifurcation point (d) cross section showing both vessel branches
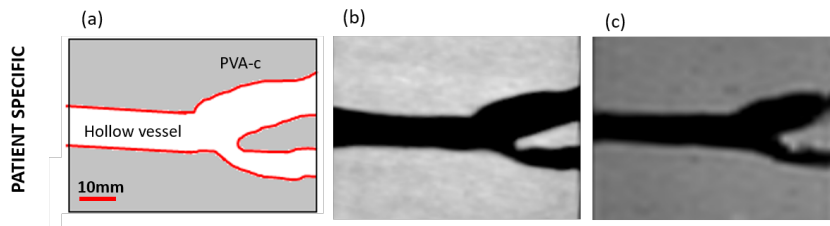
Figure 3.14: Multi-modality imaging of carotid artery phantom (a) schematic (b) CT imaging (c) MRI imaging, where some small bubbles can be observed in the background material

clearly and easily visualised.

The coronary vessel phantom was successfully imaged with IVUS in a hospital setting. This demonstrated that the phantom could be easily used in a clinical setting for clinical training, surgical planning, or testing new devices and techniques. The phantom had a realistic appearance with IVUS, and the TMM appeared homogeneous, with attenuation visually consistent with clinical images. The vessel and bifurcation into two branches, was clearly apparent. The vessel wall has a subtle appearance, as is seen in clinical images. The phantom was damaged by a sharp object during transportation, which manifested as an absence of signal near the
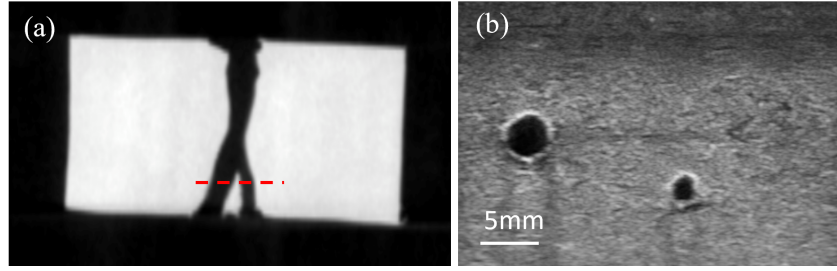
Figure 3.15: Multi-modality imaging of coronary vessel phantom (a) CT imaging, with dashed line to show ultrasound imaging plane. Distortion occurs at each end of the vessel, as the printed structure was smaller than the box it was encased it and therefore the hole had to be plugged with extra material (b) ultrasound imaging shows clearly the two wall-less vessels and homogeneous background

vessel, and this is highlighted by an arrow in **Fig. 3.16(c)**. Unfortunately, due to COVID restrictions, it was not possible to perform further IVUS imaging as part of this project.
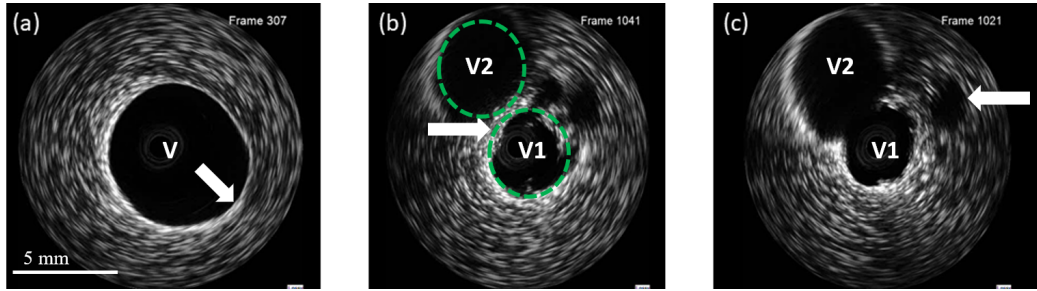
Figure 3.16: Intravascular imaging of coronary vessel phantom (a) straight vessel segment, with vessel (V) clearly shown (arrow: internal vessel wall) (b) separation into two vessels V1 and V2 (dashed green ellipses) at a bifurcation (arrow: TMM forming a wall between two vessels); (c) bifurcation of the two vessels (V1 and V2)with arrow highlighting a small hole created as a result of damage to phantom

3.4 Discussion

A method has been developed that enabled the fabricated of wall-less, vascular, patient-specific phantoms. The technique uses PVA in two different forms - both as a solid, 3D printing material and as an aqueous solution for forming the TMM. This method has the potential to overcome some of the challenges experienced with

previous phantom fabrication techniques, such as difficulty in creating complex or patient-specific structures.

In this work, three basic geometries were demonstrated, as a proof of concept: including a straight vessel, a stenosis, and a bifurcation. These geometries have been realised using prior techniques, but the simplicity of the novel method was demonstrated, and the resulting images were comparable with those achieved using alternative methods. The technique was then applied to real patient data, and patient-specific phantoms were created. The phantoms created were imaged using ultrasound, CT, and MRI. They were also shown to be compatible with IVUS imaging, and to the author's knowledge, this is the first example of patient-specific, intravascular imaging phantoms, using dissolvable vessels.

The phantoms presented here had a realistic appearance with both the external and internal imaging modalities. From this, it is possible to conclude that the combination of PVA-c and 3D printed PVA is a suitable method for creating wall-less, anatomically realistic, vascular phantoms. These phantoms can be used in a clinical environment, as was demonstrated here, and so could be used for clinical training and surgical planning. They are also highly relevant in the testing and development of novel medical devices, especially intravascular devices, as the phantoms have the capability to be attached to a flow set up, to simulate blood flow around the coronary vessels. As the phantoms have been demonstrated to be compatible with many of the imaging modalities used in computer assisted interventions, there is also the possibility of employing these methods to create phantoms that can be used to provide large imaging data sets, for instance for training machine learning models.

The novel method described is limited by the capabilities of 3D printing technology, although there have been improvements in these technologies since the start of this project. This is promising, and implies that smaller and more complex vascular structures could be achieved in future, and if a larger 3D printer was obtained, much

larger structures could also be replicated. Another limitation of the technique is the time frame required to produce a phantom. If two freeze-thaw cycles are required, it typically takes around two days to complete a phantom. In surgical planning applications, this time frame could be a limiting factor, but for clinical training it is unlikely to be problematic, and could be outweighed by the ease and cost effectiveness of the models. In future, a climate chamber could be used to have tighter control over the freeze-thaw process, and this could potentially be used to reduce the time frames involved, but experiments would need to be undertaken to investigate the effect of different conditions of the acoustic and mechanical properties of the final phantom.

The early stages of the work were presented, by the author of this thesis, at SPIE, and this was built on by other researchers, who used a similar technique, but coated the 3D printed vessel structures in paraffin wax, to prevent them dissolving into the TMM during the fabrication process. This is a useful alternative, as the material is easier to obtain than the parylene used here, however the coating was 0.1 mm thick, and if part of the coating was left behind in the phantom, it could cause image distortions. The authors also note that the use of a wax coating may lead to irregular surfaces in the vessel lumen, as it is difficult to coat the vessels evenly with the wax. Although the parylene coating method described here is more challenging and costly to replicate, it produces more consistent results and is simpler to implement successfully.

Self-healing, Nerve Block Ultrasound Phantoms

Table of Contents

This chapter builds on earlier work in **Chapter 3** and applies the technique described there for create patient-specific vascular phantoms, to enable ultrasound compatible nerve block phantoms to be created. These phantoms have patient-specific vasculature and can be used as clinical training tools, to simulate minimally invasive procedures in regional anaesthesia. The content here is been adapted from work that has been submitted to the International Journal of Computer Assisted Radiology and Surgery (IJCARS).

4.1   Introduction

Once the fabrication technique described in **Chapter 3** had been developed, it became clear that there were many applications in minimally invasive surgery where

phantoms created in that way would be highly useful. One such example is in regional anaesthesia, where nerve blocks are routinely performed but required complex and prolonged clinical training. Therefore, a collaboration was undertaken with an anaesthetist from University Collelge London Hospital (UCLH), Dr Simeon West, to further develop the work presented so far in this thesis, to enable the creation of ultrasound compatible nerve block phantoms.

4.1.1 Clinical background

Peripheral nerve blocks are routinely used in clinical practice for minimally invasive surgery and interventional pain management. They are an example of a regional anaesthesia procedure, which are becoming ever more important with the expansion of minimally invasive surgeries. Regional anaesthesia has been shown to have favourable outcomes compared with general anaesthesia, and results in lower rates of morbidity and mortality [81]. There are also economic benefits with undertaking minimally invasive surgeries using regional anaesthesia as it results in shorter hospital stays and lower costs.

A successful nerve block involves identifying the relevant nerve or plexus, inserting a needle into the surrounding area, close to the nerve or plexus and injecting local anaesthetic [82]. Real-time ultrasound guidance is the clinical standard for performing these procedures as this has been shown to have many benefits over alternative techniques for nerve localisation [83], including increased success rate, faster onset times and reduced rate of complications [84]. However, the skills required to successfully perform the procedure - including image acquisition, anatomical recognition and hand eye coordination - are complex, involve a steep learning curve, and can only be acquired with extensive training and practise [81].

For training in this procedure, it is generally agreed that the traditional apprenticeship model, where trainees observe a procedure and then attempt to perform one themselves under close supervision, is outdated [85]. This model can lead to

inconsistencies in the experience clinicians are able to require, and compromise patient safety [84]. Cadavers can be used as an alternative to training on patients, but there are many limitations with this model as well. For example, the formaldehyde used to treat cadavers affects the tissue properties, and those that are not treated do not last long; there is also a risk of infection. In addition, cadavers are rigid, which means it can be challenging to rotate the neck to access and visualise the plexus in that region. Cadavers are also expensive and have limited availability.

4.1.2 Technical background

For simulating peripheral nerve block procedures, meat-based phantoms are the simplest option. However, despite being inexpensive, meat-based phantoms can lack the anatomical realness of human structures and have a very limited lifespan. Non-meat based phantoms are an attractive alternative, although here it can be challenging to create an appropriate level of echogenicity in the phantom. If the phantoms have very low background echogenicity, it can enhance the needle visibility, providing an unrealistic simulation environment [86]. Commercial phantoms are also available, but these do not allow the replication of patient-specific anatomies, as they are usually based on generic models. These commercial models can also be prohibitively expensive and have a limited lifespan, due to the needle insertions damaging the model and forming tracks in the TMM.

There are four key qualities that phantoms need to have, for applications in regional anaesthesia and ultrasound guided nerve blocks. Firstly, they should replicate the appropriate properties of human tissue (such as echogenicity) and enable the visualisation of anatomical structures, such as nerves and vessels. Secondly, the phantoms should be affordable, or cost effective. Thirdly, they should be safe and non-toxic, so that they can be used in a clinical imaging environment. Finally, it should be possible to perform needle insertions on the phantoms, without it irreparably damaging the tissue mimicking material and preventing further use; the

phantoms should be opaque so that when these needle insertions are performed, the needle can only be visualised using ultrasound guidance, and cannot be seen from outside the phantom [86].

There is limited literature on the fabrication of peripheral nerve block phantoms. A common solution is to use meat such as chicken breast [87] or pork loin [88], with objects embedded in them to simulate nerves and vessels. However, phantoms made in this way cannot be stored and used repeatedly, and using solid objects as the nerves creates an acoustic shadow, which can limit visibility of the needle. Tofu has been used instead of meat, and although this is safer to use and lasts longer than raw meat, it does not have a realistic ultrasound appearance [89]. More recently, various hot dog sausages were used, embedded in gelatin [90]. The phantom was not resistant to damage as a result of needle insertions, but the authors explain that the tracks left by the needle can be eliminated by microwaving the phantom. However, this may not be practical for clinical training, and gelatin is not a highly durable material, so is likely to become damaged with repeated use. The majority of nerve block phantoms in the literature also have limited anatomical realism, and do not simulate patient-specific anatomies.

The literature shows that there is a need for a low cost, nerve block ultrasound phantom that has self-healing properties and could be used in clinical training for ultrasound guided nerve block procedures. Therefore, the aim of this chapter is to create such a phantom, by building on techniques developed earlier in the thesis. The main requirements of this phantom are that ultrasound imaging can be used to visualise realistic anatomies, including nerves and vascular structures. In addition, the phantom should also have the capacity to be used to simulate a nerve block procedure, include needle insertions and hydrodissection, and be self-healing so that this can be done repeatedly in the same phantom. As a proof of concept, a nerve block phantom is created based on the brachial plexus, as this is a common clinical target for nerve blocks, so important for clinical training, and can be compared with

the commercially available 'Blue Phantom'. Polyvinyl alcohol cryogel (PVA-c) was used as the tissue mimicking material (TMM), due to its favourable properties, which were discussed in **Chapter 2**.

4.2 Methods

The first stage of this work involved testing the self-healing properties of the chosen TMM material, PVA-c. Using the results from these tests, a phantom was then fabricated that included a patient-specific carotid artery, a vein, and multiple nerve structures. In clinical practice, with ultrasound imaging, nerves either appear hyperechoic or hypoechoic, depending on their location within the body (**Fig. 4.1**). This work demonstrated the creation of both hyperechoic and hypoechoic nerves, meaning the method can be tailored depending on the intended application and nerve or plexus of interest.
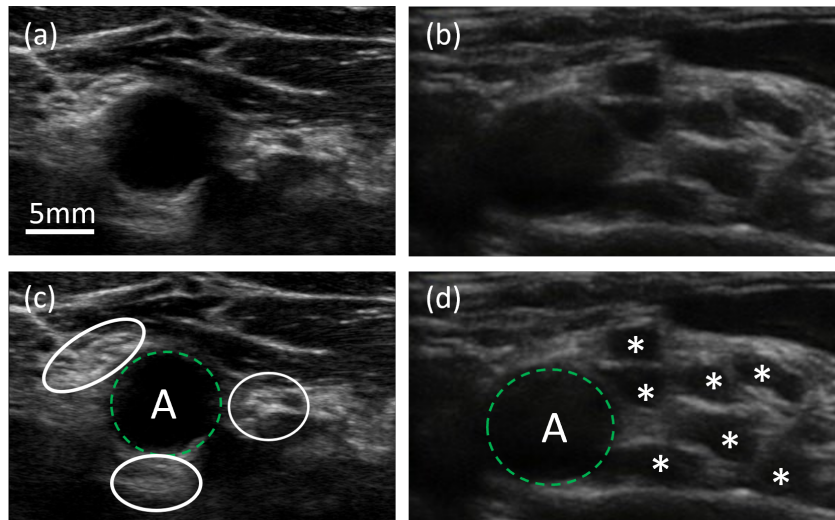
Figure 4.1: Ultrasound imaging of human nerves in vivo (a) example of hyperechoic nerves (b) example of hypoechoic nerves (c) marked up version of image in *a* to highlight artery (A) surrounded by the lateral, median, and posterior cord, which are hyperechoic nerve bundles (white ellipses) (d) marked up version of image in *b* to show artery (A) surrounded by brachial plexus divisions, which appear hypoechoic (*)

4.2.1   Self-healing tests

An initial test was undertaken, to investigate the self-healing properties of the TMM, and inform the choices for the phantom fabrication process. For this, three versions of a PVA-c phantom with the same geometry were created. The phantom was very simple and had only a single wall-less vessel, surrounded by PVA-c, so that there was a landmark for ultrasound imaging. These simple phantoms were created using methods described in **Chapter 3**. The three phantoms had varying levels of glass microspheres (53 - 106 μm) added to them, so they each had a different level of background echogenicity, to test the effect of the self-healing capabilities, and to investigate which would be most appropriate in the final nerve phantom. The first phantom had no added glass microspheres, the second had 0.05% w/w glass microspheres, and the third had 0.5% w/w glass microspheres.

Once the phantoms had undergone two freeze-thaw cycles, they were (one at a time) fixed into a water bath for imaging with ultrasound. A clinical scanner (MDP Ultrasonix, Richmond, Canada) and linear array probe (14-5 MHz) were used in this case. The ultrasound probe was fixed using a translational stage, so that it was in contact with the phantom surface, in a plane where the vessel could be visualised. A 22G needle was inserted into the phantom and care was taken to ensure the needle was also in plane. An image was then taken during the needle insertion, and directly after, to see if any tracks were left in the phantom.

4.2.2   Phantom fabrication

A schematic was drawn up, based on human images and advice from clinicians, to outline the proposed structure of the nerve phantoms. This schematic was sent to the clinician (Dr Simeon West) for feedback, and subsequently annotated to communicate thoughts on the geometry and depths of the structures included, to ensure the phantom would have enough clincal relevance. The schematic underwent multiple iterations during the planning stages of this work, and the final version,

that was used to create the phantoms here, can be seen in **Fig. 4.2**.
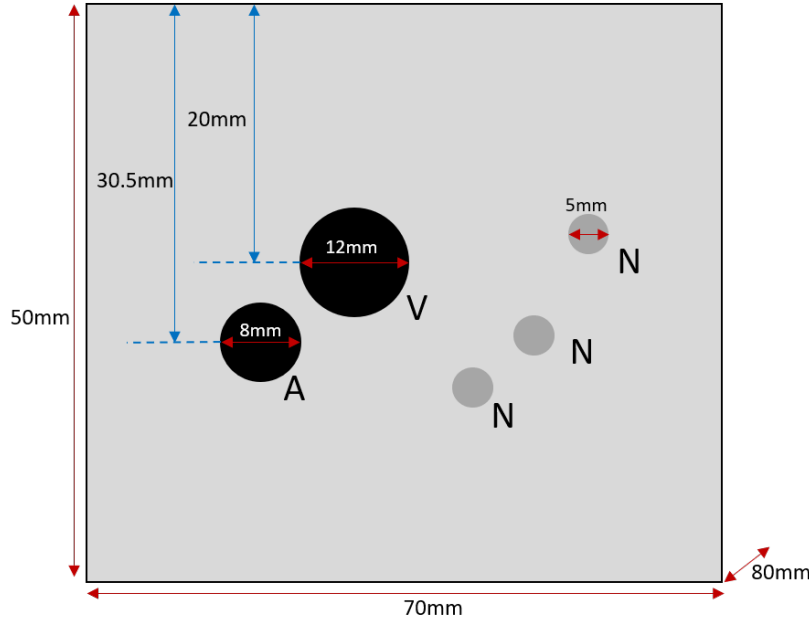
Figure 4.2: Final schematic of nerve phantom, with patient-specific artery (A), vein (V), and three hyperechoic nerves (N)

Once the geometry of the phantom had been decided on, the first step of the fabrication process was to create the PVA-c that was to be used as the TMM. A 10% w/w solution of PVA-c was made, by mixing the PVA with deionised water, as described in **Chapter 3**. To the aqueous solution, 0.5% w/w potassium sorbate was added as a preservative; potassium sorbate is used as a food preservative so is safe to use. The solution was left to cool and stored in airtight containers until needed later in the fabrication process.

The wall-less vasculature structures were fabricated using the methodology previously described in **Chapter 3**. To demonstrate the feasibility of including patient-specific structures in the phantom, a segmented patient-specific carotid artery was obtained from an online repository (GrabCAD, Cambridge, Massachusetts, United States; https://grabcad.com) and 3D printed in PVA. This form of PVA is different to the cryogel material used later for the TMM; it is a solid plastic, often used as a support material in 3D printing, as it is water soluble. The vein structure was

drawn manually using computer aided design (CAD) software (Autodesk Fusion 360, Autodesk Inc., San Rafael, California, United States), and also 3D printed in PVA. All 3D printing in this work was performed using the commercially available Ultimaker 3, (Ultimaker, Utrecht, Netherlands).

To create the hyperechoic nerve structures, negative moulds were drawn in CAD software and 3D printed in polylactic acid (PLA). A portion of the PVA-c was measured out, and 1% w/w glass microspheres (53 - 106 µm) were added. The mixture was sonicated to ensure homogeneous mixing of the glass spheres. This mixture was poured into the nerve moulds, which then underwent two freeze-thaw cycles. At the end of the freeze-thaw cycles, the nerve structures were removed from the moulds. These nerves had a 5mm diameter, as using this fabrication method, it was challenging to create nerve structures with smaller diameters.

The phantom was assembled by placing the carotid artery, vein, and nerve structures into a laser cut box. The remaining PVA-c was mixed with 0.5% glass microspheres, sonicated, and poured over the structures within the box. The whole phantom subsequently underwent two freeze-thaw cycles, to change the aqueous PVA-c solution to a solid material. Once the freeze-thaw cycles were completed, the phantom was submerged in water for 24 hours, to allow the 3D printed vessel structures to dissolve.

To create the alternative anatomy with hypoechoic nerves, the nerves were created as wall-less structures, rather than by using the negative moulds described above. This was achieved by placing solid rods at the desired location of the nerves, and removing the rods when the phantom had undergone the full freeze-thaw cycles. In this case, it was possible to create nerves with a smaller diameter, and these were 3mm.

4.2.3 Testing peripheral nerve phantoms

Ultrasound images of the peripheral nerve phantoms were acquired at UCLH, using a clinical scanner (Sonosite S2, Bothell, Washington, United States) and a high frequency linear probe (13-6 MHz). An anaesthetist (Dr Simeon West) performed the imaging and needle insertions, to ensure they were done correctly and in a clinically realistic manner. This also made it possible to get live feedback as to the mechanical and acoustic realism of the phantoms, from a clinician who regularly performs the nerve block procedures. All phantoms were submerged in water for imaging, to allow for coupling between the probe and the TMM and to remove air from the wall-less vessels.

In addition to ultrasound imaging, the peripheral nerve phantoms were used to simulate needle insertions and hydrodissection, under ultrasound guidance. This was also performed by Dr Simeon West. Clinical needles were used, including both 18 G and 22 G. To simulate hydrodissection, water was injected into the phantom, in close proximity to the nerve.

4.3 Results

4.3.1 Self-healing tests

These initial tests showed that when needle insertions were performed on PVA-c with no added backscatterers, large artefacts were observed, making it challenging to accurately localise the needle tip within the material (**Fig. 4.3a**). With no added backscatterers, the needle also left obvious tracks within the TMM (**Fig. 4.3b**) for ultrasound imaging, and these took up to a week to disappear. The artefacts and presence of tracks means that with PVA-c with no added backscatterers is not suitable for creating clinical training phantoms where needle insertions are required. Once backscatterers were added into the PVA-c however, phantoms had the ability to heal, or at least obscure any visible damage to the phantom, so that the needle
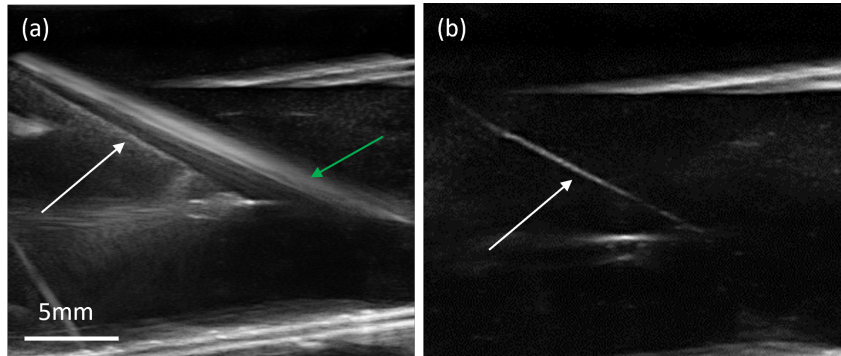
Figure 4.3: Self-healing test for phantom with no added backscatterers, (a) during needle insertion; white arrow points to the needle and green arrow points to the artefact (b) after needle insertion; white arrow points to track left by needle

tracks were not visible with ultrasound imaging after the needle had been removed. This was demonstrated even with a low amount of backscatterers (0.05% w/w). As shown in **Fig. 4.4**, with this concentration of glass microspheres, the needle did not leave any visible tracks in the material once it had been removed. There is an artefact in the images in **Fig. 4.4**, but it is thought to be a result of reflections from the bottom of the imaging tank, rather than by the needle in this case. In future, an absorbent material could be used to line the bottom of the imaging tank to prevent such artefacts. The phantom with 0.5% w/w backscatterers produced the
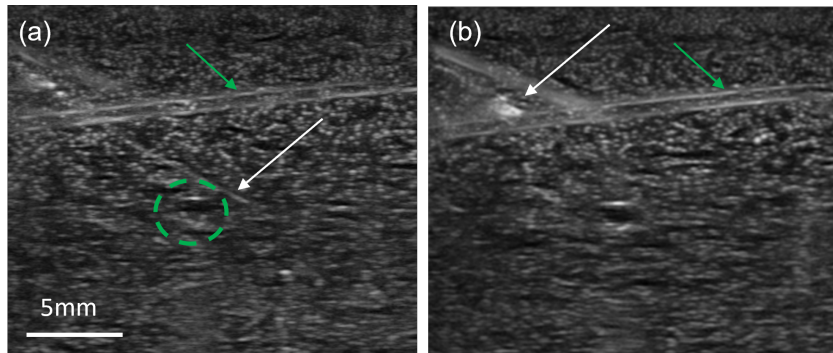
Figure 4.4: Self-healing test for phantom with 0.05% backscatters, with white arrow pointing to needle tip and green arrow pointing to artefacts (a) during needle insertion with dashed green line to highlight wall-less vessel (b) after needle removal, with no visible needle tracks behind the needle tip

most favourable results. The background material had a homogeneous appearance,

and images were acquired without any artefacts. As seen in **Fig. 4.5**, the needle could clearly be visualised within the phantom, and immediately after removal of the phantom, there was no visible damage to the TMM. The ultrasound probe was fixed during the imaging process to ensure the images were all acquired in the same plane, but once these had been taken the probe was also released from the translational stage, so that imaging could be performed in various different planes, to confirm that the lack of needle tracks was not due to a misaligned imaging plane.
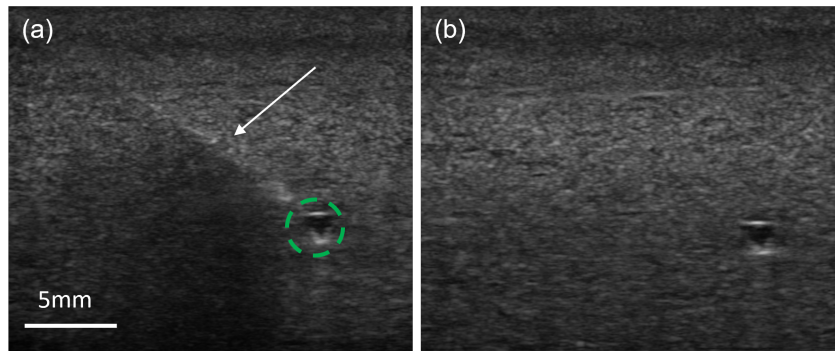
Figure 4.5: Self-healing test for phantom with 0.5% w/w glass microspheres, (a) during needle insertion, with arrow to highlight needle location (b) after needle removal with no visible tracks

4.3.2 Peripheral nerve phantom

Ultrasound imaging showed that the phantom had been successfully fabricated (**Fig. 4.6**). The TMM had a homogenous speckled appearance, consistent with human tissue, and the vessel structures could be clearly visualised. The nerves were visualised as either hyperechoic (**Fig. 4.6**) or hypoechoic (inset of **Fig. 4.6**), which demonstrated that both anatomical presentations could be replicated within the phantom. It was challenging to fabricate hyperechoic nerves with diameters less than 5 mm, but with the hypoechoic anatomy, nerves were successfully created with 3 mm diameters. However, in both cases the nerves were clearly visualised with ultrasound, and there was no shadowing underneath the structures, as was

seen in other phantoms in the literature. Ultrasound guided needle insertions were
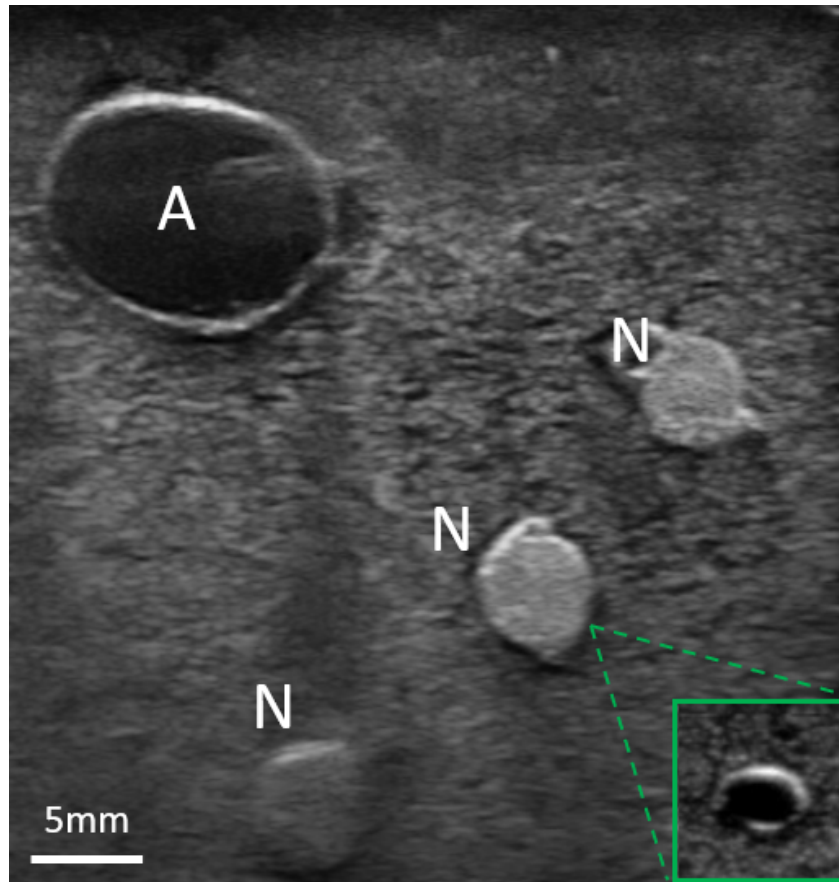
Figure 4.6: Ultrasound imaging of nerve phantom with artery (A), hyperechoic nerves (N) and inset (green box) to show alternative appearance of hypoechoic nerves. A vein was also included in the phantom, but cannot be seen in this image

successfully performed on the phantom. The insertion of a 22G clinical needle into the phantom with hyperechoic nerves is shown in **Fig. 4.7**. It was possible to visualise the needle in a realistic manner. The material gave a suitable resistance to the needle, to simulate insertion into human tissue, although there was not a strong amount of resistance at the surface to simulate the needle initially penetrating the skin. With the needle, it was possible to feel around the nerves and the boundary of the wall-less vessels. Longitudinal ultrasound imaging (**Fig. 4.8**) shows that it was possible to penetrate the vessels. When the needle was subsequently removed, there was no visible damage to the vessel wall, implying that these phantoms could
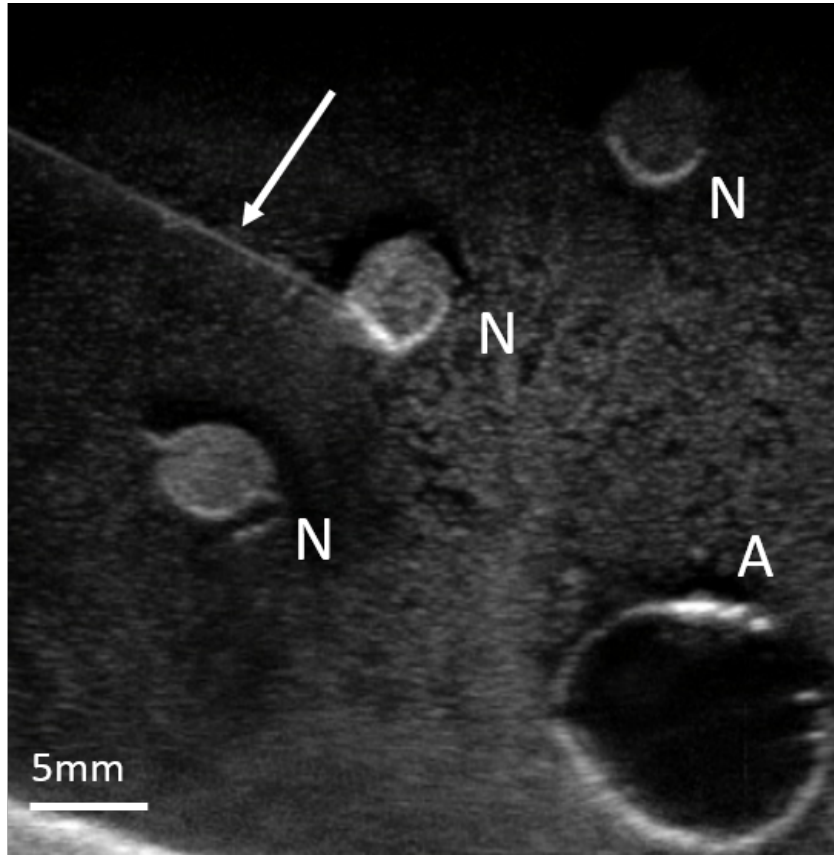
Figure 4.7: Insertion of 22G needle into hyperechoic needle phantom, showing nerves (N), artery (A) and needle (arrow)

be used repeatedly, for clinical training. The needle also did not leave any visible tracks in the background material, again showing that the phantom is suitable for repeated uses. When penetrating the vessel wall, there was a realistic level of resistance, and the operator could feel when the needle had passed through into the wall-less space. The needle was used to simulate hydrodissection, and inject water into the area surrounding a nerve (**Fig. 4.9**). The results show that this was also successfully achieved. The injection of water could be clearly visualised with ultrasound imaging (**Fig. 4.9(1, 2)**) and the nearby nerve was momentarily deformed in response to the injection. The injected liquid quickly dissipated, as is seen in clinical practice, and there was minimal evidence of the procedure 10 seconds after the initial injection (**Fig. 4.9(3)**).
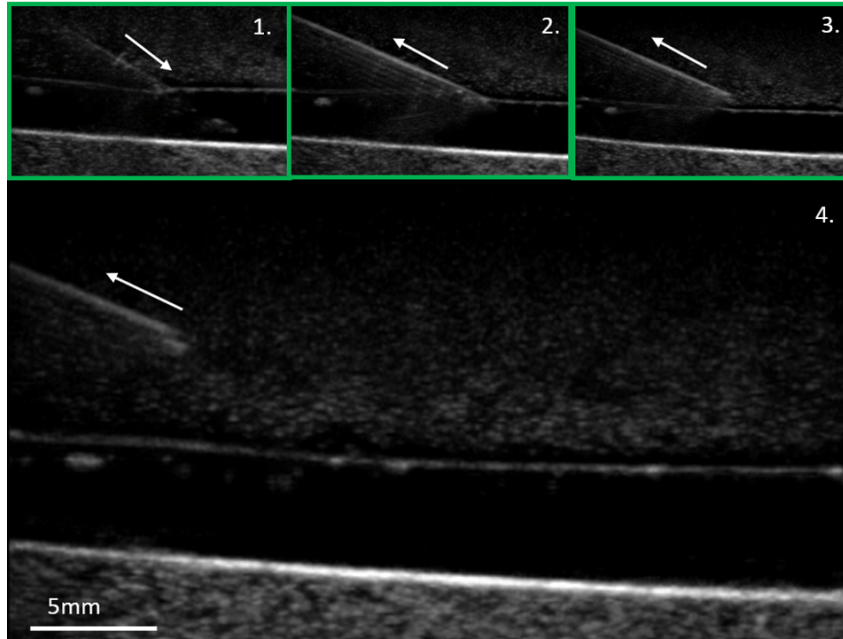
Figure 4.8: Vascular puncture leaves minimal damage to vessel structure. Ultrasound images show 22G needle puncturing vessel (1) and subsequent removal (2-4)

4.4 Discussion

In this chapter, a novel fabrication method is demonstrated, that enables a self healing, ultrasound compatible peripheral nerve phantom to be created. The method uses a combination of 3D printing techniques to create moulds and dissolvable vessel structures, and PVA-c as the TMM. This phantom has the potential to be used as a clinical training phantom in regional anaesthesia, for ultrasound guided nerve block procedures, as it can be used to simulate needle insertions and hydrodissection in addition to ultrasound imaging. The phantom shown here uses a patient-specific carotid vessel structure, but the methodology could be extended to include patient-specific structures for the nerves and vein as well.

As a result of the self-healing properties of PVA-c, the phantoms created using this novel fabrication method can be used to simulate needle insertions, without irreparably damaging the phantom. No noticeable tracks were left in the TMM after needle insertions were performed, which means these phantoms can be used multiple
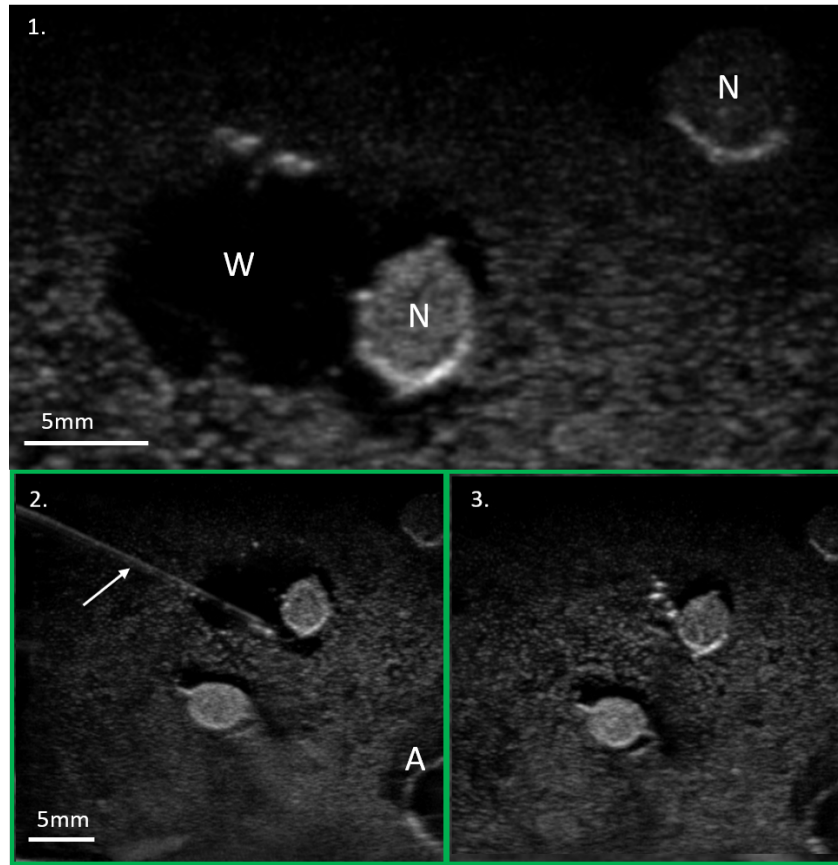
Figure 4.9: Hydrodissection of nerve, (1) during injection of water, (2) immediately after injection, (3) 10 seconds after initial injection, with nerves (N), artery (A), injected water (W) and needle (arrow)

times so they are cost effective. It was also possible to perform hydrodissection in the phantom, and the injected liquid quickly dissipated, as is seen in clinical practice.

There is a limited variability in the soft tissue structures of the phantom shown. For example, there is no differentiation between the skin surface and the tissue beneath, and in clinical practice this layer of skin gives a feeling of resistance during needle insertions. However, the practitioner (Dr Sim West) reported that there was a realistic feeling during needle insertions once inside the phantom, and it was possible to identify when the needle passed through the wall of a vascular structure, into the wall-less space beyond. It was also possible to feel the space around nerves with the needle. In future work, the phantom could be extended to include a more

realistic skin surface, and the framework presented could easily be extended to include other structures such as the tendons.

The method described aims to overcome challenges of previous nerve phantoms, including the longevity and anatomical realism. Using PVA-c as the TMM, a realistic background echogenicity was achieved, where it was possible to identify the nerve under ultrasound guidance. However, the visibility of the needle was also not overly enhanced as seen in previous phantoms, which is beneficial, as training on such phantoms can give a false confidence in clinical ability during training. The use of PVA-c as the TMM, in combination with preservatives means that it can be kept for months at a time.

The definition of cost-effectiveness for phantoms varies, depending on geographical location and clinical context. Despite this, the longevity (thanks to lack of visible damage after needle insertions), and low cost materials used in the phantoms described here, means that they are relatively cost-effective in most contexts, which has been a challenge with alternative phantoms. The estimated cost of the nerve presented phantoms here is discussed below, although the labour costs are not included in the estimate. These labour costs would again vary depending on the context.

The one-time costs required to set up a laboratory with all the equipment required is estimated to be around £8,000, and the costs included in this estimate are itemised in **Table 4.1**. The cost of the materials required to make an individual phantom would vary slightly, depending on the size and geometries used. An itemised estimate of the cost of creating the hyperechoic nerve phantom with patient-specific carotid artery developed in this chapter is presented in **Table 4.2** and is estimated to be around £30. This is considerably more affordable than a comparable commercial regional anaesthesia phantom, such as the Blue Phantom model, which is £725 (purchased here [91]) and the phantom paradigm presented in this thesis allows for flexibitlity and personalisation that is not afforded with the

Blue Phantom models.

All the items listed in the estimates are the exact models used in this thesis. The Ultimaker 3 printer can be bought from 3dgbire [92], and the water bath and electronic stirrer from IKA (water bath here [93] and stirrer here [94]). The PLA and PVA for 3D printing can be bought from RS Components (PLA here [95] and PVA here [96]) and the PVA powder used to create the PVA-c TMM can be bought from Sigma Aldrich (here [97]). The general supplies required to set up the laboratory, and laboratory supplies required per phantom are quoted as an estimate, based on experience within the laboratory, but this very difficult to accurately quantify. These general costs would likely not need to be considered in a well-established research centre, but could be more significant in low resource settings. The initial, single purchase costs could be significantly reduced by choosing cheaper items; for example, the water bath used here was highly expensive, as it was already owned by the research centre where this work was conducted. Cheaper alternatives are readily available (e.g. £44.99 from Amazon [98]) and would likely produce the same outcome.

Table 4.1: Cost of the single purchase items required to make a phantom

Item	Price
3D printer (Ultimaker 3)	£2983.50
Water bath (HBR4 control, IKA)	£3833
Electronic stirrer (Eurostar Digital 20, IKA)	£1076
General supplies (e.g beakers)	£100
Total	£7992.50

Table 4.2: Cost of materials for a single hyperechoic nerve phantom. A unit refers to the purchased quantity.

Item	Price /unit	Price /phantom
PLA for 3D printing	£10.96 (0.3 kg)	£2.08
PVA for 3D printing	£47.68 (0.5 kg)	£0.57
PVA powder	£116 (1 kg)	£23.20
Lab supplies (e.g BluTack)	-	£5
Total	-	£30.85

In conclusion, the phantom technique developed here allowed the creation of a successful nerve block phantom that could be used for clinical training in regional anaesthesia, to simulate ultrasound guided interventions. The materials used are affordable and the paradigm could easily be adapted to replicate other patient-specific geometries or pathologies, and complexity within the phantom could be increased as training progresses. The anatomically realistic, self-healing phantoms described in this chapter would be useful in a variety of applications where needle insertions are performed under ultrasound guidance, including musculoskeletal injections, interventional and breast radiology, along with oncological biopsy and other tissue sampling.

Photoacoustic Imaging Phantoms

Table of Contents

This chapter describes the role of photoacoustic imaging (PAI) in minimally invasive surgeries and gives a brief overview of the recent progress in this field, including its potential for use in imaging peripheral nerves, and related applications in regional anaesthesia. This literature review was published in a book chapter (Mackle *et al.* 2020 [99]). To further develop the field of PAI, suitable imaging phantoms are required, and so the rest of this chapter focuses on using the techniques developed earlier in this thesis to create PAI phantoms and investigate their capabilities for applications in minimally invasive surgery.

5.1   Introduction & literature review

The overall concept of PAI was covered in the background of this thesis, in **Chapter 2**. As previously mentioned, it is a relatively new imaging modality, which has shown promise in applications in minimally invasive surgery. It has been demonstrated in several studies that PAI can be used to visualise human peripheral vasculature in vivo, including vessels in the human palm [100, 101, 102] and arm [103]. However, translation to clinical practice remains a challenge for PAI systems, primarily due to limited imaging depth capabilities of current systems.

From a translational standpoint, both the size and the cost of PAI systems are important factors. This consideration has led to interest in light emitting diodes (LEDs) as PAI excitation sources [104, 105]. However, a prominent challenge associated with using LEDs is that they tend to have much lower pulse energies than conventional excitation sources, such as Q-switched Nd:YAG pumped optical parametric oscillators (OPOs), and so the ultrasound signals are correspondingly weaker. Pioneering work by Hansen [106] demonstrated the feasibility of LED-based PAI, and Allen and Beard [107] investigated the use of LEDs for biomedical applications. Recently, LEDs have been integrated alongside a clinical, handheld imaging probe as part of a commercial system (CYBERDYNE INC., Tsukuba, Japan) [108]. In this system, an LED array is positioned on each side of the imaging probe, angled so that their axes of illumination intersect the ultrasound imaging plane. B-mode ultrasound images and photoacoustic images can be acquired sequentially, with photoacoustic information overlaid onto the ultrasound images in real-time.

In order to develop these PAI systems efficiently, and make them effective for clinical practice, suitable phantoms are required. The requirements of such phantoms are very similar to those described earlier in this thesis, and so the phantom fabrication techniques developed earlier applied, to investigate the feasibility of using these phantoms for PAI. One area of interest when attempting to use these phantom fabrication techniques for PAI was what depths it was possible to pen-

etrate to and receive signal from, as a significant limitation of PAI is the shallow penetration depth. A second point of interest was whether it was possible to visualise needles within the phantom, as needle insertions are a prominent area of interest for applying PAI in clinical practice.

5.1.1 Applications of LED-based PAI for minimally invasive procedures

LED-based PAI may be well suited to guiding minimally invasive procedures that are targeted at peripheral blood vessels or nerves. In current clinical practice, B-mode ultrasound guidance is used to visualise both anatomical structures and invasive medical devices. Procedures that use ultrasound guidance include peripheral venous access, peripheral arterial access, biopsies, nerve blocks, and interventional pain procedures. In expert hands, B-mode ultrasound imaging can provide reliable identification of a variety of structures, including nerves, arteries, and veins. However, none of these structures have a unique ultrasound appearance with B-mode imaging; the reflected ultrasound waves are dependent upon the mechanical properties of the tissue and the angle of insonation, so misidentification of tissues is common. In these contexts, LED-based PAI could be useful in a variety of ways. Firstly, it could help to identify procedural targets, such as blood vessels or nerves. Blood vessels can be visualised directly with PAI due to the presence of haemoglobin in red blood cells, with excitation wavelengths spanning visible and NIR wavelengths. Likewise, direct image contrast for nerves and surrounding adipose tissues can be obtained with specific NIR wavelengths where optical absorption by lipids is prominent [109, 46, 45]. Secondly, LED-based PAI could be used to avoid damaging critical structures or puncturing arteries. Finally, it could be used to localise invasive devices relative to external imaging probes.

5.1.2   LED-Based Photoacoustic Imaging of Vasculature

Several studies have explored the use of LED-based PAI to image superficial human vasculature. In the study of Xia *et al.* [48], the human finger and wrist were imaged, and strong PA signals from subsurface vascular structures in both imaging locations were observed. This study showed relatively strong visual correspondence between ultrasound and PAI modalities, although the authors noticed distinct differences between the features visible with ultrasound and those visible with PAI. In another study by the same group, it was shown that LED-based PAI could provide sufficient depth and resolution to image superficial vasculature, such as the digital vessels [110]. These results suggest that LED-based PAI might be useful clinically for identifying, avoiding, or targeting superficial vasculature.

Maneas *et al.* used an LED-based system (AcousticX, CYBERDYNE INC., Tsukuba, Japan) to image placental vasculature, in the context of foetal medicine [111]. They imaged post-partum human placentas ex vivo and were able to detect superficial blood vessels with PAI that were not apparent with ultrasound alone. They compared images acquired from this system to those acquired from a Fabry-Pérot based system and concluded that the two systems were complementary: the former allowed for rapid 2D PA and B-mode ultrasound imaging, whilst the latter yielded finer detail.

To guide vascular access procedures, PAI devices would need to visualise vessels to depths of 40 mm or more; this would ensure they are suitable, even for patients with a high body mass index (BMI). For vascular access applications, imaging vessels with diameters greater than 2 mm would be necessary. However, it would also be useful to identify vessels with much smaller diameters and to ensure that collapsed vessels and those parallel to the imaging plane can be seen. Visualising these vessels could improve the safety of minimally invasive procedures by enabling clinicians to avoid vascular structures where necessary.

Beyond identifying human vasculature, distinguishing between arteries and veins

is a prominent clinical objective, particularly in the context of avoiding puncturing arterial structures when targeting veins. In current clinical practice, this can be challenging. Ultrasound-guided clinical procedures that involve percutaneous access to vessels would benefit from enhanced visualisation of arterial and venous structures. For instance, with central venous access, misidentification of arterial structures can lead to catastrophic bleeding; the risk of arterial puncture has been estimated to be as high as 6% [112]. The addition of imaging modalities such as colour ultrasound Doppler imaging can help to discriminate pulsatile blood flows, which are indicative of arterial blood. Nonetheless, arterial puncture is still a risk [47], with many underlying factors. Higher risk procedures include those where the vasculature is too small to identify using ultrasound, as well as ones in low-flow or no-flow states where Doppler imaging has limited utility, which can occur when patients are in shock or cardiac arrest.

LED-based PAI is promising for differentiating between arterial and venous structures, based on differences in the optical absorption spectra of oxy- and deoxy-haemoglobin. Zhu *et al.* explored the use of LED-based PAI to quantify blood oxygenation levels in a human volunteer [44], using two dual wavelength LED bars emitting alternatively at 690 nm and 850 nm. Their high imaging frame rates, which reached 500 Hz, could be well suited to visualising rapid changes in oxygenation levels. Additionally, LED-based PAI provided dynamic measurements of vasculature resulting from cuff occlusion [110]. The authors of that study discussed how LED-based PAI imaging of superficial vasculature could potentially be used in clinical settings to measure diagnostic parameters such as the heart rate and recovery time from cuff occlusion.

5.1.3 Prospects for LED-based photoacoustic imaging of peripheral nerves

Many types of needle-based procedures could benefit from enhanced visualisation of nerves, including the nerve block procedures described in **Chapter 4**, where accurate and efficient identification of nerves is essential. Imaging nerves is challenging, as their appearance can mimic other structures such as tendons [113]. Nerves also exhibit anisotropy, so their appearance is strongly dependent on the angle of insonation. Despite its advantages for visualising neural structures, the resolution of B-mode ultrasound can be insufficient to consistently recognise smaller branches, which are increasingly of clinical interest. If PAI could provide enhanced visualisation of small superficial neural structures, there would be strong potential to improve procedural outcomes.

The use of LED-based PAI for visualising nerves during minimally invasive procedures has remained elusive. The use of PAI with conventional excitation light sources to image nerves has been explored to a limited extent. Ex vivo pilot studies indicate that PAI may provide higher contrast for nerves than that obtained with B-mode ultrasound, and that it could be useful for differentiating nerves from tendons [114]. Even with high energy sources such as OPOs, when excitation light is delivered from the tissue surface, obtaining sufficient signal from lipids at clinically relevant depths is challenging. One solution, which may be relevant to future implementations of LED-based PAI, can be found with interventional PAI, where excitation light is delivered through a needle to reach targets several cm beneath the surface [115, 116, 117, 118]. With an LED-based PAI system, either identifying nerves as procedural targets or as structures to avoid could be useful, depending on the clinical context. Ideally, nerves could be visualised at depths up to 60 mm with these systems. As this could be very challenging, given the relatively low pulse energies of LEDs, visualisation of nerves to depths of 30 mm would still be useful.

Imaging of percutaneous devices such as needles and catheters using ultrasound

can be challenging. As a result, identification of the needle tip is vital to prevent damage to underlying structures. With steep insertion angles, ultrasound waves are reflected away from the transducer, and so the needle is not visible. In addition, catheters can be very poorly visible when positioned in soft tissues. Visualising needles or catheters is another area where LED-based PAI could be very useful, and the combination of PAI with current ultrasound techniques could provide better real-time guidance. In a study by Xia *et al.* [48], the performance of LED-based PAI for guiding needle insertions was evaluated for the first time. Using an ex vivo blood mimicking phantom, needles were visualised to depths of 38 mm. At insertion angles of 26 to 51°, the signal-to-noise ratio (SNR) achieved was 1.2 to 2.2 times higher than that measured with B-mode ultrasound alone; the SNR decreased as the needle insertion angle increased. Although the spatial resolution was similar for both ultrasound and PAI, the inserted needle was visible down to 2 cm with PAI, but it was barely visible with ultrasound. In a second study by Xia *et al.* [119] medical devices were coated with a carbon nanotube polydimethylsiloxane composite to enhance visibility for PAI. In this study, two experiments were performed: first, a metal needle was inserted into chicken breast and in the second, a catheter dipped in the composite coating was put into the chicken breast. In both cases, the devices were barely visible with ultrasound, but were visible with LED-based PAI. The uncoated and coated needles were visible to depths greater than 20 mm and 30 mm, respectively.

5.1.4 Challenges for clinical translation

A significant challenge for the clinical translation of LED-based PAI for minimally invasive procedures is to overcome poor SNR arising from low pulse energies and long pulse durations. Poor SNR, which limits the imaging depth, has also been encountered with the use of laser diodes for PAI [120, 121, 122]. One solution, which was suggested by Allen and Beard [107, 123] and implemented by Dai *et al.*

[124], is to overdrive LEDs when they are driven at low duty cycles[121]. Another solution is to perform signal averaging, to which LEDs can be well suited due to their high repetition rate. However, this solution comes at the expense of decreasing the frame rate [105]. Allen and Beard [123] used signal averaging to demonstrate that LEDs can be used as an excitation source for imaging superficial vascular anatomy. Coded excitation sequences such as Golay code pairs [107] can also be used, as a type of averaging, to improve the SNR. In practice, motion can limit the lengths of these code pairs. In 2013, Allen and Beard [107] demonstrated that Golay code pairs could be used to simultaneously acquire signals from a tissue-mimicking phantom at multiple wavelengths.

A second challenge with the clinical translation of LED-based PAI is to manage the heat that LEDs produce, which can be transferred to the patient and can also result in shifts in the emission wavelengths of the LEDs [125]. These thermal considerations will be important when considering integration of LEDs directly into US imaging probes, as an evolution from bulky, side-mounted arrays [126].

Exogenous contrast agents could also improve the SNR and depth penetration achievable with LED-based PAI systems. To increase SNR of vessels, contrast agents such as gold or silver nanoparticles have been used to generate larger signals [127, 128, 129, 130, 131, 132]. However, adding contrast agents is usually sub-optimal or not possible for clinical translation, as agents used in pre-clinical studies are unapproved for human use and are known to be toxic. Injections of indocyanine green (ICG) are promising, as this contrast agent is approved for use in human patients and has optical absorption spectra that can be matched to LEDs. Singh *et al.* [126] used ICG as a contrast agent to show simultaneous imaging of both vascular and lymphatic structures in vivo. In combination with contrast agents such as ICG, LED-based PAI could potentially be used to increase contrast for nerves, with injections around the nerves during hydrodissection.

Tissue-mimicking phantoms will be important for training clinicians with PAI

systems. Anatomically accurate phantoms, with optical and acoustic properties similar to those of human tissue, can be challenging to develop. The work described earlier in this thesis to create wall-less vascular phantoms has potential to be highly useful for phantoms in this area as well.

5.1.5 Photoacoustic imaging phantoms

There has been significant work to standardise phantoms fabrication methods and materials for PAI [133, 134, 135]. Standardisation would be beneficial for the development of improved imaging systems, and allow them to be objectively characterised. Various different materials have been suggested and tested as PAI phantom materials; each has their own benefits and limitations and there is no one perfect solution. For other uses of PAI phantoms, such as for clinical training, the most suitable material and fabrication method depends on the intended application.

Polyvinyl chloride plastisol (PVCP) has been widely used as a PAI phantom, due to its favourable properties such as stability over time [135, 136]. The optical, acoustic, and mechanical properties of PVCP have been reported in the literature [135, 137]. Gel wax is another oil-based material that has been demonstrated as a suitable material for PAI [111]. The optical scattering and absorption properties of the materials can be controlled by adding scatterers such as titanium oxide [50]. Gelatin based phantoms [2] have also been investigated, but these have low mechanical stability and reduced longevity compared to other materials, such as PVCP.

Studies have also shown that PVA-c phantoms can be used successfully as PAI phantoms [49, 22, 138]. In the literature, PVCP is often preferred over PVA-c due to the limited lifespan of PVA-c, however this can be extended using antimicrobial agents and using appropriate storage. This means that although PVA-c phantoms may not be suitable for testing stability of novel PAI systems over very long periods of time, for applications in minimally invasive surgery such as for training phantoms,

the material is appropriate. The techniques used in this thesis are also relatively simple and low cost, so fabrication of multiple PVA-c phantoms in certain instances may be more cost-effective than more expensive materials such as PVCP. Finally, the potential that PVA-c has shown to be self-healing makes it especially interesting as a phantom for interventional imaging, or for PA guided percutaneous procedures.

5.2   Methods

The first step of applying the phantoms developed earlier to PAI was to test how the phantom capabilities vary with different fabrication conditions. Once these had been tested and the optimal conditions had been found, a nerve phantom similar to that in **Chapter 4** could be fabricated and used to simulate interventional procedures with PAI guidance.

5.2.1   Photoacoustic image acquisition

All PAI in this chapter was performed using an LED-based system (AcousticX, CYBERDYNE INC., Tsukuba, Japan), which uses LED arrays to deliver excitation light at a wavelength of 750nm. This system has the capacity to image with both ultrasound and PA, so the images can be overlayed and displayed together, in real time. Phantoms were imaged submerged in a water bath, to enable coupling between the transducer and the phantom surface. The presence of the LEDs results in the PAI probe being bulkier than a regular ultrasound transducer, as seen in **Fig. 5.1** and so the probe dimensions had to be considered when fabricating the phantoms, to make sure that the full capacity of the probe could be exploited.

Before imaging began, blood-mimicking fluid was flushed through the vessels for contrast, using plastic tubing at either end of the vessel openings. The blood mimicking fluid was made up of India Ink diluted to 0.5%, as described by Xia *et al.* [116], which has an intrinsic absorption coefficient of $324 \, \text{mm}^{-1}$ at 750 nm [133] and was found to be consistent with measurements of human blood [116, 134].

Figure 5.1: Imaging probe of LED-based photoacoustic imaging system, showing ultrasound transducer, with LED arrays either side

Image acquisition was then performed, based on the method described by Xia *et al.* [48], in collaboration with Dr Wenfeng Xia and Mengjie Shi from Kings College London. The system uses a linear array PZT ultrasound probe, with 128 elements across 38.4 mm. Each element in the array has a transverse length of 5mm, a pitch of 0.3 mm, a central frequency of 9 MHz, and a measured -6 dB bandwidth of 77%.

Radio frequency (RF) data was acquired from all ultrasound transducer elements, at a sampling rate of 40 MHz for PAI and 20 MHz for ultrasound imaging. This data was then transferred to a graphics processing unit (GPU) via a USB interface, and averaged across sequentially acquired PA images.

5.2.2 Photoacoustic image reconstruction

The images were reconstructed using an inbuilt GPU-based Fourier domain reconstruction algorithm and displayed in real time, whilst image thresholding was performed manually in real time, to increase image clarity.

Raw RF data were saved and made available for offline reconstruction; a maximum of 1536 PAI frames and 1536 US frames, corresponding to a total duration of 20s, could be saved in memory at one time. Averaging over n frames was implemented in order to suppress random noise in the background. Typically, the n was chosen as 24, 12. A fast fourier transform (FFT)-based algorithm was employed for the offline reconstruction and the speed of sound used was 1540 m/s, as is standard for human tissue.

5.2.3   Test phantoms

The initial tests were conducted using polyvinyl alcohol cryogel (PVA-c) phantoms, fabricated with varying freeze-thaw cycles and addition of varying amounts of backscatterers, to investigate the difference between them and the penetration depths achieved with PAI. Six different phantoms were fabricated; three that underwent one freeze-thaw cycle and three more that underwent two cycles. For each set of three, the first phantom had no added backscatterers, the second had 0.05% w/w glass microspheres added and the third had 0.5% w/w backscatterers.

Each of the six phantoms were fabricated so that they had five wall-less vessels at increasing depths, using the fabrication method from **Chapter 3**. All six phantoms had identical geometry, as demonstrated by the schematic in **Fig. 5.2**, so that it would be possible to compare between them. Blood-mimicking fluid for contrast was flushed simultaneously through all five vessels, directly before imaging. The phantoms were then washed out with water after imaging, to remove any residue contrast left in the vessels.

5.2.4   Nerve phantom and needle insertions

The results from the test phantoms were used to determine the depths of the anatomical structures used in the fabrication of a nerve phantom. A phantom was fabricated using the method described in **Chapter 3**, with a hyperechoic nerve
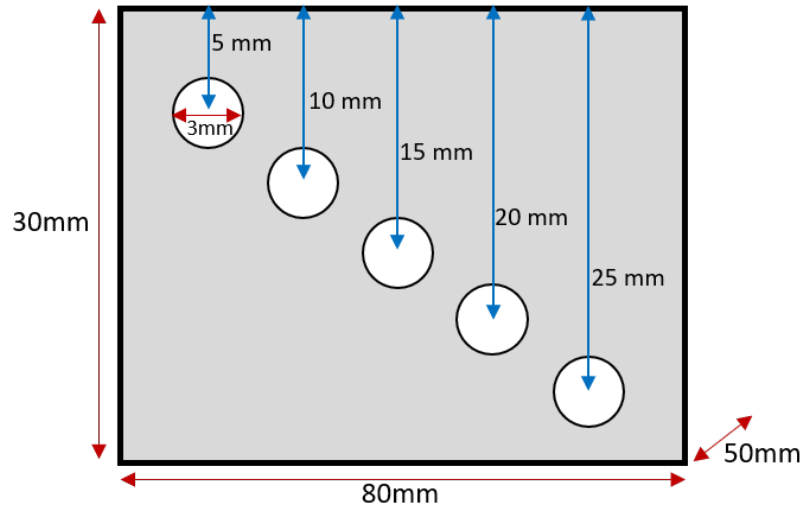
Figure 5.2: Schematic of photoacoustic imaging test phantoms, with wall-less vessels at increasing depths

structure, and two wall-less vessels, to simulate a vein and an artery, the geometry of which can be seen in **Section 5.3**. The vessels in this phantom were 3 mm in diameter, as this was most compatible with the tubing used to flush the blood-mimicking fluid through the vessels for PA contrast. After considering the results from the test phantoms, the nerve phantoms were fabricated using two freeze-thaw cycles, as this created a slightly stiffer phantom than one cycle, which provided more realistic resistance for needle insertions.
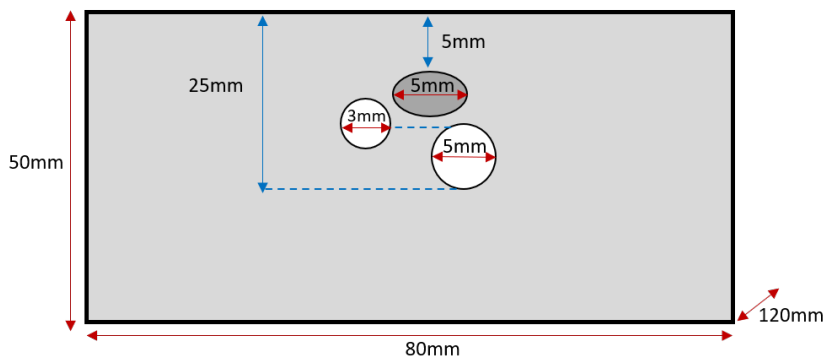
Figure 5.3: Schematic of nerve phantom for photoacoustic imaging, including wall-less vessels of 3 mm and 5 mm diameter, and a solid 5 mm diameter hyperechoic nerve structure (grey ellipse)

Multiple iterations of the nerve phantom were created and imaged with the AcousticX system. These phantoms had a smooth surface, which was the surface that was against the bottom of the plastic box that the phantom was cast in, and a rough surface, which had been open to the air during the fabrication process. Initially, a line artefact was seen in all the PA images (Fig. **5.4(a)**), which was thought to be caused by reflections from the smooth surface of the phantom. When the rough side was used for imaging instead, the artefact disappeared (Fig. **Fig. 5.4(b)**), so in subsequent iterations, the phantoms were constructed so that the imaging could be performed on the rough surface. In (**Fig. 5.4**), optical contrast was not injected into the vessels, and therefore, no generated PA signal was expected from the vessels. Once a suitable nerve phantom had been fabricated, nee-
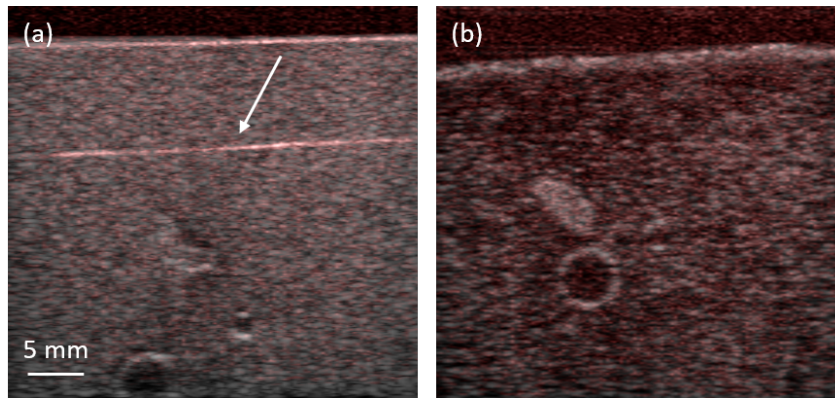
Figure 5.4: (a) Nerve phantom, as imaged with smooth surface face up, resulting in artefact (arrow) (b) nerve phantom imaged with rough side up, with no artefact observed. No optical contrast was injected into the vessels here

dle insertions were performed, to investigate the feasibility of using these phantoms for clinical training with PAI. The phantom was submerged in water, to ensure coupling between the phantom surface and the probe, and tubing was inserted into the vessel openings. India Ink was injected through the vessels for contrast; the setup can be seen in **Fig. 5.5(a)**. A 20 G needle was inserted into the phantom, but care was taken to ensure that the needle did not puncture the wall-less vessels, as this would allow the contrast to leak out.
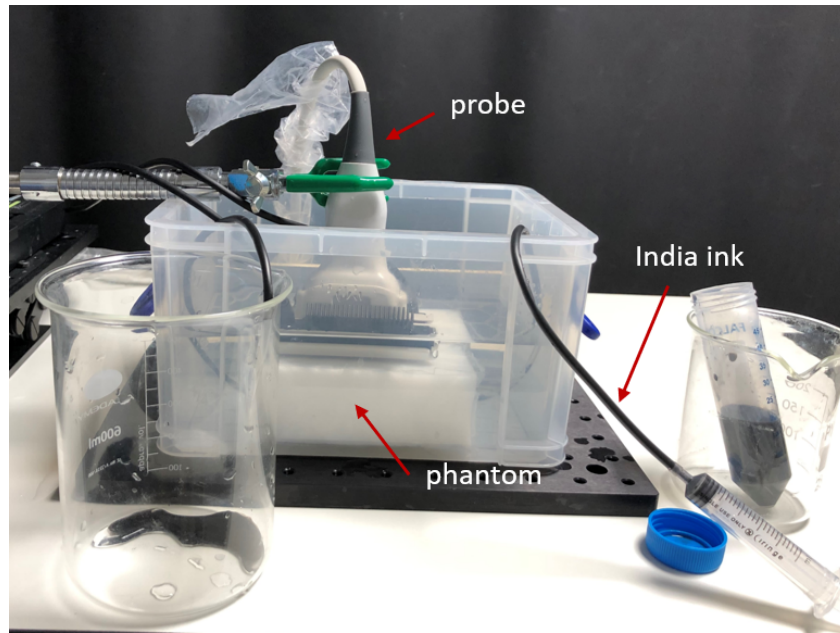
Figure 5.5: Photoacoustic imaging phantom setup, with phantom submerged in water tank, and imaging probe positioned above. Blood mimicking fluid (India ink) injected through the vessels for contrast via plastic tubing

5.3 Results

The best results were achieved when the phantom was created so that the imaging surface was rough, rather than smooth, to reduce the appearance of artefacts. The artefact was more dominant in PAI than ultrasound, and it was though to be caused by reflections on the smooth, shiny surface that was optically reflective. The rough surface likely absorbed more energy and less was reflected from this surface, and therefore there were less issues with artefacts.

Results from the test phantoms showed that PA signal could be achieved at depths up to around 20 mm within the TMM, regardless of whether backscatterers were added for ultrasound contrast. Qualitatively, the results did not differ significantly between phantoms fabricated with one freeze-thaw cycle (**5.6**) and those with two (**5.7**). However, phantoms with two freeze-thaw cycles were easier to handle, and they were more mechanically robust, which made it easier to attach the tubing.

Five vessels were included in the test phantom, at increasing depths. No signal from the deepest vessel, which was 25 mm below the surface, was apparent and so this vessel is not included in the images presented here. In the two most shallow vessels (5 mm and 10 mm) it was possible to get strong signal, with all backscatterer concentrations, and both one and two freeze-thaw cycles. It was possible to get signal from the next two vessels (15 mm and 20 mm), although only from the top of the 20 mm vessel, and the 15 mm vessel was not clearly visualised with PAI in the one freeze-thaw, no backscatterer test, as seen in **5.6(a)**.
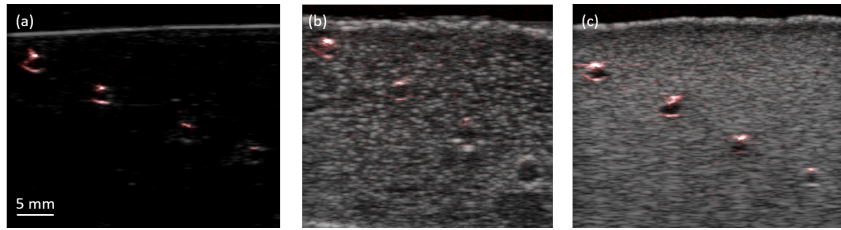
Figure 5.6: Ultrasound images, with photoacoustic overlay, of one freeze-thaw cycle test phantoms, (a) no backscatterers (b) 0.05% w/w backscatterers (c) 0.5% w/w backscatterers
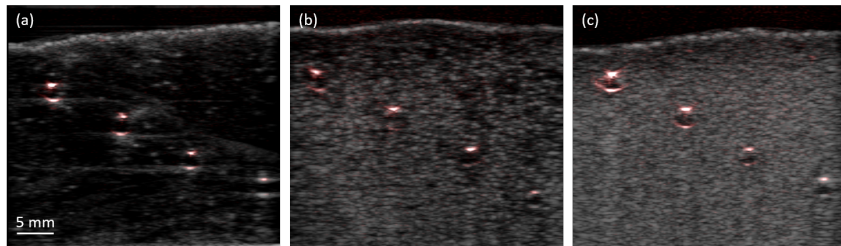
Figure 5.7: Ultrasound images, with photoacoustic overlay, of two freeze-thaw cycle test phantoms, (a) no backscatterers (b) 0.05% w/w backscatterers (c) 0.5% w/w backscatterers

Needle insertions were successfully performed on the nerve phantom. The needle was easily visualised with PAI, although it did create artefacts in the image, which can be seen in **Fig. 5.8(a)**. When the needle was removed, no visible tracks were left behind in the TMM and the background material appeared speckled and homogeneous, consistent with real tissue. As the vessels had PAI contrast, it was easy to identify them within the nerve phantom, and so they could be avoided during

the insertions. The signal obtained from the vessels was visually very similar to what would be expected in human vessels, so the phantom had satisfactory imaging properties.

Waterproof India Ink was used as the contrast agent in the vessels, and it was found that as long as the phantoms were washed out thoroughly with water after use (by flushing water from the tap through the wall-less vessels) then the ink did not stain the phantom, and it could be used repeatedly. In some early cases, however, the phantom was not washed thoroughly enough and ink was left on the surface of the phantom accidentally for a prolonged period of time. This then precluded the phantom from further use, as the ink bled into the surface of the phantom and could not be removed.
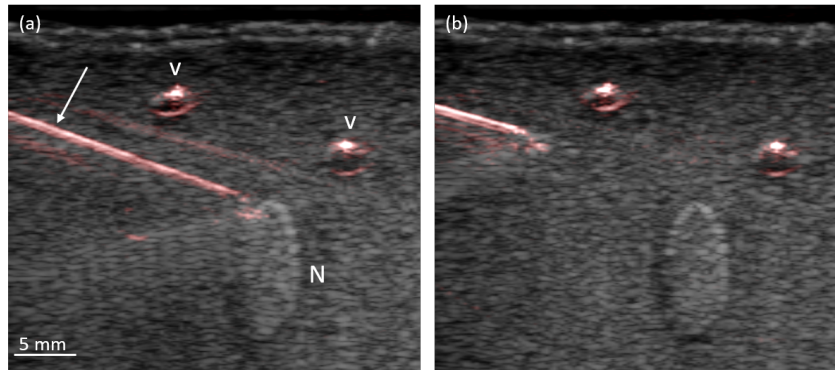
Figure 5.8: Needle insertions of nerve phantom, showing hyperechoic nerve (N), two vessels (V), and needle (white arrow) (a) needle insertion result in visible artefacts (b) needle removal left no visible tracks left in the material

5.4 Discussion

This chapter has described the role of PAI in minimally invasive surgery, and why LED-based imaging systems have a strong potential for this application, especially for peripheral targets. As photoacoustic excitation sources, LEDs have the advantage of being compact, so that they can potentially be tightly integrated with clinical US imaging probes. However, as explained here, they come with the signif-

icant challenge of overcoming low SNR that results from smaller pulse energies and longer pulse durations than many conventional photoacoustic excitation sources. Recent demonstrations highlighted, which use LED-based systems to visualise vasculature and minimally invasive devices, are promising indications of how PAI could be used in clinical practice.

The use of PVA-c phantoms for combined ultrasound and PAI was also presented. This is thought to be the first demonstration of the use of PVA-c phantoms to create nerve block phantoms, with both ultrasound and PA contrast, and the ability to perform needle insertions. The results showed that the materials used enabled a speckled, heterogeneous background to be created, with vessels that could be clearly visualised with ultrasound and PAI, up to depths of around 20 mm, which is comparable to the depths achievable in human tissue.

Needle insertions could be performed under ultrasound guidance in the PVA-c phantoms, and they did not leave any visible track marks, meaning that the phantom had suitable self-healing capabilities for it to be used as a clinical training phantom. In order to obtain PA contrast in the vessel structures, injected contrast (India Ink) was used. This means that the vessel structures cannot be punctured during needle insertions and is a limitation of possible applications. If the vessels were punctured, the injected contrast may leak out, rending the phantom useless for further PA imaging. However, in clinical practice, during nerve blocks, veins and arteries are generally targets to be avoided, rather than targeted or punctured, as it is dangerous to inject local anaesthetic (the agents used in nerve blocks) into the blood vessels. Therefore, as clinical training tools for nerve block procedures, these phantoms are still highly relevant. Other applications where vessels may be targets, such as in central venous catheterisation and vascular access, were not the focus of the phantoms created here, and these procedures are not likely to be used in conjunction with PAI, so are beyond the scope of this work.

The method used to inject the blood-mimicking fluid was not optimised and

meant that some of the imaging was not as thorough as originally planned. Unfortunately, due to lab access restrictions as a result of COVID, it was not possible to perform many planned iterations of the experiments, and there was limited time to improve the method. In future, a more sophisticated setup could be used, with the tubing fixed securely to the phantom vessels (either during the fabrication process, or afterwards using fitted adaptors). This would enable better and more consistent images to be acquired.

Another limitation of the phantoms described here is the depths at which is it possible to acquire PA contrast at. In the work described here, the depths were limited to around 20 mm. This is mostly a result of the limitations of the imaging system, and so this challenge would only be overcome with improvements in PAI technology. A possible solution to the limited imaging depth is to use interventional PAI, where excitation light is delivered through a needle. Future work could also explore this possibility, and based on the results achieved here, it is likely that the phantoms would also be compatible with interventional imaging. However, the interventional nature of the PAI might cause disruption for the clinical workflow and not be suitable for nerve block applications.

As a next step, the offline reconstruction data could be used to analyse the image intensity and SNR of the data acquired with the depth phantoms. It would also be interesting to explore the potential of the LED-based PAI systems to acquire different metrics such as oxygenation. Using multi-spectral imaging systems, it is possible to distinguish blood oxygenation levels [116, 139], and it could be possible to replicate this in a phantom, by varying the contrast injected into the artery and veins. In addition, in future the phantoms described here could be characterised both optically and acoustically, so that there is greater information available on the properties of the phantoms used here, with their specific additives and freeze-thaw cycles.

Multi-Modality, Patient-Specific, Polyvinyl alcohol Brain Phantoms for Applications in Neurosurgery

Table of Contents

This chapter describes the fabrication of a novel brain phantom, for applications in minimally invasive neurosurgery. The work was undertaken in collaboration with Dr Jonathan Shapey - a consultant neurosurgeon at King's College London. A first iteration of the phantom was published in the Journal of Visualized Experiments [140] and its use was also demonstrated in a further publication [141].

6.1   Introduction

Moving away from the vascular structures replicated in earlier chapters, there are also many other areas of minimally invasive surgery where phantoms are required. Brain phantoms have been especially challenging to fabricate, due to the complex anatomical structures, and wide variety of imaging modalities that are used clinically to diagnose brain pathologies. There was interest in developing a novel neuronavigation system, which would integrate intraoperative ultrasound and other intraoperative neuromonitoring. In order to test and validate such a system, a patient-specific phantom was needed, that would be compatible across all the imaging modalities used in skull based neurosurgeries. To simplify the problem, a vestibular schwannoma was chosen as the pathology to include in the phantom, but the method used could be extended to a variety of skull based pathologies.

6.1.1   Clinical background

Vestibular schwannoma is a type of benign (non-cancerous) brain tumour that arises from the vestibulocochlear nerve. This is the nerve that connects the brain and the inner ear. The condition is thought to have an incidence of 10.4 per million per year, and account for 8% of all intracranial tumours [142]. Although vestibular schwannoma is benign, it still poses a health risk as it can grow and restrict structures within the brain. There is also a small risk of the tumour turning malignant. The main symptoms reported as a result of vestibular schwannoma are progressive

hearing loss and tinnitus. In more severe cases where the tumour is larger, it can lead to hydrocephalus and brainstem compression.

There are risks associated with surgery, so patients are not operated on in all cases, and therefore improving the intraoperative procedure, and reducing the associated risks, using a neuronavigation system, would be beneficial in many skull based surgeries, including for vestibular schwannoma. The surgery for the removal of vestibular schwannoma involves creating a retrosigmoid craniotomy (a small hole in the skull behind the ear) through which to operate. This means that a skull also needs to be considered in the phantom fabrication process, in addition to the brain soft tissues, so that this surgery can be simulated with realistic conditions.

In the surgical treatment of vestibular schwannoma, pre-operative MRI and computed tomography (CT) imaging is used to assess the tumour, and plan surgery. During the surgical procedure, intraoperative ultrasound imaging is also used. In all three of these imaging modalities, the tumour tissue is distinguishable from the healthy brain tissue. Therefore, phantoms for use in this application should be compatible across all three imaging modalities.

6.1.2 Technical background

Previous studies have aimed to create brain phantoms, and different methods have been employed, depending on the level of complexity required and the specific application. The most common technique is to use 3D printing to create a negative mould of the brain, and then cast TMM in this mould. Ploch *et al.* used this method to create a gelatin based brain phantom, which they were then able to characterise the mechanical features of, however, no imaging techniques were demonstrated, so it is not clear how successful this phantom would be for multi-modality imaging [143]. Weinstock *et al.* also used 3D printed moulds to create a brain phantom from a patient with hydrocephalus [144]. Again, this phantom was shown to be useful as a physical training model, but no multi-modality imaging was demonstrated.

Grillo *et al.* created a brain phantom using styrene-ethylene/butylene-styrene (SEBS) gel, and were able to perform CT imaging with the phantom. They then compared the phantom CT scan to the patient MRI, to highlight the difference between the two anatomies. However, it would be more appropriate, if the phantom were to have MRI contrast, to compare directly between the phantom and patient MRI scans, rather than one CT and one MRI. In addition, the fabrication process of this phantom was very time consuming, and so the authors made scaled down models, to try and reduce the time required for fabrication. They found that below 50% of the original model size, there were issues with visualisation of surface details and identification of anatomical landmarks.

Chen *et al.* were able to use PVA-c to create a multi-modality imaging phantom of the left brain hemisphere, based on patient-specific data [56]. The authors used marker spheres and inflatable catheters to simulate tissue deformation, rather than a patient-specific pathology. The phantom was shown to be compatible with MRI, CT, and ultrasound - although the ultrasound images are not shown in the manuscript - which further demonstrates that PVA-c is a suitable material for the fabrication of brain phantoms. The authors made the images acquired in this work publicly available to the wider imaging processing community, which in itself is a valuable contribution to the field.

Overall, the requirements of the phantom, for the applications in this chapter were as follows:

1. It should be created using patient-specific data, so that it would be anatomically realistic

2. The whole brain should be included in the phantom, including both cerebral hemispheres and the cerebellum

3. A patient-specific vestibular schwannoma tumour should be included

4. The phantom should include the skull, with a craniotomy in the appropriate

region, so that the surgery could be simulated in a realistic way

5. The phantom should have multi-modality imaging capabilities, so that it would be compatible with all three imaging modalities - ultrasound, CT, and MRI - used in this type of minimally invasive neurosurgery

Based on these requirements, and the material properties discussed in **Chapter 2**, PVA-c was chosen as the TMM for this phantom. PVA-c is also a stable material that is durable enough to withstand manual manipulation, which is an important characteristic in this application. To perform intraoperative ultrasound in the minimally invasive surgery for removal of a vestibular schwannoma tumour, a burr hole ultrasound probe is used. The burr hole probe is small and thin, and pressure is applied by the clinician, to couple the probe to the brain tissue. This means that the TMM needs to also be able to withstand this pressure, so that the surgery can be simulated, and PVA-c was found to be suitable for this application, where many other soft tissue mimics such as gel wax or agar, were found to be too soft or friable to be suitable.

6.2   Methods

The methods here describe the novel technique developed for fabricating patient-specific, multi-modality brain phantoms, including a patient-specific tumour pathology. In the first instance, the phantom had compatibility with ultrasound and CT imaging, and the methods for creating this phantom are presented here, adapted from work published in the Journal of Visualized Experiments [140]. A protocol detailing step-by-step instructions for fabricating the brain phantom was included in the publication; a copy of this protocol can be found in **Appendix B** and the accompanying video be viewed **here**. Further work aimed to add MRI compatibility to the phantom, and the methods used for this work are also described.

6.2.1   Data

The phantom was created from patient-specific data, in order to make it as anatomically realistic as possible. In order to do this, anonymous, pre-operative CT and MRI scans were obtained, along with intraoperative ultrasound images, from a single patient with a vestibular schwannoma. For the CT images, volumetric scans were used, and for MRI, contrast-enhanced, T1 weighted scans were obtained. The data was acquired by Dr Shapey at the National Hospital for Neurology and Neurosurgery, from a patient with a left sided vestibular schwannoma. Slices from each of the scans can be seen in **Fig. 6.1** and the tumour is demarcated by an arrow on the CT and MRI scans, and a symbol on the ultrasound. The anonymised
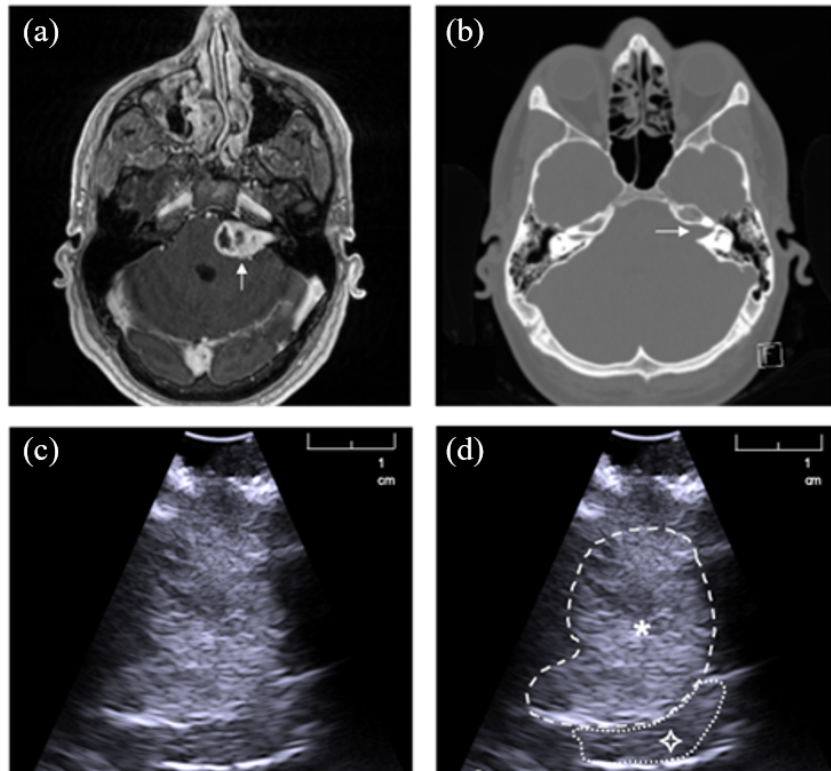
Figure 6.1: Patient data used to create phantom (a) MRI with arrow to highlight tumour (b) CT with arrow to highlight tumour (c) ultrasound (d) ultrasound marked up to highlight regions of interest ∗ cerebellar tissue and ◇ tumour
. Scale bar unavailable for patient CT and MRI scans

patient data used was originally gathered as part of a separate study, which was

conducted according to the principles expressed in the Declaration of Helsinki. It was approved by the NHS Health Research Authority and Research Ethics Committee (18/LO/0266) and informed consent was obtained from participants. All the imaging data was completely anonymised before analysis.

6.2.2   Segmentation

Segmentations of the data were completed by the neurosurgeon. This was achieved using 3D Slicer (http://slicer.org; version 4.10.2 used here) and an online brain extraction and parcellation tool from Nifty Web (http://niftyweb.cs.ucl.ac.uk). The subsequent editing of the structures, after segmentation, was completed independently of the neurosurgeon.

The skull, cerebrum, cerebellum, and tumour were the main structures of interested, so these were all segmented. The separate segmentations were then saved as .stl files, as this format is compatible with the computer aided design (CAD) software that would be used to create the phantom moulds, and also with the 3D printing software.

The segmentation of these large structures was a relatively simple process, and the resulting CAD models that were created can be seen in **Fig. 6.2**. The white asterisk in **Fig. 6.2(b)** shows the location of the left sided retrosigmoid craniotomy that was added manually during post processing. When looking at the CAD models, the tumour can be easily visually differentiated from the surrounding cerebellum tissue material; the black asterisk in **Fig. 6.2(e, f)** demarcates the location of the tumour.

6.2.3   Skull fabrication

The STL file of the segmented skull was imported into Meshmixer (Autodesk Inc., San Rafael, California, United States; http://www.meshmixer.com/; version 3.5.484 used here) for editing. A craniotomy was added to the left side of the skull, as seen
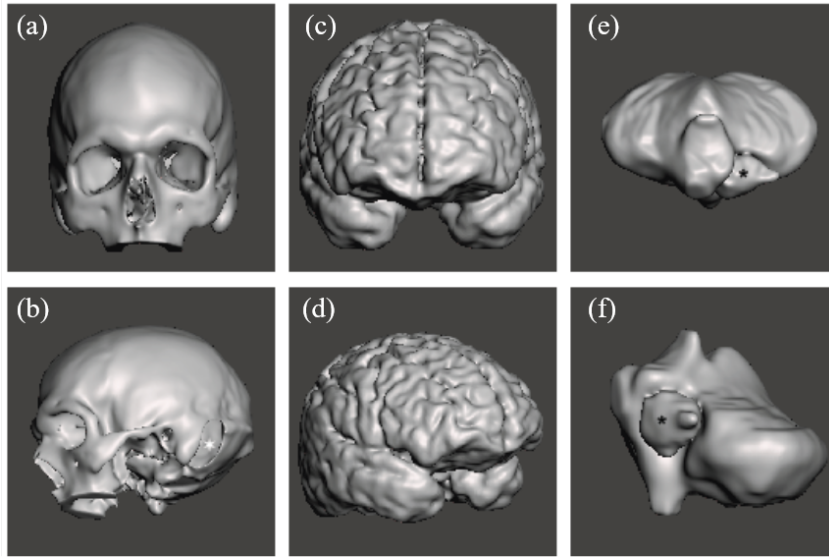
Figure 6.2: CAD models of the phantom constituents; (a, b) skull with ⋆ craniotomy (c, d) cerebral hemispheres (e, f) cerebellum with ∗ tumour

in **Fig. 6.2(b)**, and a split was created, so that the 'lid' of the skull could be removed, to allow the phantom soft tissues could be placed inside. To the plane of the split, small dowels were added to the skull model, so that the 'lid' could be secured back on to the main body of the skull.

Once the CAD file had been edited as described above, the skull was then ready for 3D printing. The main body of the skull, the 'lid' top piece, and the dowels were all printed separately. These files were imported into the 3D printing software (Cura, Ultimaker, Utrecht, Netherlands) and appropriate printing settings were chosen. As the density of the skull was not an important factor in the final phantom, 20% infill was used, to speed the printing process up as much as possible. The separate pieces were then printed on the commercially available Ultimaker S5 printer (Ultimaker, Utrecht, Netherlands), in white polylactic acid (PLA), which is a hard plastic commonly used in 3D printing. In total, the skull took around three days to print and this was the most time consuming stage of the phantom fabrication process.

6.2.4 Soft tissue mould fabrication

The cerebrum was also imported into the CAD software for editing. The whole structure was split into two cerebellar hemispheres, using the tools in Meshmixer. This step was necessary to allow the two hemispheres could be created independently, for ease of fabrication. From Meshmixer, these edited files could then be saved again as separate STL files, for compatibility with the other software used in the fabrication process. The tumour and cerebellum combined did not need to be edited, nor did the file containing the tumour alone. The cerebellum/tumour combined file was kept the same as the original segmentation, rather than splitting it into the cerebellum alone, so that the moulds could be fabricated appropriately.

The cerebellar hemispheres, cerebellum/tumour, and tumour STL files were then all separately imported into Fusion360 (Autodesk Inc., San Rafael, California, United States) for the mould creation. Using the tools in Fusion360, the segmentations were turned into a negative mould. These moulds were then split into pieces, again using the tools available in Fusion360, small dowels were added to the faces of each piece of the mould, and a hole was added to the top of each mould. This meant that the TMM could be poured into the moulds, and when it had set, the mould could be split into the separate pieces and the phantom structure could be removed without being damaged. Each piece of the mould for each soft tissue structure was then exported as an STL file again, which enabled it to be used with 3D printing software.

As with the skull, the moulds were printed on a commercially available printed (Ultimaker S5), using PLA as the printing material. Print settings were used to allow the moulds to be printed in the shortest time possible. The cerebellum/tumour mould was the most complex to create, and the resulting mould for this soft tissue can be seen in **Fig. 6.2**. In **Fig. 6.2(a)**the fully constructed mould is shown, and the hole that was manually added to enable the TMM to be introduced into the mould is marked. The separate pieces of the mould are numbered 1-4, and these

are shown in **Fig. 6.2(b-d)**
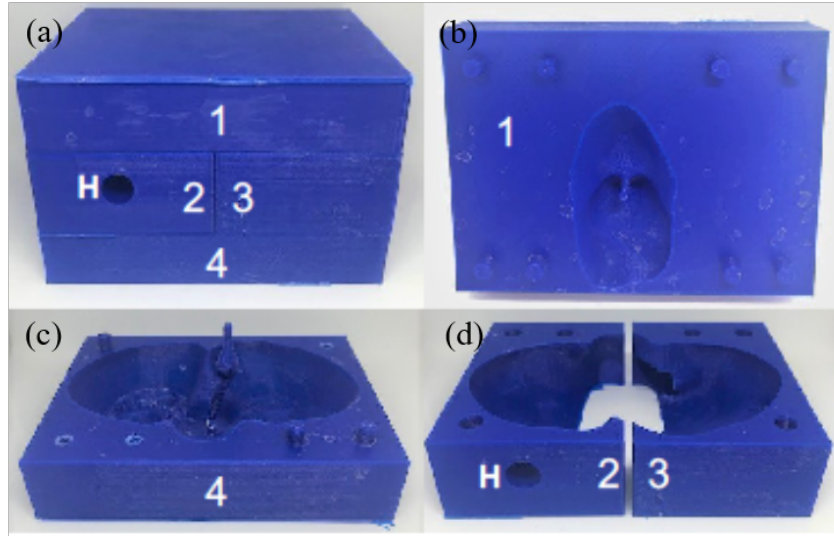
Figure 6.3: 3D printed PLA mould for cerebellum (a) complete mould, H denotes the hole to pour tissue mimicking material into (b-d) the separate pieces of the mould, numbered 1-4, which all slot together to make the mould shown in (a)

6.2.5 Contrast agents

Before the phantom could be created using the 3D printed moulds, the appropriate levels of contrast agents had to be determined. For the first iteration, the phantom had ultrasound and CT contrast. The contrast agents used for this are well characterised in the literature, as discussed in **Chapter 3**, and so this was not repeated here. Concentrations used for this phantom were based on those used by Chen *et al.* [56]. In the second iteration of the brain phantom, where MRI contrast was desired, in order to make the phantom fully compatible with the multi-modality imaging environment used in minimally invasive neurosurgery. There was less comprehensive literature available on the use of MRI contrast agents with PVA-c phantoms. Therefore, the first step in the process of creating a phantom that also had MRI imaging capabilities was to investigate the appropriate concentrations of contrast agent to use for both the healthy and tumour tissue.

Copper sulphate ($CuSO_4$) was chosen as the MRI contrast agent, as discussed

in **Section 3.2.7**. Although it is not well validated in the literature, $CuSO_4$ has been used successfully in previous phantom studies [56]. Therefore, a set of test phantoms were created to test various concentrations, and investigate the most appropriate level for the phantom and application in questions, and ensure that the addition of the other contrast agents (for CT and ultrasound imaging) did not affect the MRI imaging properties. The aim was to demonstrate that the MRI contrast agent could be used to span the physiological range of T1 and T2 values, and that adding the ultrasound and CT contrast agents did not affect this.

Samples of PVA-c (10% w/w) were produced, with varying amounts of $CuSO_4$ added to each sample. Half the samples had the ultrasound and CT contrast agents added as well. These samples were then imaged, and the results analysed to find the most appropriate concentration of contrast agent to use, to produce realistic results for both healthy brain tissue, and tumour tissue.

6.2.6 Concentration test samples

Moulds were 3D printed in PLA to enable 20 homogeneous cubes of PVA-c to be created, each containing varying amounts of contrast agents. These cubes were split into two groups of 10, referred to as 'Test A' and 'Test B'. In Test A, $CuSO_4$ of varying concentrations was added to the PVA-c samples. The concentrations chosen were (all calculated as w/w): 0, 0.01%, 0.02%, 0.025%, 0.03%, 0.05%, 0.1%, 0.15%, 0.2%, 0.25%. The range of values chosen was based on the concentrations used in previous studies [56].

The same concentrations of $CuSO_4$ were added to the samples in Test B. The Test B samples also had glass spheres (1% w/w) and barium sulphate ($BaSO_4$) (5% w/w) added, for ultrasound and CT contrast. The concentration of these additives was kept constant over all the samples so that it would be possible to compare between Test A and Test B, to investigate whether the addition of the other contrast agents affected the MRI contrast. The concentrations chosen for

the glass spheres and the $BaSO_4$ were the values used in the tumour, as this was the part of the phantom that used the highest concentration of contrast agents. Potassium sorbate (0.5% w/w) was also added to all samples, as a preservative. A schematic to show the test plates, including the concentrations used, is presented in **Fig. 6.4**, and a photo of the samples can be seen in **6.5**
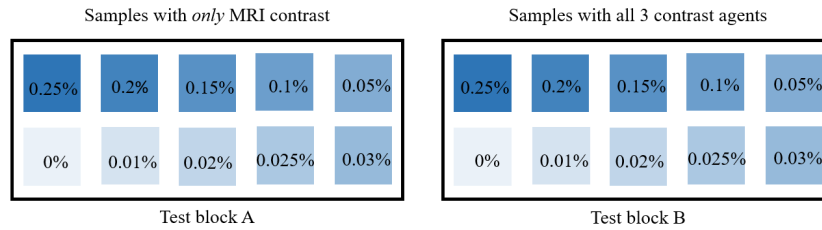
Figure 6.4: Schematic of samples used to test MRI contrast agent: Test A and Test B have identical copper sulphate concentrations in each sample; Test B also has glass spheres and barium sulphate to test the effect of ultrasound and computed tomography contrast agents

Figure 6.5: Photo of MRI contrast test samples; black plate shows Test A with just MRI contrast agent (copper sulphate) added and blue plate shows Test B with all contrast agents added (copper sulphate, glass spheres, barium sulphate)

MRI images of the test phantoms were acquired by Professor David Atkinson, from UCL, using a Philips Ingenia 3T scanner and head coil; more details of imaging

are provided in **Section 6.2.10**. The T2 and T2∗ results were fitted to the 32-echo scan automatically by the scanner, and these could then be plotted against concentration using MATLAB. The T1 results had to be fitted manually before plotting, and this was done with the help of code provided by Professor Atkinson, in MATLAB. This code included a GUI that was used to import the required data into MATLAB. The code also fitted the data so that the T1 relaxation times were displayed, using a colour map, for each sample. This output of Professor Atkinson's code was then used to plot the T1 relaxation time against concentration, also in MATLAB. ROIs were drawn in each sample, and the mean relaxation time within that region was calculated, and plotted against the corresponding concentration of that sample.

During the minimally invasive neurosurgery in which the phantoms are designed for, T1 imaging is used, so the T1 values were the focus of the analysis. However, it was also interesting to see that the T2 relaxation times were within the range of physiological values.

6.2.7 Preparation of tissue mimicking material

The TMM used for the fabrication of the soft tissues was PVA-c. The base material was prepared using the same method as that outlined in **Chapter 3**. Potassium sorbate (0.5% w/w) was added to the aqueous material as an antimicrobial agent to preserve the phantom. Contrast agents were added separately to the PVA-c for the tumour and the healthy tissue, so the two different tissue types would have the appropriate levels of contrast for imaging. Once the appropriate contrast agents were added to the aqueous PVA-c, the mixture was sonicated for 5 mins, to ensure homogeneous mixing of these additives, and left to rest for 10 mins at room temperature, so that any bubbles produced in the sonicating process could escape. Bubbles remaining on the surface of the mixture at the end of this time were carefully scraped off.

In the first phantom iteration, where only ultrasound and CT contrast was included, 1% w/w glass spheres were added to the tumour material for ultrasound contrast and 5% w/w barium sulphate ($BaSO_4$) was added for CT contrast. To the PVA-c that was to be used for the healthy tissues (cerebral hemispheres and cerebellum), glass spheres were added for ultrasound contrast, at a concentration of 0.05% w/w. No $BaSO_4$ was added to the healthy tissue, as the natural properties of PVA-c allow it to be visualised with CT imaging without any extra additives. Without the addition of $BaSO_4$ to the 'healthy' tissues, there was a strong contrast between the healthy tissue and tumour, as is seen in the real patient CT images.

In the second phantom iteration, where MRI contrast was also required, the same concentrations of ultrasound and CT contrast agents were used for healthy tissue as were used in the first iteration. As a result of feedback from clinicians, a lower concentration of $BaSO_4$ (2.5% w/w) was used for the tumour, so that the tumour area would appear less bright with CT imaging. In this second iteration, $CuSO_4$ was also added for MRI contrast, based on the T1 results from the test samples; T1 contrast was chosen as this was the most clinically relevant and at this stage, adding T1 and T2 contrast simultaneously would be challenging.

6.2.8   Addition of MRI contrast

To calculate the required $CuSO_4$ concentration for each part of the phantom, (hemispheres, cerebellum, tumour) the first step was to find the T1 relaxation times in the literature for those tissues, in the human brain, at 3T. Only literature using 3T was considered, as all the imaging for this work was done using a 3T scanner, and the patient data was also acquired with a 3T scanner.

Wansapura *et al.* [145] found the T1 relaxation to be 832 ± 10 ms for white matter and 1331 ± 13 ms for grey matter. These values are widely cited in the literature, and broadly agree with the average values found across other works, so the white matter value (832 ms) was used for the brain hemispheres. For the

cerebellum, it was challenging to find literature values at 3T, but cerebellar white matter was found to have a T1 relaxation time of 1081 ± 182 ms by Lee *et al.* [146], so this was value was used. Finally, for the schwannoma, values for human tissue at 3T were not found in the literature; in this second iteration, 1200 ms was chosen for the tumour but this proved to be inconsistent with human tissues, as explained further in the discussion

The corresponding concentrations for these T1 relaxation times were then interpolated from the test sample results. For the brain hemispheres, 0.01% $CuSO_4$ was added to the aqueous PVA-c at the same time as the other contrast agents; 0.02% $CuSO_4$ was used for the cerebellum and no (0%) $CuSO_4$ was added for the tumour. These values did not yield successful results, as explained in the discussion, and there is further work in progress on this.

6.2.9   Phantom assembly

The phantom assembly process was the same for both iterations of the brain phantoms. The only difference in the two phantoms was during the addition of contrast agents in the previous section and therefore, the assembly process applies to both phantoms.

The tumour was created first, and when this piece was finished, it was added into the slot within the tumour/cerebellum mould, and the PVA-c poured into the tumour/cerebellum mould then surrounded the solid tumour, so that eventually, this all became one solid structure. Therefore, the first step of phantom assembly was to use the 3D printed tumour mould to create the tumour, using the PVA-c mix that had glass spheres and $BaSO_4$. The tumour underwent two 6 hour freeze-thaw cycles (freezing at -20°C and thawing at room temperature, around 20°C). This structure was then placed inside the corresponding slot in the cerebellum/tumour mould, and the PVA-c mixture that contained only glass spheres was poured into the mould, over the solid tumour. This whole structure then underwent two of the

same freeze-thaw cycles.

The brain hemispheres were created in the same way, by pouring the PVA-c mixture into the two separate moulds, and being subject to two freeze-thaw cycles. Once the hemispheres and cerebellum had thawed for the second time, they were placed into the 3D printed skull. The cerebellum was secured in place in the skull with a small length of wire, so that it wouldn't rotate or slip around inside the skull. The brain hemispheres were placed on top of the cerebellum and the tight fit of the skull kept them secured in place.

6.2.10   Imaging

Ultrasound imaging was performed in simulation of intraoperative ultrasound during vestibular schwannoma surgery. A BK5000 scanner was used (BK Medical, Luton, UK) with a burr hole probe. Ultrasound gel was used for coupling the probe to the tissue surface, as this was deemed simpler than submerging the phantom in water.

CT images were acquired using an O-arm scanner (Medtronic, Dublin, Ireland), which is a mobile X-ray intraoperative 2D/3D imaging system. For CT scanning, the phantom was placed on the patient bed and orientated in the same way the patients' skull would be during imaging

MRI images of the two test blocks were acquired with a Philips Ingenia 3.0T MR system, (Phillips Healthcare Amsterdam, Netherlands); the protocol used to acquire T1 images can be found in **Appendix C**. The samples, enclosed in the 3D printed moulds, were put into the scanner simultaneously and placed inside a head coil on the patient bed.

MRI images of the full brain phantom were acquired with a separate 3T scanner (MAGNETOM Prisma scanner, Siemens, Munich, Germany). The protocol used for the MRI acquisition with this scanner can be found in **Appendix A**. This is the same machine and protocol as was used in **Chapter 3**. The scanner used to

acquire the brain phantom images was the same machine as that used to acquire the original patient data, and so had an identical protocol, for ease of comparison between the human and phantom data. This machine could not be used to acquire the test sample data, due to COVID restrictions at the time.

6.3 Results

6.3.1 Concentration test samples

The T2 values were calculated by the scanner, for regions of interest, as shown in **Fig. 6.6**. For this application, the T1 imaging properties were the focus and so the T2 results were not analysed it great detail. However, they serve as a proof of concept that the T2 properties can also be tuned for PVA-c phantoms, and this could be investigated further in future, if the T2 imaging properties were of interest. The T2 relaxation times of the concentration test phantoms generally followed the
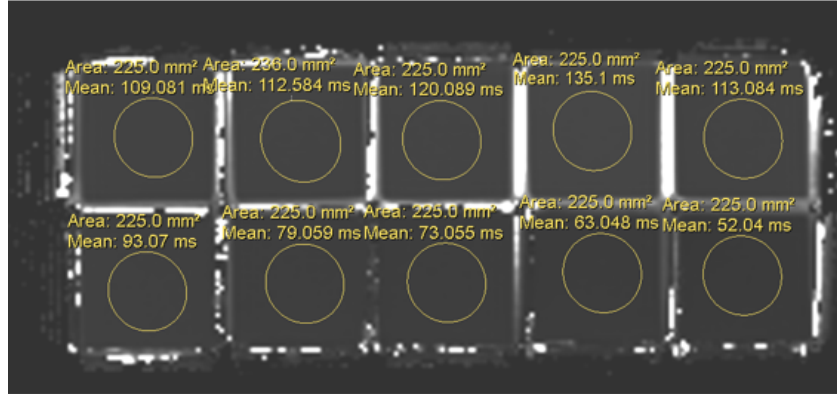
Figure 6.6: T2 values for regions of interest, as calculated by the scanner for Test A: PVA-c samples with copper sulphate added for MRI contrast

pattern that was expected, based on the samples used, (**Fig. 6.7**). The samples containing higher concentrations of $CuSO_4$ had faster T2 relaxation times, and there did not appear to be significant difference in relaxation time between the samples with only $CuSO_4$, and the samples that contained all the contrast agents. There are some values, plotted in **Fig. 6.7** that appear to be outlier values - namely

the Test A results for 0% $CuSO_4$ and the Test A result for 0.15% $CuSO_4$.This could be a result of the sample being contaminated with some $CuSO_4$ during the fabrication process; the 0.15% sample could also be due to incomplete mixing of the contrast agent within the aqueous solution of PVA-c during the fabrication process. The T1 properties followed a similar pattern to the T2 results, and overall showed
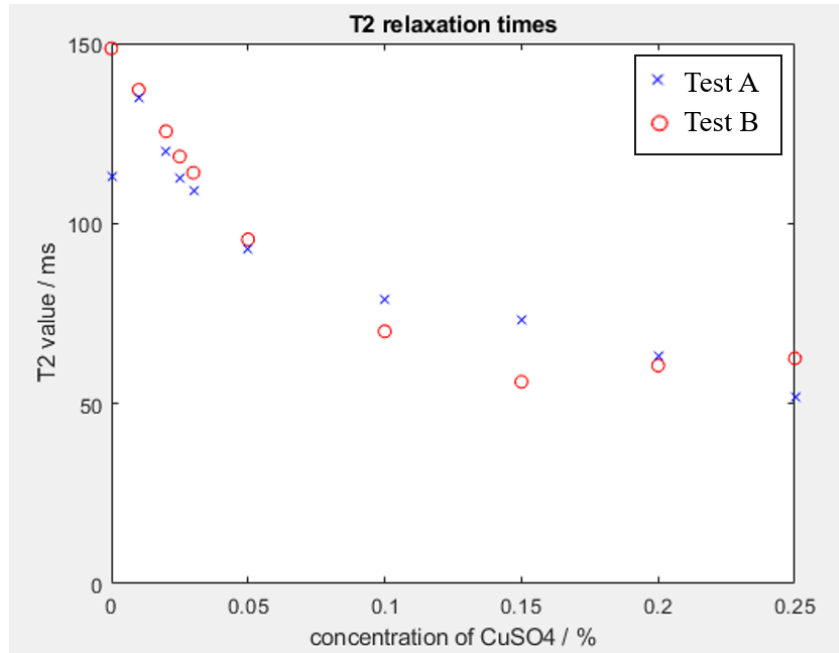
Figure 6.7: T2 relaxation times for samples in Test A (MRI contrast only) and Test B (all contrast agents), based on the values calculated by the scanner, for the ROIs shown in **Fig. 6.7**

that the results were comparable between Test A and Test B, and followed the expected pattern of decreasing T1 relaxation time, with increasing concentration of $CuSO_4$. This can be seen visually in **Fig. 6.8**, where the image shows that the two test plates appear to have very similar results, despite Test B having glass spheres and $BaSO_4$ added, in addition to the $CuSO_4$ contrast. The T1 results were fitted manually, as described in **Section 6.2**, and T1 relaxation times for each sample were then plotted against concentration. These results were promising, and showed that the T1 relaxation times were very similar for Test A and Test B. This is highlighted by the results in **Fig. 6.9**, where the blue crosses showing the results
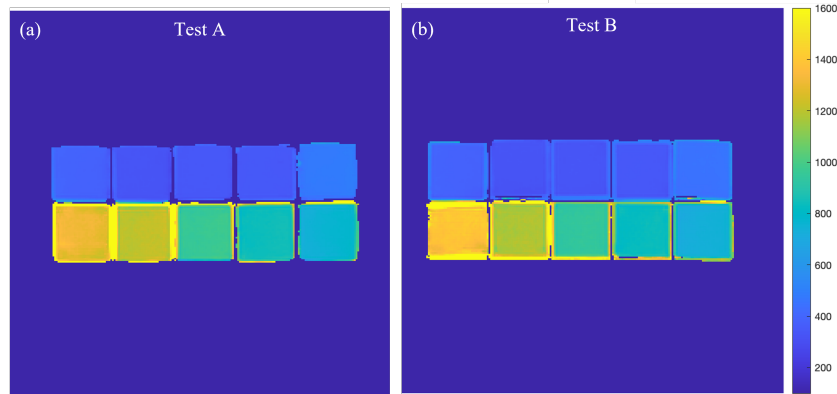
Figure 6.8: T1 images of samples (a) Test A (MRI contrast only) (b) Test B (all three contrast agents) show that the results are visually comparable for both tests, so the extra contrast agents in Test B did not affect the T1 properties of the samples

from Test A ($CuSO_4$ only) overlap closely with the results from Test B (all contrast agents), which are noted by the red circles. The results demonstrate that with the contrast agents employed, it is possible to create PVA-c phantoms that span the physiological range of T1 relaxation times. For this application, the specific window of interest was 600 - 1200 ms, as this is approximately the range of values for human brain tissue at 3T [145, 147, 148], and this region of interest is highlighted by the green dashed line in **Fig. 6.9**.

This specific region of interest is examined in more detail (**Fig. 6.10**), and even on closer inspection here, the two plates have very similar results. There is, however, a consistently higher T1 relaxation time for Test A than Test B at the same concentration, implying that the extra contrast agents did slightly decrease the relaxation time of a given sample, in addition to the decrease from the baseline that was achieved with CuSO4 alone. The difference is slightly more pronounced with the lowest concentrations concentrations (the greatest difference between Test A and Test B was 50.3 ms for 0.01% $CuSO_4$), and in future work it would be interesting to investigate this difference further, and compare the results from plain PVA-c to PVA-c with added $BaSO_4$ and glass spheres, to see what the effect on MRI signal is from these contrast agents alone. The results from **Fig. 6.9** were used
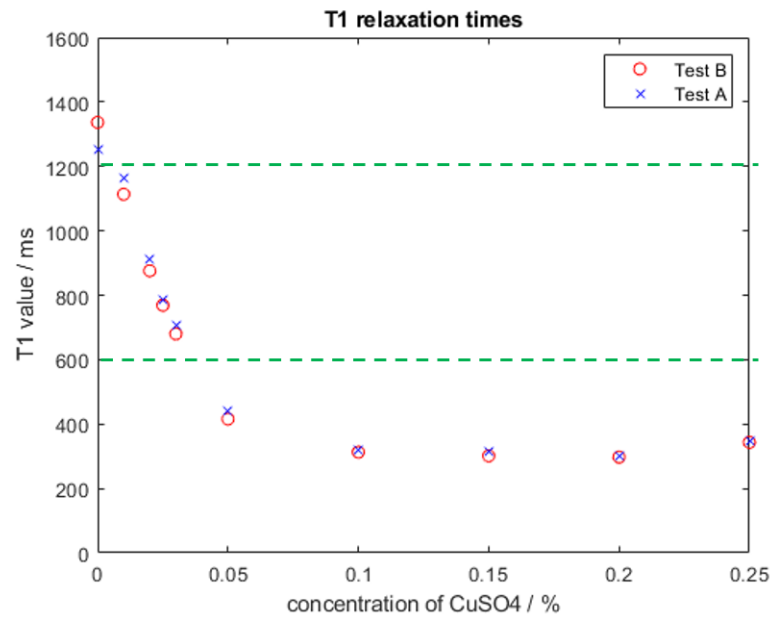
Figure 6.9: T1 relaxation times for samples in Test A (MRI contrast only) and Test B (all contrast agents), green dashed line highlights region of interest for human brain tissue
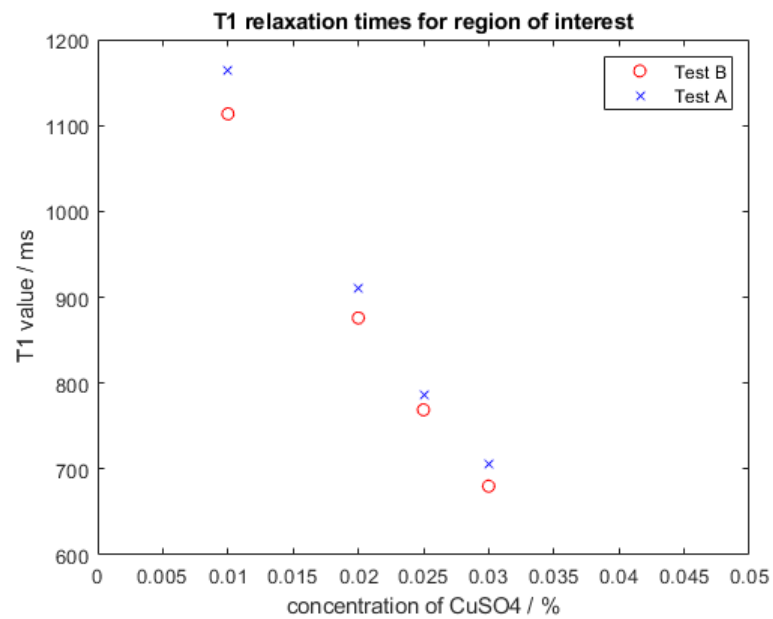
Figure 6.10: T1 relaxation times for region spanning human brain tissue, highlighted by green dashed lines in **Fig. 6.9**

to calculate the concentration of CuSO4 to be used in the phantom. Interpolation between the data points found that for 1080 ms, the corresponding concentration of CuSO4 to be added was 0.0147%, and for 832 ms, the concentration should be 0.022%. These were rounded up 0.01% and 0.02% due to limitations in the equipment available for measuring the contrast agents. For the tumour, as 1200 ms was thought to be the required associated T1 relaxation time for the tumour, no $CuSO_4$ was added.

6.3.2 Ultrasound and CT compatible phantom

Using the technique described, an anatomically realistic phantom was fabricated, consisting of a patient-specific skull, brain, and tumour. The completed phantom can be seen in **Fig. 6.11**. The two brain hemispheres (one is seen in **Fig. 6.11(b)**) were produced separately and have a realistic appearance, featuring the gyri and sulci of the brain. The whole phantom is an opaque white colour, which is the natural colour of PVA-c, but this could easily be changed if required, by adding dyes to the aqueous solution of PVA-c during the fabrication process. This was not deemed necessary for this project however, and was omitted to increase ease of fabrication. The cerebellum, seen in **Fig. 6.11(c)** fit comfortably into the base of the 3D printed skull -**Fig. 6.11(a)** - and the tumour is clearly visible due to its off-white colour that separates it from the surrounding cerebellar tissue, and arises from the $BaSO_4$. The tumour is securely attached to the cerebellum tissue, and can be manipulated in a way similar to real tissue. The phantom was imaged using both CT and ultrasound. $BaSO_4$ was added to the tumour for CT contrast and imaging of the phantom - **Fig. 6.12** - shows that this contrast was achieved and the tumour is clearly visible from the surrounding cerebellar tissue. On visual inspection, the clinician expressed that the tumour appears slightly too bright with CT imaging, and for a more realistic appearance, less CT contrast could be used in future iterations. The skull was printed with a low percentage infill (20%) in
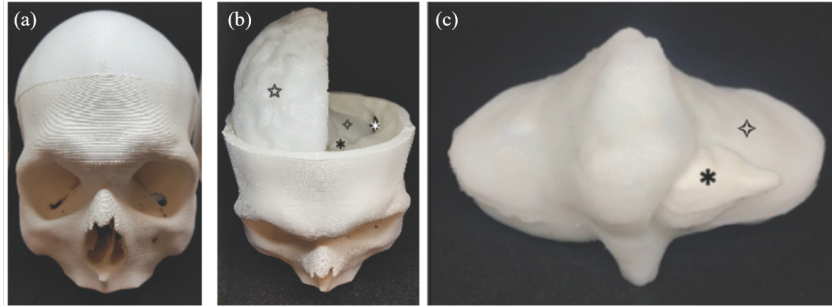
Figure 6.11: The finished phantom; (a) skull (b) phantom with skull top removed showing ★brain hemisphere, ◇cerebellum, ∗tumour, ⋆retrosigmoid craniotomy (c) ◇cerebellum and ∗tumour

order to reduce the time required for printing. Therefore, on the CT images, there is a lattice structure seen in the phantom skull, rather than the solid bone seen in real patients. This is not a limitation of the technique, because only the outline of the skull is needed for minimally invasive neurosurgery; the skull is mainly used for image registration and the printed phantom is sufficient for that purpose. The skull could be printed with 100% infill to avoid the reduced realism in the phantom image, but this would significantly increase the time of the phantom fabrication process.

Glass microspheres were added to the phantom for ultrasound contrast, and the results show that this was successful, and the tumour can be distinguished from the surrounding tissue with ultrasound imaging. To the untrained eye, it can be challenging to differentiate between the healthy and tumour tissue, so the results in **Fig. 6.12(b)** have been outlined to highlight the tumour. On visual inspection, as seen in **Fig. 6.12(c, d)**, comparison between the ultrasound images obtained from the phantom and the patient shows that the contrast agents used in the phantom were effective for creating realistic imaging properties. The CT images from the patient and phantom can also been compared - **Fig. 6.12(a, b)** - and this also shows that the phantom was an appropriate mimic, with similar anatomy to the patient. The phantom image is **Fig. 6.12(a)** is not from the same slice as the patient image in **Fig. 6.12(b)** and it is, therefore, not possible to directly compare
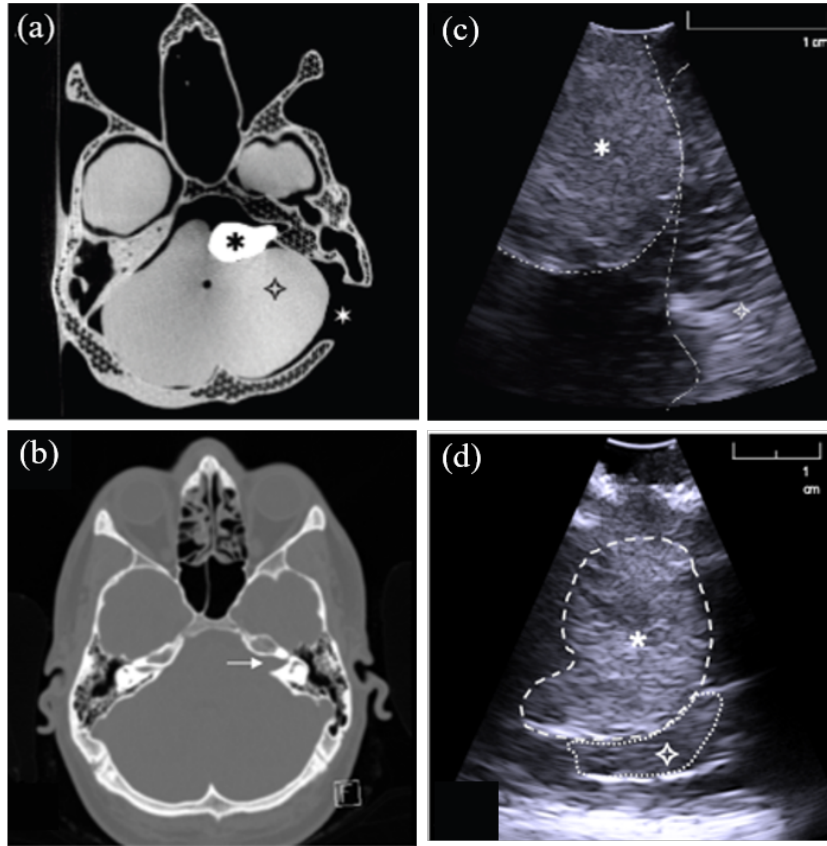
Figure 6.12: CT and ultrasound imaging of phantom scans (top row), as compared with patient scans (bottom row) with ∗tumour, ⋄cerebellum and ⋆craniotomy highlighted: (a) axial CT scan of phantom, through the level of the skull base and tumour (b) patient CT (c) intraoperative ultrasound of phantom, acquired with burr hole ultrasound probe, through the retrosigmoid craniotomy in plane approximately perpendicular to skull (d) patient ultrasound. Scale bar unavailable for patient CT and MRI scans

the tumour in these images. Overall, the tumour was deemed to have suitable anatomy and imaging properties.

The phantom was tested during a surgical simulation in a virtual operating room; a photo of this setup can be seen in **Fig. 6.12**. A skull clamp was used to position the phantom on the operating table, and the CT scan was registered using a clinical neuronavigation system; the registered scan can be seen displayed on the neuronavigation system in **Fig. 6.12**. As previously mentioned, for the surgical removal of a vestibular schwannoma tumour, a retrosigmoid approach is used, and

this was replicated in the phantom simulation. During the simulation process, the phantom model proved to be stable and no damage was observed from the necessary manipulation, and the phantom could be manipulated in the same way a human brain would be in a clinical scenario. As the phantom showed no signs of damage, it could be used repeatedly under the same conditions.

Figure 6.13: Surgical simulation with the phantom ♦ ultrasound system with burr hole transducer, ✠ neuronavigation system. Note: model pictured is one based on a patient with a right sided tumour

6.3.3 MRI compatible phantom

Unfortunately, the phantom did not have the appropriate level of T1 contrast with MRI imaging to produce realistic images (**Fig. 6.14**). The two brain hemispheres had the same amount of contrast added in the fabrication process, but appeared to have non-identical contrast with MRI imaging. This was likely due to incomplete mixing of the aqueous PVA-c with the contrast agents, as the addition of $CuSO_4$ increased the viscosity of the PVA-c and made it difficult to effectively mix, even with sonication. The tumour also did not have the desired level of contrast, and

ideally would have been brighter than the surrounding material on the MRI images. The values chosen were based on estimations from regular tumour tissue, however, in clinical practice, contrast is administered to the patient so that the tumour is contrast enhanced for imaging. In future work, this should be considered and the phantom should be created based on a contrast enhanced tumour.
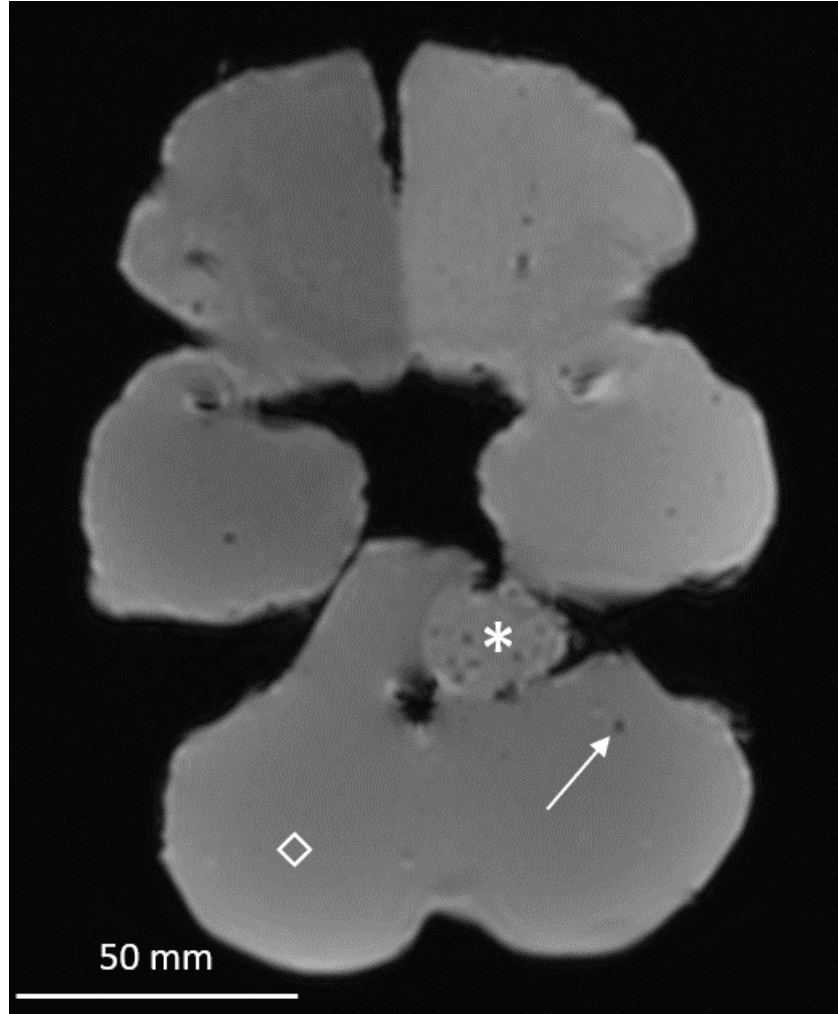
Figure 6.14: MRI imaging of brain phantom, highlighting *tumour and ◇cerebellum. The two brain hemispheres with different intensity can be seen, and multiple bubbles can be observed within the material (arrow)

Using ITK-SNAP (http://www.itksnap.org/) [149] the image intensity of different regions of the phantom were compared to a patient scan, and the results are outlined in **Table 6.1**. For the patient scan, the two hemispheres were assumed to

be equivalent. Although image intensity is not the same as T1, it can be used as a correlate and in this case, it was clear that the phantom did not quite match that of the patient data. In the patient scan, the tumour had a higher image intensity than the healthy tissues, and the cerebellum and brain hemispheres had a very similar image intensity. In order to adjust the phantom to better reflect the properties of a patient image, the tumour should have a higher image intensity, and this is achieved by shortening the T1 relaxation time for that tissue. The cerebellum and hemispheres should have the same concentration of MRI contrast added, so that they have equivalent image intensity, as is seen in the patient data. This should also be adjusted in the phantom and a lower image intensity should be created, by choosing a concentration that gives the tissue a longer T1 relaxation time.

Table 6.1: Comparison of average image intensities of brain and phantom tissue

Tissue	Patient data	Phantom data
Tumour	577	364
Cerebellum	247	394
Left hemisphere	225	456
Right hemisphere	225	342

6.4   Discussion

This section describes the fabrication of a patient-specific phantom that includes the brain, skull, and vestibular schwannoma tumour. The overall goal was to create a phantom compatible with multi-modality imaging, including CT, ultrasound, and MRI. In order to achieve this goal, a first iteration was created that included CT and ultrasound contrast. The second iteration, to include MRI is still a work in progress, but with further work, the phantom will be fully compatible with all three clinically relevant imaging modalities.

The novel brain phantom described here had the required level of anatomical detail for applications in minimally invasive neurosurgery, and was shown to be

useful for the development of new neuronavigational technology. The use of 3D printing techniques enabled anatomically realistic details to be achieved, and the phantom was mechanically stable enough to be manipulated in a way to simulate surgery. The first iteration of the phantom was published in JoVE [140], and the use of this phantom for validating a novel neuronavigation software was published in IJCARS [141].

The material used to create the brain phantom was PVA-c, which is well established as a suitable TMM and was shown here to be appropriate for applications in minimally invasive surgery. One of the benefits of PVA-c is that the acoustic and mechanical properties of the material can be tuned by varying the freeze-cycles. Two freeze-thaw cycles were used in the fabrication of the brain phantom, and this resulted in the material having sufficient durability to withstand manipulation and contact from the ultrasound probe during the simulation of vestibular schwannoma surgery. Provided that the tumour was not excised during the surgical simulation, the phantom could be used repeatedly, over a period of months.

PVA-c was also a suitable material as it is readily available, simple to use, and non-toxic. This means that it can safely be used as a clinical training tool in a hospital environment. However, the necessary addition of $CuSO_4$ for MRI contrast in the second phantom iteration results in this non-toxic property being lost, as $CuSO_4$ is moderately toxic when ingested, and can cause eye irritation. The concentrations of $CuSO_4$ in the phantom were very low, so as long as it is handled with care, it should not pose a great health and safety risk. Unfortunately, the addition of the toxic $CuSO_4$ is necessary to get appropriate MRI contrast. In future, if suitable, non-toxic contrast agents were found that could give the same level of MRI contrast to the phantom, then these could be used instead.

One limitation of the use of the phantom presented as a clinical training tool is that in a surgical setting, for intraoperative ultrasound imaging, saline is used for coupling, rather than a gel. This was not replicated in the phantoms demonstrated

here, as in order to flush saline around the phantom, the skull would need to be watertight. This is challenging to achieve, because without the surrounding skin, the skull naturally has holes such as the eye sockets, so further work would be required to overcome this. For example, the skull CAD model could be manually edited to close the holes before it is printed, although this would likely increase the print time of the structure. The use of gel in this instance did not significantly affect the clinical workflow or affect the quality of the acquired images, so was deemed acceptable.

It was challenging to obtain appropriate MRI contrast for the various different tissue constituents of the phantom. The MRI results showed that it is possible to use $CUSO_4$ to get varying MRI contrast within the phantom, and the phantom is fully MRI compatible. Further work is needed, however, to obtain the correct concentrations of the contrast agent so that the phantom mimics the patient images. In order to do this, the tumour within the phantom should be created to have a 'contrast enhanced' appearance, by adding contrast to the PVA-c, so that it has a much shorter T1 relaxation time than that achieved in the results shown here. A more detailed study of the addition of $CuSO_4$ to PVA-c as an MRI contrast agent, and the interaction and effects of other contrast agents, such as those used for ultrasound a CT image contrast would also be highly interesting and improve on the work presented here. Care should also be taken in future to ensure the contrast agents are fully mixed within the aqueous solution of PVA-c, to avoid inhomogeneities, as was seen in the results here, where the left and right phantom hemispheres did not have the same image intensity.

In future, the phantom could also be improved by adding in differentiation between internal brain structures. This would increase the anatomical complexity of the phantom and make it more realistic, but would not significantly increase the utility of the phantom for the intended application in this chapter, and so was beyond the scope of the current work. Adapting the phantom to include a

variety of other structures would, however, make it more widely applicable to other minimally invasive neurosurgeries. It is thought that in future, with improvements in 3D printing technology, this will become less challenging, as printers would likely have higher resolution and shorter print times.

Conclusion

This thesis presents novel fabrication methods for creating polyvinyl alcohol cryogel (PVA-c) phantoms for applications in minimally invasive surgery. The aim was to overcome prominent limitations with phantom fabrication techniques, including limited patient-specific geometries, restricted compatibility with imaging modalities, and high cost. The methods described here address these challenges, and culminate in the creation an open source platform (found <u>here</u>) that allows all the files used in this work to be readily shared with the community, enabling others to easily replicate the phantoms presented.

Unfortunately, due to the COVID crisis, access to the laboratory and clinical scanners were abruptly limited during the course of this work, and so had a significant impact on all of the work presented here. Care was taken to mitigate the effects of COVID on this thesis as much as possible, but as with any lab-based project, some limitations were inevitable.

In **Chapter 2**, a detailed discussion of phantoms for applications in minimally invasive surgery was provided. Here, the current challenges applicable to the overall themes of the thesis were presented, and context was given for the work that follows.

Chapter 3 described the development of a novel fabrication method for the creation of wall-less, vascular, ultrasound phantoms is developed, using PVA. The technique used PVA in two different forms - both as a solid, 3D printing material and as an aqueous solution for forming the tissue mimicking material (TMM). The results showed that the phantoms were highly ultrasound compatible, and could be extended to also include computed tomography (CT) and MRI contrast. With this method, it was possible to overcome some of the challenges previously experi-

enced with phantom fabrication techniques, such as difficulty in creating complex or patient-specific structures.

In **Chapter 4**, the methods developed in the previous chapter were expanded, and a novel, self-healing ultrasound nerve phantom was described. The phantom was shown to be highly useful for simulating procedures used in minimally invasive surgery, such as needle insertions and hydrodissection. As well as using the prior methods developed to overcome challenges with anatomical complexity and patient-specificity, the nerve phantoms presented also addressed challenges associated with cost-effectiveness and longevity. The majority of alternative methods do not show self-healing properties, so cannot be used repeatedly over long periods of time, and commercial phantoms that do have some level of self-healing are prohibitively expensive. The work in this chapter showed that the phantoms could be used repeatedly, without causing any visible damage to the phantom, even when viewed with ultrasound imaging, and they were relatively low cost, so the production of multiple models for different clinical training scenarios is feasible.

At the beginning of **Chapter 5**, literature was presented on the use of LED-based PAI for guiding minimally invasive procedures. The role of phantoms in the development of such systems, and their transfer into clinical use was also described. This was followed by an investigation into the use of PVA-c phantoms, which were developed earlier in this thesis, for PAI. The phantoms were found to be suitable for combined ultrasound and PAI, and with India ink used as a contrast agent, PA signal could be acquired from vessels up to depths of around 20 mm. The phantoms could also be used to simulate PA guided needle insertions and the work in this chapter provided a promising foundation for future work.

Finally, in **Chapter 6**, a novel multi-modality, patient-specific brain phantom, including a vestibular schwannoma tumour was presented. An ultrasound and CT compatible brain phantom was successfully created, and work on expanding this to also include MRI compatibility was described. The novel brain phantom had

the required level of anatomical detail for applications in minimally invasive neuro-surgery, and was shown to be useful in the development of a novel neuronavigational system. The use of 3D printing techniques enabled anatomically realistic details to be achieved, and the phantom proved to be mechanically stable enough to be manipulated in the same was as human tissue, and allow minimally invasive surgery to be simulated.

PVA-c was used as the tissue mimicking material, across all chapters, due to its beneficial properties. It is a water-based material, so naturally has a speed of sound similar to that of human tissue, and its acoustic and mechanical properties could be tuned by varying the freeze-thaw cycles or adding contrast agents into the aqueous solution. Preservatives were added to the material so that it could be stored for extended periods of time. 3D printing was used in conjunction with the TMM to enable rapid fabrication, and the realisation of patient-specific details.

The phantoms presented are all relatively cost-effective, although the definition of this of course depends on geography, and the amount of times a phantom will be used. It is also not particularly cost-effective or efficient to buy all the equipment required to fabricate a single phantom. However, for labs that already have the basic equipment required, or for settings where multiple phantoms will be fabricated and used, the methods presented provide a novel framework for rapidly fabricating phantoms that are more cost-effective that the commercially available alternatives. This framework also enables the fabrication of phantoms that are significantly more flexible than commercial options and other fabrication techniques, and the method can be adapted to different applications, patient-specific geometries, and imaging environments. The one-time costs associated with obtaining the equipment used in the novel fabrication techniques described in this thesis are estimated to be around £8000, as explained in **Chapter 4** and the cost per phantom, after this intial cost, is estimated to be approximately £30, depending on the size and geometry of the phantom.

Although there were many successful results presented here, the work is also subject to a range of limitations; the limitations pertaining to each individual chapter were discussed in the relevant sections. Despite this, the methods developed provide a good basis for further work to build on. An appropriate level of anatomical detail was achieved, through the use of patient-specific data to create the phantoms. However, in future, they could be improved by including more layers of complexity, such as adding tendons into the nerve phantoms, or other internal brain structures into the brain phantoms.

One key direction of future work is to improve the MRI compatibility of the brain phantoms presented in Chapter 6. This will be done by confirming the appropriate level of contrast agents required to adequately simulate T1 contrast in all the tissues. Further work on the effect of the other contrast agents - including ultrasound and CT - on the T1 contrast would also be beneficial.

The work in Chapter 5 described a promising direction for PVA-c phantoms, and it would be interesting to further investigate what is feasible with PAI, and extend the work presented to include interventional PAI, based on the success of the self-healing work in Chapter 4. Finally, as the nerve phantoms in Chapter 4 were shown to be relevant for applications in minimally invasive surgery, such as needle-based interventions, it would be interesting to perform a study to assess their clinical use as training phantoms.

All the work presented as part of this thesis has contributed to the development of an open source platform ((found here)), which enables the methods, materials, 3D printing files, and patient-data required to recreate the phantoms described to be collated and shared with the wider community. It is hoped that this will enable others to easily access everything necessary to replicate any of the work from this thesis, and encourage transparency in the field.

MRI Protocol for Siemens Magnetom

Included below is the protocol used to acquire MRI images in **Chapter 3** and to acquire MRI images of the whole phantom in **Chapter 6 (Section 6.3.3)**.

SIEMENS MAGNETOM Prisma_fit

\\RESEARCH\Cranial_Nerves\Cranial_Nerves\SBN\t1_mpr_stealth_ns_tra_DIS3D
TA: 5:19 PM: ISO Voxel size: 0.5×0.5×1.5 mmPAT: 2 Rel. SNR: 1.00 : tfl

Properties

Prio recon	Off
Load images to viewer	On
Inline movie	Off
Auto store images	On
Load images to stamp segments	On
Load images to graphic segments	Off
Auto open inline display	Off
Auto close inline display	Off
Start measurement without further preparation	Off
Wait for user to start	Off
Start measurements	Single measurement

Routine

Slab group	1
Slabs	1
Dist. factor	50 %
Position	L5.8 A22.0 H0.9 mm
Orientation	Transversal
Phase enc. dir.	R >> L
AutoAlign	---
Phase oversampling	13 %
Slice oversampling	77.8 %
Slices per slab	144
FoV read	250 mm
FoV phase	100.0 %
Slice thickness	1.50 mm
TR	2020.0 ms
TE	1.65 ms
Averages	1
Concatenations	1
Filter	Distortion Corr.(3D), Prescan Normalize, Elliptical filter
Coil elements	HC1-7;NC1

Contrast - Common

TR	2020.0 ms
TE	1.65 ms
Magn. preparation	Non-sel. IR
TI	1100 ms
Flip angle	15 deg
Fat suppr.	None
Water suppr.	None

Contrast - Dynamic

Averages	1
Averaging mode	Long term
Reconstruction	Magnitude
Measurements	1
Multiple series	Each measurement

Resolution - Common

FoV read	250 mm
FoV phase	100.0 %
Slice thickness	1.50 mm
Base resolution	256
Phase resolution	100 %
Slice resolution	100 %
Phase partial Fourier	Off
Slice partial Fourier	Off

Resolution - Common

Interpolation	On

Resolution - iPAT

PAT mode	GRAPPA
Accel. factor PE	2
Ref. lines PE	24
Accel. factor 3D	1
Reference scan mode	Integrated

Resolution - Filter Image

Image Filter	Off
Distortion Corr.	On
Mode	3D
Unfiltered images	Off
Prescan Normalize	On
Unfiltered images	Off
Normalize	Off
B1 filter	Off

Resolution - Filter Rawdata

Raw filter	Off
Elliptical filter	On

Geometry - Common

Slab group	1
Slabs	1
Dist. factor	50 %
Position	L5.8 A22.0 H0.9 mm
Orientation	Transversal
Phase enc. dir.	R >> L
Slice oversampling	77.8 %
Slices per slab	144
FoV read	250 mm
FoV phase	100.0 %
Slice thickness	1.50 mm
TR	2020.0 ms
Multi-slice mode	Single shot
Series	Ascending
Concatenations	1

Geometry - AutoAlign

Slab group	1
Position	L5.8 A22.0 H0.9 mm
Orientation	Transversal
Phase enc. dir.	R >> L
AutoAlign	---
Initial Position	L5.8 A22.0 H0.9
L	5.8 mm
A	22.0 mm
H	0.9 mm
Initial Rotation	90.00 deg
Initial Orientation	Transversal

Geometry - Navigator

Geometry - Tim Planning Suite

Set-n-Go Protocol	Off
Table position	H
Table position	1 mm
Inline Composing	Off

SIEMENS MAGNETOM Prisma_fit

System - Miscellaneous

Positioning mode	ISO
Table position	H
Table position	1 mm
MSMA	S - C - T
Sagittal	R >> L
Coronal	P >> A
Transversal	F >> H
Coil Combine Mode	Adaptive Combine
Save uncombined	Off
Matrix Optimization	Off
AutoAlign	---
Coil Select Mode	On - AutoCoilSelect

System - Adjustments

B0 Shim mode	Tune up
B1 Shim mode	TrueForm
Adjust with body coil	Off
Confirm freq. adjustment	Off
Assume Dominant Fat	Off
Assume Silicone	Off
Adjustment Tolerance	Auto

System - Adjust Volume

Position	Isocenter
Orientation	Transversal
Rotation	0.00 deg
A >> P	263 mm
R >> L	350 mm
F >> H	350 mm
Reset	Off

System - pTx Volumes

B1 Shim mode	TrueForm
Excitation	Non-sel.

System - Tx/Rx

Frequency 1H	123.252616 MHz
Correction factor	1
Gain	Low
Img. Scale Cor.	1.000
Reset	Off
? Ref. amplitude 1H	0.000 V

Physio - Signal1

1st Signal/Mode	None
TR	2020.0 ms
Concatenations	1

Physio - Cardiac

Magn. preparation	Non-sel. IR
TI	1100 ms
Fat suppr.	None
Dark blood	Off
FoV read	250 mm
FoV phase	100.0 %
Phase resolution	100 %

Physio - PACE

Resp. control	Off
Concatenations	1

Inline - Common

Subtract	Off

Inline - Common

Measurements	1
StdDev	Off
Save original images	On

Inline - MIP

MIP-Sag	Off
MIP-Cor	Off
MIP-Tra	Off
MIP-Time	Off
Save original images	On

Inline - Composing

Inline Composing	Off
Distortion Corr.	On
Mode	3D
Unfiltered images	Off

Sequence - Part 1

Introduction	On
Dimension	3D
Elliptical scanning	Off
Reordering	Linear
Asymmetric echo	Allowed
Flow comp.	No
Multi-slice mode	Single shot
Echo spacing	5.1 ms
Bandwidth	350 Hz/Px

Sequence - Part 2

RF pulse type	Fast
Gradient mode	Normal
Excitation	Non-sel.
RF spoiling	On
Incr. Gradient spoiling	Off
Turbo factor	256

Sequence - Assistant

Mode	Off

JoVE Protocol

Included below is the protocol used in the JoVE publication, which details how to create a patient-specific brain tumour phantom. The text is taken from Mackle *et al.* 2020 [140] and the video etailing these steps can be found **here**.

jove

Brain phantoms in particular have been fabricated using different methods, depending on the level of complexity required and the tissues that need to be replicated[20, 21, 22, 23]. Usually, a mold is used, and liquid tissue-mimicking material poured into it. Some studies have used commercial molds[24] whilst others use 3D-printed custom molds of a healthy brain, and simulate brain lesions by implanting marker spheres and inflatable catheters[19, 25]. To the best of the author's knowledge, this is the first report of a 3D-printed patient-specific brain tumor phantom model created with tissue-mimicking ultrasound and X-ray properties. The total fabrication is visualized by the flowchart in **Figure 1**; the whole process takes around a week to complete.

Protocol

This study was conducted according to the principles expressed in the Declaration of Helsinki and was approved by the NHS Health Research Authority and Research Ethics Committee (18/LO/0266). Informed consent was obtained, and all imaging data were completely anonymized before analysis.

1. Data

1. Obtain pre-operative contrast-enhanced T1-weighted Magnetic Resonance Imaging (MRI) and volumetric computed tomography (CT) data.

    1. If acquired in Digital Imaging and Communications in Medicine (DICOM) format, convert to Neuroimaging Informatics Technology Initiative[26] (NiFTI) format for processing and analysis.

2. Obtain intraoperative ultrasound data.

2. Segmentation

1. Install software to segment the patient data with.

2. Skull segmentation
   NOTE: The steps involved in segmenting the skull broadly follow those outlined by Cramer and Quigley[27] on https://radmodules.com/, but are adapted to create an appropriately-sized craniotomy.

    1. Load the patient's volumetric CT scan in segmentation software, open the **Segment Editor** module and create new segmentation named 'Skull'.

    2. Use the '**Threshold**' function to highlight the skull.

    3. Remove any unwanted segmentations (e.g., skin calcifications, mandible, C1/2, styloid process, the CT patient frame, and any annotations embedded within the image). Use the '**Scissors**' function to remove parts when viewing the model in 3D and make use of the '**Islands**' function after manually disconnecting any unwanted structures using the '**Erase**' function.

    4. Manually correct any gaps in the segmentation that were missed during thresholding using the '**Paint**' and '**Draw**' functions (e.g., lamina papyracea, cortical edge of the mastoid bone and ethmoid bone).

    5. Use the '**Paint**' and '**Draw**' functions to fill in the foramen magnum and create a 5 mm protruding spike upon which the lower part of phantom model can be secured.
       NOTE: The location of the spike is best determined on the coronal and sagittal image planes.

    6. Apply the '**Smoothing**' function. Use a median smoothing setting of 1.0 mm (3 × 3 × 1 pixels) to minimize the amount of detail lost.

jove

NOTE: If the phantom model must include a complete intact skull (e.g., to facilitate surgical simulation of creating an appropriately located craniotomy), move to step 2.2.15; however, if a craniotomy is required in the model, complete steps 2.2.7 to 2.2.14.

7. Click 'Add' to add a new segmentation and name it 'Skull Craniotomy'.

8. In the **'Segmentations'** module, copy the 'Skull' segmentation across to 'Skull Craniotomy' using the **'Copy/Move Segments'** tab.
   NOTE: Both the 'Skull' and 'Skull Craniotomy' segmentations are needed in order to be able to perform the functions described in steps 2.2.9 to 2.2.13

9. Use the '**Scissors**' function to remove an appropriately-sized craniotomy in 'Skull Craniotomy'.
   NOTE: Creating the craniotomy this way will, also, remove an addition portion of skull on the opposite side hence the need for steps 2.2.11 to 2.2.14.

10. Click **'Add'** and add a new segmentation; name it 'Craniotomy Only'.

11. In 'Craniotomy Only' select the segmentation 'Skull Craniotomy' and use the '**Logical Operator**' function to subtract 'Skull Craniotomy' from 'Skull'.

12. Use the '**Scissors**' function to erase everything except the desired craniotomy on the correct side of the tumor, saving 'Craniotomy Only'.

13. In 'Skull Craniotomy' use the '**Logical Operator**' function to subtract 'Craniotomy only' from 'Skull' and save.

14. Open **'Segmentations'** module and export the 'Skull Craniotomy' as a stereolithography (STL) file.

15. Open 3D modeling software and import the STL file 'Skull Craniotomy'.
    NOTE: If the model appears in striped pink complete the '**Flip Normals**' function by selecting the complete model (**Select | Double click**) and then '**Edit | Flip Normals**'. The model will now turn grey and can be edited. Ensure '**View Objects Browser**' is turned on.

16. Reduce the number of triangles to improve the computational time.

17. Select the complete model (**Select | Double click** turns the model orange) then '**Edit | Reduce**'. The default '**Reduce**' function is set at 50% so repeat until the desired reduction is achieved. Aim for a total number of triangles < 500,000.

18. Apply '**Smoothing**' function ensuring the '**Shape Preserving**' box remains ticked. Select the complete model then '**Deform | Smooth**'.

19. Click '**Analysis'** then **'Inspector'** and use this function to detect any small defects in the model and click auto-repair (suggest '**Flat-fill**' selection).

20. Cut 'Skull' to create a top and bottom using the '**Edit/ Plane**' cut function. Select '**Keep Both Slices**' and '**Remeshed**' fill type. Change skull to transparent with '**Shaders**' function to provide a better internal view of the skull and adjust the plane so that it is parallel to the skull base.

21. Separate shells by selecting '**Edit | Separate shells**' and rename 'Skull_Top' and 'Skull_Bottom' within the objects browser.
    NOTE: Do not move their positions. Click the eye icon to remove one or the other from view.

jⱺve

22. Click '**Meshmix'** then select **'Cylinder'** to create a dowel and edit size to 4 mm × 10 mm × 4 mm ('**Edit | Transform'**). Hide 'Skull_Bottom' by clicking the eye icon to remove from view.

23. Select '**Edit | Align'** planes. An additional transparent cylinder will appear. In the '**Align'** window, choose 'Surface point' (left click end transparent cylinder) for the **'Source'** and 'Surface point' (**Shift** + **left click** undersurface of 'Skull_Top') for the **'Destination.'**

24. Using the '**Edit | Transform'** function move dowel into skull using the green arrow and adjust position with blue and red arrows. Rename 'Dowel_Anterior'.

25. In the object browser make 3 copies and rename 'Dowel_Posterior', 'Dowel_Left' and 'Dowel_Right'.

26. Move each dowel to the desired location using the '**Edit | Transform'** function.
    NOTE: Do not move or change the position of the dowel in the green plane.

27. Create copies of each but keep all copies in the same location and create an additional dowel and resize to 3 mm × 10 mm × 3 mm. Rename 'Dowel'.

28. Create holes for Dowels in the skull using the '**Boolean Difference'** function. Select 'Skull_Top' first and then select a dowel in the object browser. In the '**Boolean Difference**' tab ensure '**Auto-reduce**' is switch off. Repeat for each dowel in turn.

29. Hide 'Skull_Top' and view 'Skull_Bottom' repeating the above '**Boolean Difference'** function for each dowel in turn.

30. Export 'Skull_Top', 'Skull_Bottom' and 'Dowel' as separate binary STL files.

3. Brain tissue segmentation

1. Upload the contrast enhanced T1 MRI of the brain to http://niftyweb.cs.ucl.ac.uk/program.php?p=GIF and download its output. This is an open-source parcellation tool for T1-weighted images that utilizes a Geodesic Information Flow (GIF) algorithm[28] to perform brain extraction and tissue segmentation.

2. Open segmentation software and load the contrast enhanced T1 MRI and GIF parcellation output file.

3. Open the '**Segment Editor'** module and create a new segmentation.

4. Select the appropriate labels and combine them to form a single segmentation. For example, cerebral and diencephalon label maps can be combined to create one model, referred to as 'Brain' and midbrain, brainstem, cerebellum and vermian structures can be combined to create a second model referred to as 'Cerebellum'.

5. Use the '**Smoothing'** function (suggested median 2.00 mm, 5 × 5 × 3 pixels).

6. Use the '**Scissors'** function to remove any unwanted or erroneous segmentations.

7. Save 'Brain' and 'Cerebellum' segmentations.

8. Open '**Segmentations'** module and export 'Brain' and 'Cerebellum' as STL files.

4. Tumor segmentation

1. Open segmentation software and load the contrast enhanced T1 MRI.

2. Open the '**Segment Editor'** module and create new segmentation named 'Tumor'.

3. Use the '**Threshold'** function to highlight the tumor.

jove

4. Correct the segmentation using the '**Paint**', '**Draw**' and '**Erase**' functions.

5. Apply the '**Smoothing**' function (suggested median 2.00 mm 5 x 5 x 3 pixels).

6. Create a new segmentation named 'Cerebellum_Tumor'.

7. Combine the 'Cerebellum' model and 'Tumor' using the '**Logical Operators | Add**' function.

8. Save 'Tumor' and 'Cerebellum_Tumor' segmentations.

9. Open '**Segmentations**' module and export 'Tumor' and 'Cerebellum_Tumor' as STL files.
   NOTE: At the end of the segmentation process, the following files are available: 'Skull_Top', 'Skull_Bottom', 'Dowel', 'Brain', 'Cerebellum', 'Tumor', 'Cerebellum_Tumor'.

3. 3D Printing of Brain/Tumor Molds and Skull

1. Create the brain and tumor molds

   1. Split the 'Brain' segmentation into two hemispheres, using the '**Plane cut**' tool in 3D modeling software.

   2. Save each hemisphere as a separate STL file 'Brain right' and 'Brain left'.

   3. Import the STL file 'Tumor' into computer-aided design (CAD) software.

   4. Click the '**mesh**' tab and then use the '**Reduce**' function to reduce the size of the model so that it can be handled by the program – the aim is to reduce the size as much as possible, whilst still retaining all the detail necessary.

   5. Click the '**solid**' tab and use the '**Mesh to BRep**' tool to convert the imported mesh to a body that can be

manipulated. If this action cannot be completed, the mesh was not reduced enough in step 3.1.3.

6. Click '**Create**' then '**Box**' and draw a box around the tumor. Select to create this as a '**New Body**' and rotate the view to ensure the box completely encloses the tumor on all sides.

7. In the modify tab, use the '**Combine**' tool to cut the tumor (the '**Tool Body**') from the box (the '**Target Body**'). This will then leave a box with a hollow shape of the tumor inside it.

8. Check that the hollowed-out box is present. Cut this box into an appropriate number of pieces so that once the mold is filled, it can be prized apart without damaging the phantom inside. For the tumor here, it is enough to split the box in two, but for the other parts of the phantom, more pieces are needed.

9. Create planes through the box in the places that the mold needs to be cut. Click '**Construct**' then '**Midplane**' to create a plane through the center of the box. Right click on the created plane and choose '**Offset Plane**' to position the plane more precisely.

10. Use the '**Split Body**' function in the '**Modify**' tab to split the mold along the planes created.

11. Move the individual pieces of the mold, by right clicking and selecting '**Move/Copy**', so that all the pieces are facing outwards.

12. Add rivets to the faces of each piece of the mold (so it can fit together securely), by clicking '**Create sketch**' then '**Centre diameter circle**' and on each face, drawing small circles. Right click then '**Extrude**' these circles outwards a few millimeters on one face and extrude them inwards on the corresponding face.

jɔve

NOTE: The circles that are extruded inwards need to be slightly bigger - approximately 1.5 mm - than those that are extruded outwards, so that they will fit together snugly.

13. Save each piece of the mold as a separate STL file.

14. Repeat steps 3.1.4 – 3.1.14 for 'Brain left', 'Brain right' and 'Cerebellum tumor'.

NOTE: Using the file 'Cerebellum tumor' rather than just 'Cerebellum' to create the mold means that the mold will have a space in it for the tumor to be inserted during construction.

2. Print the 3D molds

1. Install or open 3D printing software.

2. Open the STL file for each piece of the mold in the printing software and rotate it so that it lies flat against the build plate. It is possible to add multiple mold pieces to the build plate and to print these simultaneously.

3. Choose a large layer height (around 0.2 mm) and low infill value (around 20%) for faster printing. Print the molds using a rigid material such as Polylactic acid (PLA). If the molds are positioned appropriately, support material is not necessary.

3. Print the Skull

1. Open the 'Skull Top' file in the printing software and choose a large layer height (around 0.2 mm) and low infill value (around 20%).

2. Print the skull model in PLA but in contrast to step 3.2.3, support material will be required, so select to '**Add support**' in the software. PVA is used as the support material as it can later be dissolved away with water.

3. Repeat steps 3.3.1 and 3.3.2 for 'Skull Bottom'.

4. Once the top and bottom of the skull have been printed, submerge them in water overnight to dissolve away the PVA support material.

NOTE: The support material will dissolve away much faster if warm water is used, but if the water is too warm, it will deform the printed PLA. Therefore, it is preferable to use cool water and leave the print submerged overnight.

4. Preparation of PVA-c

1. Measure 200 g of PVA powder and set to the side.

2. Heat 1800 g of deionized water to 90 °C and add to a 2L conical flask.

NOTE: The water needs to be almost boiling so the PVA powder will dissolve readily, but if the water reaches 100 °C, some will be lost to evaporation, which is to be avoided.

3. Suspend the conical flask in a temperature-controlled water bath set at 90 °C.

4. Position an electronic stirrer in the flask, ensuring it does not touch the bottom or sides, and set the speed to 1500 rpm.

NOTE: Check that the water is stirring evenly and there are not stagnant points at the sides or bottom.

5. Gradually add the PVA powder to the conical flask, over around 30 min, then leave it to stir for around another 90 min. The resulting gel is the tissue-mimicking material PVA-c.

6. Remove conical flask from the water bath and pour the contents into a beaker. Cover the top with cling film to prevent the formation of a skin on top of the PVA-c. Leave the PVA-c to cool to room temperature (around

jove

20 °C). Once cooled, the PVA-c will be transparent. Tiny white crystals may be seen in the PVA-c, but any bubbles appearing on the surface must be gently scraped off.

7. Add 0.5 w/w% potassium sorbate to the PVA-c as a preservative, and manually stir well.

8. The PVA-c can be left at room temperature if covered in cling film for a few days before it is poured into molds.

5. Phantom Assembly

1. Measure out enough PVA-c to fill the tumor mold into a beaker.

2. To the PVA-c for the tumor, add 1 w/w% glass microspheres for ultrasound contrast and 5 w/w% Barium Sulfate for X-ray contrast, and stir by hand.
   NOTE: It may be necessary to measure out excess PVA-c for the tumor so that these percentages are a measurable amount.

3. Sonicate the beaker to ensure homogenous mixing of the additives.

4. Leave to cool and allow any bubbles formed to escape, around 10 min, then scrape any bubbles from the surface.
   NOTE: Do not leave for extended period once the glass spheres have been added, no longer than around 10 min, before pouring the PVA-c into a mold, as the glass spheres will settle to the bottom of the beaker. Once the phantom has been frozen, this will no longer be a concern, and the final phantom can be used at room temperature.

5. Secure the tumor mold together (tape can be used to cover the joins in the mold) and pour in the PVA-c through the hole in the top of the mold. Leave for a few minutes to allow any bubbles formed in the pouring process to escape through the hole, then place straight into the freezer.

6. Perform two freeze-thaw cycles on the tumor; each cycle here consists of 6 h of freezing at -20 °C and 6 h of thawing at room temperature. Then, carefully remove from mold.

7. Place the tumor into the corresponding space for it in the cerebellum mold, then construct the rest of the cerebellum mold and secure it together.

8. To the remaining PVA-c add 0.05 w/w% glass microspheres, then repeat steps 5.1.3 and 5.1.4.

9. Pour the PVA-c into the cerebellum mold, allowing it to surround the tumor that has been placed inside. Additionally, pour the mixture into the molds for each brain hemisphere.

10. Perform two freeze-thaw cycles on each brain hemisphere and the cerebellum; each cycle here consists of 24 h of freezing at -20 °C and 24 h of thawing at room temperature.
    NOTE: Cycles with 12 h freezing followed by 12 h thawing also effective, to allow the phantom to be created in less time. 24 h was chosen for ease of application, to avoid returning to the lab every 12 h.

11. Once the phantoms have thawed for the second time, carefully remove them from the molds and place into the printed skull.
    NOTE: When not in use, the completed PVA-c phantoms should be stored in an airtight container in the fridge, and can be kept for a few weeks in this way

12. For completion, place the 'Cerebellum tumor' phantom on the spike at the base of the 'Skull Bottom' model. The models of two brain hemispheres ('Brain left' and 'Brain right') are placed on top and slot into the uppermost part of the 'Cerebellum tumor'.

jove

13. Place the four dowels in each space on the 'Skull Bottom' model and place 'Skull Top' model on top. If required, the model may then be maneuvered into the desired position to simulate intraoperative use in surgery.

6. Phantom Imaging

1. Ultrasound Imaging

    1. Apply ultrasound gel to the imaging probe.

       NOTE: Gel is not used intraoperatively but may be used in simulation and does not significantly change the clinical workflow or the quality of the acquired images.

    2. Image the brain and tumor through the craniotomy, with a clinical scanner and burr hole probe.

2. CT Imaging

    1. Image the whole phantom in a CT scanner.

Representative Results

Following the described protocol, an anatomically realistic phantom was fabricated, which consists of a patient-specific skull, brain and tumor. The relevant anatomical structures for the phantom (skull, brain, tumor) are segmented using patient MRI and CT data (**Figure 2a,b**). The patient intra-operative ultrasound data (**Figure 2c**; **Figure 2d** shows the same image as **Figure 2c**, but with the tumor outlined) was used to compare the phantom images to the real patient images.

Meshes were created for each piece of the model (**Figure 3**), and these were then used to manufacture the 3D molds. The molds were easily printed on a commercial printer and assembled by slotting the pieces together. The cerebellum mold was the most complex to design and assemble (**Figure 4**). The skull (**Figure 5a**) was the most difficult part to print as it required support material, so was a slow process; the whole print took a total of three days to complete, which is a limiting factor in the protocol.

The completed phantom (**Figure 5**) was a realistic model of a patient skull, brain and tumor. The two brain hemispheres (**Figure 5b**) were produced separately, and have a realistic appearance, featuring the gyri and sulci of the brain. The whole phantom is white in color, as this is the natural color of PVA-c; this can easily be changed by adding dye but was not necessary for the application. The cerebellum (**Figure 5c**) fits comfortably into the base of the printed skull and the brain hemispheres sit on top of this. The tumor is easily visible in the cerebellum, as the extra contrast added to the tumor results in it being an off-white color that separates it from the surrounding material, which is it securely attached to.

The phantom was imaged with both CT and ultrasound (**Figure 6a,b**). Barium sulfate was used to give the tumor appropriate CT contrast, and the phantom image (**Figure 6a**) shows that this was achieved, as the tumor is clearly visualized. The skull was not printed with 100% infill, in order to reduce the time taken for printing. Therefore, the skull does not look entirely realistic in the CT images, because the lattice structure of the print can be seen. This is not a problem for the application, as only the outline of the skull is needed for the neuronavigation system. The skull could be printed with 100% infill to avoid this reduced accuracy of the CT image, but would add time onto the printing process. Glass microspheres were added to the cerebellum, brain hemispheres and tumor for ultrasound contrast. The results show that the tumor is also visible with ultrasound imaging (**Figure 6b**) and can be distinguished from the surrounding tissue. On visual inspection, the ultrasound images obtained

MRI Protocol for Phillips Ingenia

Included below is the protocol used to acquire MRI images of the samples in **Chapter 6**.

Nucleus =	"H1";		Refocusing control =	"constant";
SmartSelect =	"yes";		angle (deg) =	180;
Coil 1 (exclude) =	"None";		bright fat reduction =	"no";
Uniformity =	"CLEAR";		TR =	"user
FOV FH (mm) =	120;		defined";	
RL (mm) =	200;		(ms) =	15000;
ACQ voxel size FH (mm) =	1;		Halfscan =	"no";
RL (mm) =	1;		Water-fat shift =	"user
Slice thickness (mm) =	5;		defined";	
Recon voxel size FH (mm) =	0.833333313;		(pixels) =	1;
RL (mm) =	0.833333313;		IR delay (ms) = 100;	
Fold-over suppression =	"no";		dual =	"no";
Reconstruction matrix =	240;		power =	"1";
SENSE =	"no";		RF Shims =	"adaptive";
k-t BLAST =	"no";		Shim =	"default";
Slice orientation =	"coronal";		mDIXON =	"no";
Fold-over direction =	"RL";		Fat suppression =	"no";
Fat shift direction =	"F";		Grad Rev Fat suppr =	"no";
Slice Offc. AP (P=+mm) =	-54.3621635;		Water suppression =	"no";
RL (L=+mm) = -1.54418683;			MTC =	"no";
FH (H=+mm) = 4.90181875;			Research prepulse =	"no";
Ang. AP (deg) =			Zoom imaging =	"no";
0.00489285914;			Diffusion mode =	"no";
RL (deg) =	4.47798395;		T1 mapping =	"no";
FH (deg) =	0.125276864;		Transmit channels =	"both";
Free rotatable =	"no";		SAR mode =	"high";
Large table movement =	"no";		B1 mode =	"default";
PlanAlign =	"no";		SAR allow first level =	"yes";
REST slabs =	0;		PNS mode =	"high";
Interactive positioning =	"no";		Gradient mode =	
Patient position =	"head first";		"default";	
Patient body position =	"head first";		SofTone mode =	"no";
Patient orientation =	"supine";		Cardiac synchronization =	"no";
Patient body orientation =	"supine";		Heart rate > 250 bpm =	"no";
Scan type =	"Imaging";		Respiratory compensation =	"no";
Scan mode =	"2D";		Navigator respiratory comp =	"no";
technique =	"IR";		Flow compensation =	"no";
Acquisition mode =	"cartesian";		Motion smoothing =	"no";
Fast Imaging mode =	"TSE";		NSA =	1;
shot mode =	"multishot";		Manual start =	"no";
TSE factor =	26;		Dynamic study =	"no";
startup echoes =	0;		Arterial Spin labeling = "no";	
profile order =	"low_high";		Preparation phases =	"auto";
DRIVE =	"no";		Interactive F0 = "no";	
ultrashort = "no";			B0 field map =	"no";
fid reduction =	"default";		B1 field map =	"no";
Echoes =	1;		MIP/MPR =	"no";
partial echo = "no";			Images =	"M", "R", (2)
TE =	"user		"no";	
defined";			Autoview image =	"R";
(ms) =	5.9000001;			

Reference tissue =   "Grey matter";
Recon compression =   "No";
Preset window contrast =   "soft";
Reconstruction mode =   "real time";
Save raw data =   "no";
Hardcopy protocol =   "no";
Image filter =   "system default";
Uniformity correction =   "no";
Geometry correction =   "default";
IF_info_seperator =   1634755923;
Total scan duration =   "02:15.0";
Rel. SNR =   0.803947985;
Act. TR/TI (ms) =   "15000 / 100";
Act. TE (ms) =   "5.9";
ACQ matrix M x P =   "120 x 182";
ACQ voxel MPS (mm) =   "1.00 / 1.10 / 5.00";
REC voxel MPS (mm) =   "0.83 / 0.83 / 5.00";
Scan percentage (%) =   91;
WFS (pix) / BW (Hz) =   "0.996 / 435.8";
TSE es / shot (ms) =   "5.9 / 153";
TEeff / TEequiv (ms) =   "6 / 6 ";
Min. TR/TI (ms) =   "626 / 50";
Head SAR =   "< 4 %";
Whole body SAR / level =   "0.0 W/kg / normal";
SED =   " 0.0 kJ/kg";
Coil Power =   "4 %";
Max B1+rms =   "0.56 uT";
PNS / level =   "41 % / normal";
dB/dt =   "38.6 T/s";
Sound Pressure Level (dB) = 17.6766739;

List of Abbreviations

ABS: acrylonitrile butadeine styrene

BMI: body mass index

$BaSO_4$: barium sulphate

CAD: computer aided design

$CaSO_4$: copper sulphate

CT: computed tomography

FDM: fused deposition modelling

GPU: graphics processing unit

HIPS: high impact polystyrene

ICG: indocyanine green

IVUS: intravascular ultrasound imaging

LED: light emitting diode

MRI: magnetic resonsance imaging

NIR: near-infrared

PAI: photoacoustic imaging

PET: positron emission tomography

PLA: polylactic acid

PVA: polyvinyl alcohol

PVA-c: poly-vinyl alcohol cryogel

PVCP: polyvinyl chloride

OPOs: optical parametric oscillators

ROI: region of interest

RF: radiofrequency

SLA: stereolithography

SNR: signal-to-noise ratio

TMM: tissue mimicking material

TPU: thermoplasctic polyurethane

w/w: weight-by-weight

List of Components

List of components and equipment used in this thesis to fabrication PVA-c phantoms

3D printer: Ultimaker 3 and Ultimaker 5S; see Ultimaker website for information on where to purchase

Barium sulphate: powder, from Amazon

Copper sulphate: powdered, Amazon

Electronic stirrer: Eurostar Digital 20, IKA from IKA.com

Glass microspheres: 53 - 106 um, from Amazon

PLA for 3D printing: various colours, bought from RS Components, but available from many sources

Potassium sorbate: powder, from from Amazon

PVA-c powder: >90 % hydrolysed, bought from Sigma Aldrich but available from various sources

PVA for 3D printing: bought from RS Components, but available from many sources. Care must be taken to store this material in a airtight container or bag, to prevent absorption of humidity from the air

Water bath: HBR4 control from IKA

Other general equipment required: beakers, blu-tac, conical flasks, tape, weighing scale,

Bibliography

[1] D. I. Nikitichev, A. Barburas, K. McPherson, J. M. Mari, S. J. West, and A. E. Desjardins. Construction of 3-dimensional printed ultrasound phantoms with wall-less vessels. *J Ultrasound Med*, 35(6):1333–9, 2016. 16, 32, 47, 48

[2] J.R. Cook, R. R. Bouchard, and S. Y. Emelianov. Tissue-mimicking phantoms for photoacoustic and ultrasonic imaging. *Biomedical Optics Express*, 2(11):3193–3206, 2011. 21, 30, 32, 38, 95

[3] S. Wang, Y. Noh, J. Brown, S. Roujol, Y. Li, S. Wang, R. Housden, M. C. Ester, M. Al-Hamadani, R. Rajani, and K. Rhode. Development and testing of an ultrasound-compatible cardiac phantom for interventional procedure simulation using direct three-dimensional printing. *3D Print Addit Manuf*, 7(6):269–278, 2020. 21

[4] S. Mirza and S. Athreya. Review of simulation training in interventional radiology. *Acad Radiol*, 25(4):529–539, 2018. 21

[5] A. Tejo-Otero, I. Buj-Corral, and F. Fenollosa-Artes. 3d printing in medicine for preoperative surgical planning: A review. *Ann Biomed Eng*, 48(2):536–555, 2020. 21

[6] S. Shen, H. Wang, Y. Xue, L. Yuan, X. Zhou, Z. Zhao, E. Dong, B. Liu, W. Liu, B. Cromeens, B. Adler, G. Besner, and R. X. Xu. Freeform fabrication of tissue-simulating phantom for potential use of surgical planning in conjoined twins separation surgery. *Sci Rep*, 7(1):11048, 2017. 22

[7] A. U. Niazi, N. Haldipur, A. G. Prasad, and V. W. Chan. Ultrasound-guided regional anesthesia performance in the early learning period: effect of simulation training. *Reg Anesth Pain Med*, 37(1):51–4, 2012. 22

[8] T.M.H. Naur, P.M. Nilsson, P.I. Pietersen, P.F. Clementsen, and L. Konge. Simulation-based training in flexible bronchoscopy and endobronchial ultrasound-guided transbronchial needle aspiration (ebus-tbna): A systematic review. *Respiration*, 93:355–362, 2017. 22

[9] K. S. Akhtar, A. Chen, N. J. Standfield, and C. M. Gupte. The role of simulation in developing surgical skills. *Curr Rev Musculoskelet Med*, 7(2):155–60, 2014. 22

[10] V. Vitiello, S. L. Lee, T. P. Cundy, and G. Z. Yang. Emerging robotic platforms for minimally invasive surgery. *IEEE Rev Biomed Eng*, 6:111–26, 2013. 30

[11] K. H. Fuchs. Minimally invasive surgery. *Endoscopy*, 34(2):154–159, 2002. 30

[12] https://www.adam-rouilly.co.uk/products/clinical-skills-simulators/blue-phantom-ultrasound-training models. Accessed on: 13/10/2021, 2021. 30

[13] C. K. McGarry, L. J. Grattan, A. M. Ivory, F. Leek, G. P. Liney, Y. Liu, P. Miloro, R. Rai, A. Robinson, A. J. Shih, B. Zeqiri, and C. H. Clark. Tissue mimicking materials for imaging and therapy phantoms: a review. *Phys Med Biol*, 2020. 32

[14] P. Li, Z. Yang, and S. Jiang. Tissue mimicking materials in image-guided needle-based interventions: A review. *Mater Sci Eng C Mater Biol Appl*, 93:1116–1131, 2018. 32

[15] M. O. Culjat, D. Goldenberg, P. Tewari, and R. S. Singh. A review of tissue substitutes for ultrasound imaging. *Ultrasound Med Biol*, 36(6):861–73, 2010. 32, 33, 39

[16] G. McIlvain, E. Ganji, C. Cooper, M. L. Killian, B. A. Ogunnaike, and C. L. Johnson. Reliable preparation of agarose phantoms for use in quantitative magnetic resonance elastography. *J Mech Behav Biomed Mater*, 97:65–73, 2019. 32

[17] L. C. Cabrelli, P. I. Pelissari, A. M. Deana, A. A. Carneiro, and T. Z. Pavan. Stable phantom materials for ultrasound and optical imaging. *Phys Med Biol*, 62(2):432–447, 2017. 32, 33

[18] E. Maneas, W. Xia, O. Ogunlade, M. Fonseca, D. I. Nikitichev, A. L. David, S. J. West, S. Ourselin, J. C. Hebden, T. Vercauteren, and A. E. Desjardins. Gel wax-based tissue-mimicking phantoms for multispectral photoacoustic imaging. *Biomed Opt Express*, 9(3):1151–1163, 2018. 32, 40

[19] A. Pacioni, M. Carbone, C. Freschi, R. Viglialoro, V. Ferrari, and M. Ferrari. Patient-specific ultrasound liver phantom: materials and fabrication method. *Int J Comput Assist Radiol Surg*, 10(7):1065–75, 2015. 33, 37

[20] C. Hazelaar, M. van Eijnatten, M. Dahele, J. Wolff, T. Forouzanfar, B. Slotman, and Wfar Verbakel. Using 3d printing techniques to create an anthropomorphic thorax phantom for medical imaging purposes. *Med Phys*, 45(1):92–100, 2018. 33, 37

[21] I. M. de Carvalho, L. L. De Matheo, J. F. Costa Junior, M. Borba Cde, M. A. von Kruger, A. F. Infantosi, and W. C. Pereira. Polyvinyl chloride plastisol breast phantoms for ultrasound imaging. *Ultrasonics*, 70:98–106, 2016. 33

[22] W. Xia, D. Piras, M. Heijblom, W. Steenbergen, T. G. van Leeuwen, and S. Manohar. Poly(vinyl alcohol) gels as photoacoustic breast phantoms revisited. *J Biomed Opt*, 16(7):075002, 2011. 33, 34, 95

[23] K. J. Surry, H. J. Austin, A. Fenster, and T. M. Peters. Poly(vinyl alcohol) cryogel phantoms for use in ultrasound and mr imaging. *Phys Med Biol*, 49(24):5529–46, 2004. 34, 47

[24] S. Jiang, S. Liu, and W. Feng. Pva hydrogel properties for biomedical application. *J Mech Behav Biomed Mater*, 4(7):1228–33, 2011. 34

[25] W. Jamroz, J. Szafraniec, M. Kurek, and R. Jachowicz. 3d printing in pharmaceutical and medical applications - recent achievements and challenges. *Pharm Res*, 35(9):176, 2018. 35, 36

[26] J. Coles-Black, D. Bolton, and J. Chuen. Accessing 3d printed vascular phantoms for procedural simulation. *Front Surg*, 7:626212, 2020. 36, 47

[27] https://www.hubs.com/knowledge-base/how-design-parts-sla-3d printing/. Accessed on: 29/10/21, 2021. 36

[28] I. Hernandez-Giron, J. M. den Harder, G. J. Streekstra, J. Geleijns, and W. J. H. Veldkamp. Development of a 3d printed anthropomorphic lung phantom for image quality assessment in ct. *Phys Med*, 57:47–57, 2019. 37

[29] E. D. Ehler, B. M. Barney, P. D. Higgins, and K. E. Dusenbery. Patient specific 3d printed phantom for imrt quality assurance. *Phys Med Biol*, 59(19):5763–73, 2014. 37

[30] R. L. Scawn, A. Foster, B. W. Lee, D. O. Kikkawa, and B. S. Korn. Customised 3d printing: An innovative training tool for the next generation of orbital surgeons. *Orbit*, 34(4):216–9, 2015. 37

[31] G. Biglino, P. Verschueren, R. Zegels, A.M. Taylor, and S. Schievano. Rapid prototyping compliant arterial phantoms for in-vitro studies and device testing. *Journal of Cardiovascular Magnetic Resonance*, 15(1):1–7, 2013. 37

[32] V. Filippou and C. Tsoumpas. Recent advances on the development of phantoms using 3d printing for imaging with ct, mri, pet, spect, and ultrasound. *Med Phys*, 2018. 37

[33] Y. He, Y. Liu, B. A. Dyer, J. M. Boone, S. Liu, T. Chen, F. Zheng, Y. Zhu, Y. Sun, Y. Rong, and J. Qiu. 3d-printed breast phantom for multi-purpose and multi-modality imaging. *Quant Imaging Med Surg*, 9(1):63–74, 2019. 37

[34] H. Magsood and R. L. Hadimani. Development of anatomically accurate brain phantom for experimental validation of stimulation strengths during tms. *Mater Sci Eng C Mater Biol Appl*, 120:111705, 2021. 37

[35] P. G. M. Knoops, G. Biglino, A. D. Hughes, K. H. Parker, L. Xu, S. Schievano, and R. Torii. A mock circulatory system incorporating a compliant 3d-printed anatomical model to investigate pulmonary hemodynamics. *Artif Organs*, 41(7):637–646, 2017. 37

[36] E. L. Madsen, J. A. Zagsebski, R. A. Banjavie, and R. E. Jutila. Tissue mimicking materials for ultrasound phantoms. *Med Phys*, 5(5):391–394, 1978. 38

[37] F. Z. Lu, J.A. Zagzebski, and Lee F. T. Ultrasound backscatter and attenuation in human liver with diffuse disease. *Ultrasound Med Biol*, 25(7):1047–1054, 1999. 38

[38] D. Nicholas. Evaluation of backscattering coefficients for exicised human tissues: results, interpretation and associated measurements. *Ultrasound Med Biol*, 8(1):17–28, 1982. 38

[39] K. Funamoto, O. Yamashita, and T. Hayase. Poly(vinyl alcohol) gel ultrasound phantom with durability and visibility of internal flow. *J Med Ultrason (2001)*, 42(1):17–23, 2015. 39

[40] Y. Cao, G. Y. Li, X. Zhang, and Y. L. Liu. Tissue-mimicking materials for elastography phantoms: A review. *Extreme Mechanics Letters*, 17:62–70, 2017. 39

[41] S. Cournane, A. J. Fagan, and J. E. Browne. Review of ultrasound elastography quality control and training test phantoms. *Ultrasound*, 20(1):16–23, 2012. 39

[42] S. Cournane, L. Cannon, J. E. Browne, and A. J. Fagan. Assessment of the accuracy of an ultrasound elastography liver scanning system using a pva-cryogel phantom with optimal acoustic and mechanical properties. *Phys Med Biol*, 55(19):5965–83, 2010. 39

[43] P. Beard. Biomedical photoacoustic imaging. *Interface Focus*, 1(4):602–31, 2011. 39, 40

[44] Y. Zhu, G. Xu, J. Yuan, J. Jo, G. Gandikota, H. Demirci, T. Agano, N. Sato, Y. Shigeta, and X. Wang. Light emitting diodes based photoacoustic imaging and potential clinical applications. *Sci Rep*, 8(1):9885, 2018. 40, 91

[45] M. K. Dasa, C. Markos, M. Maria, C. R. Petersen, P. M. Moselund, and O. Bang. High-pulse energy supercontinuum laser for high-resolution spectroscopic photoacoustic imaging of lipids in the 1650-1850 nm region. *Biomed Opt Express*, 9(4):1762–1770, 2018. 40, 89

[46] R. Nachabe, B. H. Hendriks, A. E. Desjardins, M. van der Voort, M. B. van der Mark, and H. J. Sterenborg. Estimation of lipid and water concentrations in scattering media with diffuse optical spectroscopy from 900 to 1,600 nm. *J Biomed Opt*, 15(3):037015, 2010. 40, 89

[47] A. Balthasar, A. E. Desjardins, M. van der Voort, S. Roggeveen, K. Wang, W. Bierhoff, A. G. Kessels, M. Sommer, and M. van Kleef. Optical detection of vascular penetration during nerve blocks: an in vivo human study. *Reg Anesth Pain Med*, 37:3–7, 2012. 40, 91

[48] W. Xia, M. Kuniyil Ajith Singh, E. Maneas, N. Sato, Y. Shigeta, T. Agano, S. Ourselin, J. West S, and E. Desjardins A. Handheld real-time led-based photoacoustic and ultrasound imaging system for accurate visualization of clinical metal needles and superficial vasculature to guide minimally invasive procedures. *Sensors (Basel)*, 18(5), 2018. 40, 90, 93, 97

[49] A. Kharine, S. Manohar, R. Seeton, R. G. Kolkman, R. A. Bolt, W. Steenbergen, and F. F. M. de Mul. Poly(vinyl alcohol) gels for use as tissue phantoms in photoacoustic mammography. *Phys Med Biol*, 48(3), 2003. 40, 54, 95

[50] S. E. Bohndiek, S. Bodapati, D. Van De Sompel, S. R. Kothapalli, and S. S. Gambhir. Development and application of stable phantoms for the evaluation of photoacoustic imaging instruments. *PLoS One*, 8(9):e75533, 2013. 40, 95

[51] A. Valladares, T. Beyer, and I. Rausch. Physical imaging phantoms for simulation of tumor heterogeneity in pet, ct, and mri: An overview of existing designs. *Med Phys*, 47(4):2023–2037, 2020. 40

[52] Karolina Stepniak, Ali Ursani, Narinder Paul, and Hani Naguib. Novel 3d printing technology for ct phantom coronary arteries with high geometrical accuracy for biomedical imaging applications. *Bioprinting*, 18, 2020. 40

[53] J. Solc, T. Vrba, and L. Burianova. Tissue-equivalence of 3d-printed plastics for medical phantoms in radiology. *Journal of Instrumentation*, 13(09):P09018–P09018, 2018. 40

[54] I. Mano, H. Goshima, M. Nambu, and M. Iio. New polyvinyl alcohol gel material for mri phantoms. *Magnetic Resonance in Medicine*, 3:921–926, 1986. 41

[55] I. Reinertsen, M. Descoteaux, K. Siddiqi, and D. L. Collins. Validation of vessel-based registration for correction of brain shift. *Med Image Anal*, 11(4):374–88, 2007. 41

[56] S. J. Chen, P. Hellier, M. Marchal, J. Y. Gauvrit, R. Carpentier, X. Morandi, and D. L. Collins. An anthropomorphic polyvinyl alcohol brain phantom based on colin27 for use in multimodal imaging. *Med Phys*, 39(1):554–61, 2012. 41, 57, 110, 116, 117

[57] 2019. 44, 49

[58] G. A. Roth, G. A. Mensah, C. O. Johnson, G. Addolorato, E. Ammirati, L. M. Baddour, N. C. Barengo, A. Z. Beaton, E. J. Benjamin, C. P. Benziger, A. Bonny, M. Brauer, M. Brodmann, T. J. Cahill, J. Carapetis, A. L. Catapano, S. S. Chugh, L. T. Cooper, J. Coresh, M. Criqui, N. DeCleene, K. A. Eagle, S. Emmons-Bell, V. L. Feigin, J. Fernandez-Sola, G. Fowkes, E. Gakidou, S. M. Grundy, F. J. He, G. Howard, F. Hu, L. Inker, G. Karthikeyan, N. Kassebaum, W. Koroshetz, C. Lavie, D. Lloyd-Jones, H. S. Lu, A. Mirijello,

A. M. Temesgen, A. Mokdad, A. E. Moran, P. Muntner, J. Narula, B. Neal, M. Ntsekhe, G. Moraes de Oliveira, C. Otto, M. Owolabi, M. Pratt, S. Rajagopalan, M. Reitsma, A. L. P. Ribeiro, N. Rigotti, A. Rodgers, C. Sable, S. Shakil, K. Sliwa-Hahnle, B. Stark, J. Sundstrom, P. Timpel, I. M. Tleyjeh, M. Valgimigli, T. Vos, P. K. Whelton, M. Yacoub, L. Zuhlke, C. Murray, V. Fuster, and Gbd-Nhlbi-Jacc Global Burden of Cardiovascular Diseases Writing Group. Global burden of cardiovascular diseases and risk factors, 1990-2019: Update from the gbd 2019 study. *J Am Coll Cardiol*, 76(25):2982–3021, 2020. 44

[59] R. Bauersachs, U. Zeymer, J. B. Briere, C. Marre, K. Bowrin, and M. Huelsebeck. Burden of coronary artery disease and peripheral artery disease: A literature review. *Cardiovasc Ther*, 2019:8295054, 2019. 44, 45

[60] K. G. Smolderen, K. Wang, G. de Pouvourville, B. Bruggenjurgen, J. Rother, U. Zeymer, K. G. Parhofer, P. G. Steg, D. L. Bhatt, E. A. Magnuson, and Reach Registry Investigators. Two-year vascular hospitalisation rates and associated costs in patients at risk of atherothrombosis in france and germany: highest burden for peripheral arterial disease. *Eur J Vasc Endovasc Surg*, 43(2):198–207, 2012. 44

[61] Y.F. Law, K. W. Johnston, H. F. Routh, and R. S. C. Cobbold. On the design and evaluation of a steady flow model for doppler ultrasound studies. *Ultrasound in Med & Biol.*, 15(5):505–516, 1989. 47

[62] M. Russ, R. O'Hara, S. V. Setlur Nagesh, M. Mokin, C. Jimenez, A. Siddiqui, D. Bednarek, S. Rudin, and C. Ionita. Treatment planning for image-guided neuro-vascular interventions using patient-specific 3d printed phantoms. *Proc SPIE Int Soc Opt Eng*, 9417, 2015. 47

[63] D.M. King, C. M. Moran, J. D. McNamara, A. J. Fagan, and J. E. Browne. Development of a vessel mimicking material for use in anatomically realistic doppler flow phantoms. *Ultrasound in Med & Biol.*, 37:813–826, 2011. 47, 48

[64] S. S. Lai, B. Y. Yiu, A. K. Poon, and A. C. Yu. Design of anthropomorphic flow phantoms based on rapid prototyping of compliant vessel geometries. *Ultrasound Med Biol*, 39(9):1654–64, 2013. 47

[65] P. M. O'Flynn, E. T. Roche, and A. S. Pandit. Generating an ex vivo vascular model. *ASAIO J*, 51(4):426–33, 2005. 47

[66] J. Dineley, S. Meagher, T. L. Poepping, W. N. McDicken, and P. R. Hoskins. Design and characterisation of a wall motion phantom. *Ultrasound Med Biol*, 32(9):1349–57, 2006. 47

[67] B. Chayer, M. van den Hoven, M. R. Cardinal, H. Li, A. Swillens, R. Lopata, and G. Cloutier. Atherosclerotic carotid bifurcation phantoms with stenotic soft inclusions for ultrasound flow and vessel wall elastography imaging. *Phys Med Biol*, 64(9):095025, 2019. 47

[68] A. J. Chee, C. K. Ho, B. Y. Yiu, and A. C. Yu. Walled carotid bifurcation phantoms for imaging investigations of vessel wall motion and blood flow dynamics. *IEEE Trans Ultrason Ferroelectr Freq Control*, 63(11):1852–1864, 2016. 47

[69] H. Nisar, J. Moore, R. Piazza, E. Maneas, E. C. S. Chen, and T. M. Peters. A simple, realistic walled phantom for intravascular and intracardiac applications. *Int J Comput Assist Radiol Surg*, 15(9):1513–1523, 2020. 47

[70] K. V. Ramnarine, T. Anderson, and P. R. Hoskins. Construction and geometric stability of physiological flow rate wall-less stenosis phantoms. *Ultrasound in Med & Biol.*, 27(2):245–250, 2001. 47

[71] D. W. Rickey, P. A. Picot, D. A. Christopher, and A. Fenster. A wall-less vessel phantom for doppler ultrasound studies. *Ultrasound in Med & Biol.*, 21(9):1163–1176, 1995. 47

[72] X. Zhou, D. A. Kenwright, S. Wang, J. A. Hossack, and P. R. Hoskins. Fabrication of two flow phantoms for doppler ultrasound imaging. *IEEE Trans Ultrason Ferroelectr Freq Control*, 64(1):53–65, 2017. 47

[73] T. L. Poepping, H. N. Nikolov, T. N. Rankin, M. Lee, and D. W. Holdsworth. An in vitro system for doppler ultrasound flow studies in the stenosed carotid artery bifurcation. *Ultrasound in Med & Biol.*, 28(4):495–506, 2002. 48

[74] J. R. Blake, W. J. Easson, and P. R. Hoskins. A dual-phantom system for validation of velocity measurements in stenosis models under steady flow. *Ultrasound Med Biol*, 35(9):1510–24, 2009. 48

[75] Z. Guo and A. Fenster. Three-dimensional power doppler imaging: A phantom study to quantify vessel stenosis. *Ultrasound in Med & Biol.*, 22(8):1059–1069, 1996. 48

[76] R. F. Smith, B. K. Rutt, and D. W. Holdsworth. Anthropomorphic carotid bifurcation phantom for mri applications. *J Magn Reson Imaging*, 10:533–544, 1999. 48

[77] S. Meagher, T. L. Poepping, K. V. Ramnarine, R. A. Black, and P. R. Hoskins. Anatomical flow phantoms of the nonplanar carotid bifurcation, part ii: experimental validation with doppler ultrasound. *Ultrasound Med Biol*, 33(2):303–10, 2007. 48

[78] D. M. Watts, C. J. Sutcliffe, R. H. Morgan, S. Meagher, J. Wardlaw, M. Connell, M. E. Bastin, I. Marshall, K. V. Ramnarine, P. R. Hoskins, and R. A. Black. Anatomical flow phantoms of the nonplanar carotid bifurcation, part i: computer-aided design and fabrication. *Ultrasound Med Biol*, 33(2):296–302, 2007. 48

[79] C. K. Ho, A. J. Chee, B. Y. Yiu, A. C. Tsang, K. W. Chow, and A. C. Yu. Wall-less flow phantoms with tortuous vascular geometries: Design principles and a patient-specific model fabrication example. *IEEE Trans Ultrason Ferroelectr Freq Control*, 64(1):25–38, 2017. 48

[80] M. Rogosnitzky and S. Branch. Gadolinium-based contrast agent toxicity: a review of known and proposed mechanisms. *Biometals*, 29(3):365–76, 2016. 56

[81] E. Albrecht and K. J. Chin. Advances in regional anaesthesia and acute pain management: a narrative review. *Anaesthesia*, 75 Suppl 1:e101–e110, 2020. 70

[82] P. Warman and B. Nicholls. Ultrasound-guided nerve blocks: efficacy and safety. *Best Pract Res Clin Anaesthesiol*, 23(3):313–26, 2009. 70

[83] J. M. Neal, R. Brull, V. W. Chan, S. A. Grant, J. L. Horn, S. S. Liu, C. J. McCartney, S. N. Narouze, A. Perlas, F. V. Salinas, B. D. Sites, and B. C. Tsui. The asra evidence-based medicine assessment of ultrasound-guided regional anesthesia and pain medicine: Executive summary. *Reg Anesth Pain Med*, 35(2 Suppl):S1–9, 2010. 70

[84] T. E. Kim and B. C. H. Tsui. Simulation-based ultrasound-guided regional anesthesia curriculum for anesthesiology residents. *Korean J Anesthesiol*, 72(1):13–23, 2019. 70, 71

[85] H. M. Smith, S. L. Kopp, A. K. Jacob, L. C. Torsher, and J. R. Hebel. Designing and implementing a comprehensive learner-centered regional anesthesia curriculum. *Reg Anesth Pain Med*, 34:88–94, 2009. 70

[86] G. Hocking, S. Hebard, and C. H. Mitchell. A review of the benefits and pitfalls of phantoms in ultrasound-guided regional anesthesia. *Reg Anesth Pain Med*, 36(2):162–70, 2011. 71, 72

[87] D. Micheller, M. J. Chapman, M. Cover, J. D. Porath, N. Theyyunni, R. Kessler, and R. Huang. A low-fidelity, high-functionality, inexpensive ultrasound-guided nerve block model. *CJEM*, 19(1):58–60, 2017. 72

[88] S. Sparks, D. Evans, and D. Byars. A low cost, high fidelity nerve block model. *Critical Ultrasound Journal*, 6:1–3, 2014. 72

[89] B. A. Pollard. New model for learning ultrasound-guided needle to target localization. *Reg Anesth Pain Med*, 33(4):360–2, 2008. 72

[90] K. M. Rathbun, W. T. Brader, and J. W. Norbury. A simple, realistic, inexpensive nerve phantom. *J Ultrasound Med*, 38(8):2203–2207, 2019. 72

[91] https://simandskills.com/products/regional-anaesthesia-ultrasound-training-block model. Accessed on: 03/01/2022. 84

[92] https://3dgbire.com/pages/ultimaker 3. Accessed on: 03/01/2022. 85

[93] https://www.ika.com/en/Products-Lab-Eq/Heating-Baths-Heated-bath-Oil-bath-csp-206/HBR-4-control-cpdt 20003549/. Accessed on: 03/01/2022. 85

[94] https://www.ika.com/en/Products-Lab-Eq/Overhead-Stirrers-Agitator-Blender-Lab-mixer-csp-187/EUROSTAR-20-digital-cpdt 4442000/. Accessed on: 03/01/2022. 85

[95] https://uk.rs-online.com/web/p/3d-printing materials/8320406. Accessed on: 03/01/2022. 85

[96] https://uk.rs-online.com/web/p/3d-printing materials/8320494. Accessed on: 03/01/2022. 85

[97] https://www.sigmaaldrich.com/GB/en/product/sial/p8136. Accessed on: 03/01/2022. 85

[98] https://www.amazon.co.uk/IVYX Scientific-Digital-Laboratory-RT-100 Accessed on: 03/01/2022. 85

[99] E. C. Mackle, E. Maneas, W. Xia, S. West, and A. E. Desjardins. *LED-based photoacoustic imaging for guiding peripheral minimally invasive procedures*, page 321–334. Springer, 2020. 87

[100] S. Hu and L. V. Wang. Photoacoustic imaging and characterization of the microvasculature. *J Biomed Opt*, 15(1):011101, 2010. 88

[101] H. F. Zhang, K. Maslov, G. Stoica, and L. V. Wang. Functional photoacoustic microscopy for high-resolution and noninvasive in vivo imaging. *Nat Biotechnol*, 24(7):848–51, 2006. 88

[102] E. Z. Zhang, J. G. Laufer, R. B. Pedley, and P. C. Beard. In vivo high-resolution 3d photoacoustic imaging of superficial vascular anatomy. *Phys Med Biol*, 54(4):1035–46, 2009. 88

[103] M. P. Fronheiser, S. A. Ermilov, H. P. Brecht, A. Conjusteau, R. Su, K. Mehta, and A. A. Oraevsky. Real-time optoacoustic monitoring and three-dimensional mapping of a human arm vasculature. *J Biomed Opt*, 15(2):021305, 2010. 88

[104] Qingkai Yao, Yu Ding, Guodong Liu, and Lvming Zeng. Low-cost photoacoustic imaging systems based on laser diode and light-emitting diode excitation. *Journal of Innovative Optical Health Sciences*, 10(04), 2017. 88

[105] H. Zhong, T. Duan, H. Lan, M. Zhou, and F. Gao. Review of low-cost photoacoustic sensing and imaging based on laser diode and light-emitting diode. *Sensors*, 18(7), 2018. 88, 94

[106] R. S. Hansen. Using high-power light emitting diodes for photoacoustic imaging. *Medical Imaging 2011: Ultrasonic Imaging, Tomography, and Therapy*, 7968:79680A, 2011. 88

[107] T. J. Allen and P. C. Beard. Light emitting diodes as an excitation source for biomedical photoacoustics. *Photons Plus Ultrasound: Imaging and Sensing 2013*, 8581:85811F, 2013. 88, 93, 94

[108] A. Hariri, J. Lemaster, J. Wang, A. S. Jeevarathinam, D. L. Chao, and J. V. Jokerst. The characterization of an economic and portable led-based photoacoustic imaging system to facilitate molecular imaging. *Photoacoustics*, 9:10–20, 2018. 88

[109] A. Balthasar, A. E. Desjardins, M. van der Voort, G. W. Lucassen, S. Roggeveen, K. Wang, W. Bierhoff, A. G. Kessels, M. van Kleef, and

M. Sommer. Optical detection of peripheral nerves: an in vivo human study. *Reg Anesth Pain Med*, 37(3):277–82, 2012. 89

[110] Wenfeng Xia, Efthymios Maneas, Nam Trung Huynh, Mithun Kuniyil Ajith Singh, Nina Montaña Brown, Sebastien Ourselin, Edward Gilbert-Kawai, Simeon J. West, Adrien E. Desjardins, Alexander A. Oraevsky, and Lihong V. Wang. Imaging of human peripheral blood vessels during cuff occlusion with a compact led-based photoacoustic and ultrasound system. *Photons Plus Ultrasound: Imaging and Sensing 2019*, 10878:1087804, 2019. 90, 91

[111] E. Maneas, R. Aughwane, N. Huynh, W. Xia, R. Ansari, M. Kuniyil Ajith Singh, J. C. Hutchinson, N. J. Sebire, O. J. Arthurs, J. Deprest, S. Ourselin, P. C. Beard, A. Melbourne, T. Vercauteren, A. L. David, and A. E. Desjardins. Photoacoustic imaging of the human placental vasculature. *J Biophotonics*, 13(4):e201900167, 2020. 90, 95

[112] C. Thompson and T. Barrows. Carotid arterial cannulation: removing the risk with ultrasound? *Can J Anaesth*, 56(6):471–2, 2009. 91

[113] L. Helen, B. D. O'Donnell, and E. Moore. Nerve localization techniques for peripheral nerve block and possible future directions. *Acta Anaesthesiol Scand*, 59(8):962–74, 2015. 92

[114] J. M. Mari, W. Xia, S. J. West, and A. E. Desjardins. Interventional multispectral photoacoustic imaging with a clinical ultrasound probe for discriminating nerves and tendons: an ex vivo pilot study. *J Biomed Opt*, 20(11):110503, 2015. 92

[115] D. Piras, C. Grijsen, P. Schutte, W. Steenbergen, and S. Manohar. Photoacoustic needle: minimally invasive guidance to biopsy. *J Biomed Opt*, 18(7):070502, 2013. 92

[116] W. Xia, D. I. Nikitichev, J. M. Mari, S. J. West, R. Pratt, A. L. David, S. Ourselin, P. C. Beard, and A. E. Desjardins. Performance characteristics of an interventional multispectral photoacoustic imaging system for guiding minimally invasive procedures. *J Biomed Opt*, 20(8):86005, 2015. 92, 96, 105

[117] Wenfeng Xia, Daniil I. Nikitichev, Jean Martial Mari, Simeon J. West, Sebastien Ourselin, Paul C. Beard, and Adrien E. Desjardins. An interventional multispectral photoacoustic imaging platform for the guidance of minimally invasive procedures. *Opto-Acoustic Methods and Applications in Biophotonics II*, page 95390D, 2015. 92

[118] W. Xia, E. Maneas, D. I. Nikitichev, C. A. Mosse, G. Sato Dos Santos, T. Vercauteren, A. L. David, J. Deprest, S. Ourselin, P. C. Beard, and A. E. Desjardins. Interventional photoacoustic imaging of the human placenta with ultrasonic tracking for minimally invasive fetal surgeries. *Med Image Comput Comput Assist Interv*, 9349:371–378, 2015. 92

[119] W. Xia, S. Noimark, E. Maneas, M. K. A. Singh, S. Ourselin, S. J. West, and A. E. Desjardins. Led-based photoacoustic imaging of medical devices with carbon nanotube-polydimethylsiloxane composite coatings. *Microscopy Histopathology and Analytics*, page JW3A–4, 2018. 93

[120] Thomas J. Allen, B. T. Cox, and Paul C. Beard. Generating photoacoustic signals using high-peak power pulsed laser diodes. *Photons Plus Ultrasound: Imaging and Sensing 2005: The Sixth Conference on Biomedical Thermoacoustics, Optoacoustics, and Acousto-optics*, 5697:233–242, 2005. 93

[121] T. J. Allen and P. C. Beard. Pulsed near-infrared laser diode excitation system for biomedical photoacoustic imaging. *Opt Lett*, 31:3462–3464, 2006. 93, 94

[122] R. G. Kolkman, W. Steenbergen, and T. G. van Leeuwen. In vivo photoacoustic imaging of blood vessels with a pulsed laser diode. *Lasers Med Sci*, 21(3):134–9, 2006. 93

[123] T. J. Allen and P. C. Beard. High power visible light emitting diodes as pulsed excitation sources for biomedical photoacoustics. *Biomed Opt Express*, 7(4):1260–70, 2016. 93, 94

[124] X. Dai, H. Yang, and H. Jiang. In vivo photoacoustic imaging of vasculature with a low-cost miniature light emitting diode excitation. *Opt Lett*, 42(7):1456–1459, 2017. 94

[125] C. Willert, B. Stasicki, J. Klinner, and S. Moessner. Pulsed operation of high-power light emitting diodes for imaging flow velocimetry. *Measurement Science and Technology*, 21(7), 2010. 94

[126] M. K. A. Singh, T. Agano, N. Sato, Y. Shigeta, and T. Uemura. Real-time in vivo imaging of human lymphatic system using an led-based photoacoustic/ultrasound imaging system. *Photons Plus Ultrasound: Imaging and Sensing 2018*, 10494:1049404, 2018. 94

[127] L. Leggio, S. Gawali, D. Gallego, S. Rodriguez, M. Sanchez, G. Carpintero, and H. Lamela. Optoacoustic response of gold nanorods in soft phantoms

using high-power diode laser assemblies at 870 and 905 nm. *Biomed Opt Express*, 8(3):1430–1440, 2017. 94

[128] F. Gao, L. Bai, X. Feng, H. P. Tham, R. Zhang, Y. Zhang, S. Liu, L. Zhao, Y. Zheng, and Y. Zhao. Remarkable in vivo nonlinear photoacoustic imaging based on near-infrared organic dyes. *Small*, 12(38):5239–5244, 2016. 94

[129] F. Gao, L. Bai, S. Liu, R. Zhang, J. Zhang, X. Feng, Y. Zheng, and Y. Zhao. Rationally encapsulated gold nanorods improving both linear and nonlinear photoacoustic imaging contrast in vivo. *Nanoscale*, 9(1):79–86, 2017. 94

[130] M. F. Beckmann, B. S. Gutrath, A. Buchkremer, T. Eckert, J. Timper, A. Leifert, W. Richtering, U. Simon, and G. Schmitz. Size dependent photoacoustic signal response of gold nanoparticles using a multispectral laser diode system. *IEEE International Ultrasonics Symposium*, page 2336–2339, 2012. 94

[131] B. S. Gutrath, M. F. Beckmann, A. Buchkremer, T. Eckert, J. Timper, A. Leifert, W. Richtering, G. Schmitz, and U. Simon. Size-dependent multispectral photoacoustic response of solid and hollow gold nanoparticles. *Nanotechnology*, 23(22):225707, 2012. 94

[132] V. Cunningham and H. Lamela. Laser optoacoustic spectroscopy of gold nanorods within a highly scattering medium. *Opt Lett*, 35:3387–3389, 2010. 94

[133] B. W. Pogue and M. S. Patterson. Review of tissue simulating phantoms for optical spectroscopy, imaging and dosimetry. *J Biomed Opt*, 11(4):041102, 2006. 95, 96

[134] G. Lamouche, B.F. Kennedy, K.M. Kennedy, C.E. Bisaillon, A. Curatolo, G. Campbell, V. Pazos, and D.D. Sampson. Review of tissue simulating phantoms with controllable optical, mechanical and structural properties for use in optical coherence tomography. *Biomedical optics express*, 3(6):1381–1398, 2012. 95, 96

[135] W. C. Vogt, C. Jia, K. A. Wear, B. S. Garra, and T. Joshua Pfefer. Biologically relevant photoacoustic imaging phantoms with tunable optical and acoustic properties. *J Biomed Opt*, 21(10):101405, 2016. 95

[136] J. Joseph, M. K. Ajith Singh, N. Sato, and S. E. Bohndiek. Technical validation studies of a dual-wavelength led-based photoacoustic and ultrasound imaging system. *Photoacoustics*, 22:100267, 2021. 95

[137] M. Fonseca, B. Zeqiri, P.C. Beard, and B.T. Cox. Characterisation of a phantom for multiwavelength quantitative photoacoustic imaging. *Phys Med Biol*, 61(13):4950, 2016. 95

[138] S. Manohar, A. Kharine, J. C. van Hespen, W. Steenbergen, and T. G. van Leeuwen. Photoacoustic mammography laboratory prototype: imaging of breast tissue phantoms. *J Biomed Opt*, 9(6):1172–81, 2004. 95

[139] X. Wang, X. Xie, G. Ku, L. V. Wang, and G. Stoica. Noninvasive imaging of hemoglobin concentration and oxygenation in the rat brain using high-resolution photoacoustic tomography. *J Biomed Opt*, 11(2):024015, 2006. 105

[140] Eleanor C. Mackle, Jonathan Shapey, Efthymios Maneas, Shakeel R. Saeed, Robert Bradford, Sebastien Ourselin, Tom Vercauteren, and Adrien E. Desjardins. Patient-specific polyvinyl alcohol phantom fabrication with ultrasound and x-ray contrast for brain tumor surgery planning. *Journal of Visualized Experiments*, (161), 2020. 108, 111, 133, 145

[141] J. Shapey, T. Dowrick, R. Delaunay, E. C. Mackle, S. Thompson, M. Janatka, R. Guichard, A. Georgoulas, D. Perez-Suarez, R. Bradford, S. R. Saeed, S. Ourselin, M. J. Clarkson, and T. Vercauteren. Integrated multi-modality image-guided navigation for neurosurgery: open-source software platform using state-of-the-art clinical hardware. *Int J Comput Assist Radiol Surg*, 16(8):1347–1356, 2021. 108, 133

[142] V. K. Gupta, A. Thakker, and K. K. Gupta. Vestibular schwannoma: What we know and where we are heading. *Head Neck Pathol*, 14(4):1058–1066, 2020. 108

[143] C. C. Ploch, Cssa Mansi, J. Jayamohan, and E. Kuhl. Using 3d printing to create personalized brain models for neurosurgical training and preoperative planning. *World Neurosurg*, 90:668–674, 2016. 109

[144] P. Weinstock, R. Rehder, S. P. Prabhu, P. W. Forbes, C. J. Roussin, and A. R. Cohen. Creation of a novel simulator for minimally invasive neurosurgery: fusion of 3d printing and special effects. *J Neurosurg Pediatr*, 20(1):1–9, 2017. 109

[145] J. P. Wansapura, S. K. Holland, R. S. Dunn, and W. S. Ball Jr. Nrm relaxation times in the human brain at 3.0t. *J Magn Reson Imaging*, 9:531–538, 1999. 120, 125

[146] Y. Lee, M.F. Callaghan, J. Acosta-Cabronero, A. Lutti, and Z Nagy. Normal regional t1 and t2 relaxation times of the brain at 3t. *Magnetic resonance in medicine*, 81(1):454–465, 2019. 121

[147] H. Lu, L. M. Nagae-Poetscher, X. Golay, D. Lin, M. Pomper, and P. C. van Zijl. Routine clinical brain mri sequences for use at 3.0 tesla. *J Magn Reson Imaging*, 22(1):13–22, 2005. 125

[148] C. Lin, M Bernstein, J Huston, and S Fain. Measurements of t1 relaxation times at 3.0t: Implications for clinical mra. *Proceedings of the 9th Annual Meeting of ISMRM*, 2001. 125

[149] P. A. Yushkevich, J. Piven, H. C. Hazlett, R. G. Smith, S. Ho, J. C. Gee, and G Gerig. User-guided 3d active contour segmentation of anatomical structures: significantly improved efficiency and reliability. *Neuroimage*, 31(3):1116–1128, 2006. 131